Technische Universität München
TUM School of Computation, Information and Technology

Single-Shot Quantitative Phase Imaging with Common-Path Interferometric Systems

Jie Dong

Vollständiger Abdruck der von der TUM School of Computation, Information and Technology der Technischen Universität München zur Erlangung des akademischen Grades eines

Doktors der Ingenieurwissenschaften (Dr.-Ing.)

genehmigten Dissertation.

Vorsitz:		Prof. Dr.-Ing. Thomas Eibert
Prüfer*innen der Dissertation:	1.	Prof. Dr.-Ing. habil. Dr. h.c. Alexander W. Koch
	2.	Assoc. Prof. Dr.-Ing. Shengjia Wang

Die Dissertation wurde am 15.09.2022 bei der Technischen Universität München eingereicht und durch die TUM School of Computation, Information and Technology am 08.02.2023 angenommen.

Abstract

The phase of light carries important information about a wavefront and is often used for detecting important physical parameters of objects. This thesis develops novel common-path interferometric methods for single-shot quantitative phase imaging, particularly in the fields of speckle interferometry and digital holographic microscopy.

Firstly, a dual-sensitive image-shearing speckle interferometer is developed, which enables simultaneous measurements of in-plane and out-of-plane strain components in a single shot. This method is achieved by combining off-axis interferometry, common-path image shearing, and symmetric observation. Based on the proposed method, we report measurements of multiple crack-tip strain components in mode-I fracture experiments. Next, the common-path image-shearing speckle interferometer with an unlimited minimal shear amount is developed by placing a Wollaston prism near the Fourier plane of a quasi-4f imaging system. This method requires no tilt among the optical components, allowing stable interferometric measurements and simple optical alignment. For a demonstration, we report single-shot full-field measurements of crack-tip strain components with various shear amounts in mode-I fracture experiments.

To correct wavefront aberrations in common-path digital holographic microscopy, a low-pass filtering compensation (LPFC) method is developed. LPFC estimates the phase aberrations from a single hologram of objects by Fourier transform and low-pass spatial filtering. Phase imaging experiments on a Ronchi grating and a human blood smear demonstrate the accuracy and imaging capability of the proposed method. LPFC requires no numerical fitting, iterative steps, or prior knowledge of the optical system, significantly simplifying the process of phase compensation in digital holographic microscopy. Finally, a new common-path interferometric microscopy method, termed multibeam array interferometric microscopy (MAIM), is developed for single-shot high-throughput quantitative phase imaging. This method is achieved by integrating common-path holographic microscopy, multibeam interference technology, and holographic multiplexing technology. MAIM increases the field of view (FOV) of conventional digital holographic microscopy by a maximum factor of 5, while maintaining the subnanometer optical path length stability.

We analyze the theoretical fundamentals of MAIM, build the MAIM prototypes which increase the FOV by factors of 5, 4, and 3, respectively, demonstrate proof-of-concept imaging experiments, and report biomedical imaging applications. MAIM potentially permits (ultra)fast or long-term (time-lapse) imaging of nanoscale dynamics of unstained live samples *in vitro* with a high throughput.

All of these developed methods are based on the off-axis interferometric configuration of common-path geometry, and therefore they offer both high imaging speeds (temporal resolution) and high temporal phase stability.

Contents

Chapter 1

Introduction

1.1 Phase retrieval

Light is an electromagnetic wave, consisting of synchronized oscillations of electric and magnetic fields. Optical imaging utilizes special light-matter interactions, such as reflection, absorption, dispersion, and second-harmonic generation, to obtain detailed images of certain parameters. Both the amplitude and the phase of light play important roles in light-matter interactions, and the phase offers many unique imaging capabilities compared with the intensity. For example, the phase of X-rays allows high-contrast imaging of low-absorbing objects, as in this region the phase-shift section is much larger than the absorption section [1]. Besides, the phase provides quantitative information on certain physical parameters, since the results represent the optical path length difference at the subwavelength level of illumination [2]. Additionally, in X-ray crystallography, the phase of far-field diffraction fields carries the position information of the atoms constituting a molecule [3], revealing the structure of the molecule.

However, direct phase measurements are very challenging, as the light field oscillates at such a high frequency ($\sim 10^{15}$Hz) that no photoelectric device can follow. The commonly used optical sensors, such as photosensitive films, digital cameras, and human eyes, are sensitive to the intensity only, i.e., the photon flux density, which is proportional to the square of the average amplitude of light, rather than the phase itself. The phase information is therefore generally lost in such a square-law detection process, causing the so-called *phase problem*. Although originating from the field of X-ray crystallography [3], in which a structure can be reconstructed from its diffraction data, the phase problem is now met in various other fields where complex fields are required.

Finding solutions to the phase problem is called *phase retrieval*, which usually involves

adding additional complexity to convert the phase variations into the intensity difference, and then extracting the phase from the modulated intensity images that contain the related information. The phase retrieval has been applied in various fields of science and engineering, including X-ray microscopy [4], electron microscopy [5], light microscopy [6], and industrial evaluations such as non-destructive testing (NDT) [7].

1.1.1 Mechanisms

Interference

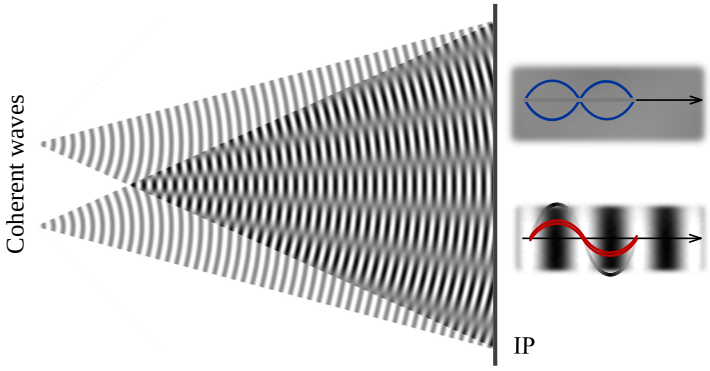

Figure 1.1: Young's double-slit interference. Coherent waves from two slits produce constructive and destructive interference when they are in phase and $n\pi$ out of phase, respectively. IP, imaging plane.

The study of optical interference started at least since the first description of "Newton's rings" in the 17th century [8]. Interference converts relative phase variations to light intensity changes by the superposition principle of waves (Figure 1.1). Bright and dark fringes on the plane IP, which are caused by constructive and destructive interference, represent the relative phase difference of $2n\pi$ and $n\pi$, respectively, where n denotes the natural numbers. Middle level brightness in the fringe pattern represents the transitional phase difference between the interfering waves. Phase-shifting interferometry and digital holography are two modern methods that utilize interference for phase retrieval.

Phase-shifting interferometry. Interferometry involves comparing two or more waves interferometrically, including one known wave that works as a reference wave. The resultant interference pattern is also called an "interferogram", containing both the background intensity and the visible contrast that carries the relative phase information. Locating centers of interference fringes or using fringe-contour-generation techniques allows measurements with errors as large as $\sim \lambda/10$. By adopting a phase-shifting procedure, interferometry can become a *complex-field* technique. Phase-shifting interferometry usually re-

quires multiple recording steps or a spatial carrier frequency in the spatial domain, so that the visible contrast can be separated from the background intensity by using multiple images or by applying frequency analysis methods such as Fourier transform. Phase-shifting interferometry allows extremely sensitive phase measurements (up to $\lambda/100$) [2]. Variable implementations of phase-shifting interferometry have been achieved over the years, such as speckle interferometry [9], imaging-shearing interferometry [10], and interferometers for gravitational wave detection [11].

Digital holography. In the 1940s, holography was invented by Gabor to avoid the spherical aberrations of electron lenses and to improve the resolving power of electron microscopes [5]. Gabor's holography allows a wavefront to be recorded and later reconstructed, which can be described as a two-step process: recording a "hologram" of an object on a photographic film through the interference between illuminating wave and the secondary wave emitted by the object, and reconstructing the object wave through diffraction by illuminating the hologram with the same reference wave. Both step phase-shifting and off-axis techniques can be adopted in holography to ensure the complete recording and reconstruction of amplitudes and phases.

Geometrical optics

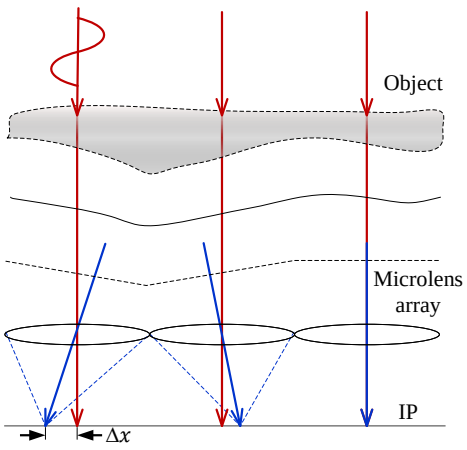

Figure 1.2: Principle of the Shack-Hartmann wavefront sensor. The lateral shifts of the focal spots show the directions (wavefront slope) of the incoming light waves at each microlens, indicating the phase delays of the entire distorted wavefront.

Shack-Hartmann sensors. In the late 1960s, a Shack-Hartmann wavefront sensor was developed based on geometric optics to correct the wavefront distortions introduced by atmospheric turbulence [12]. The Shack-Hartmann wavefront sensor operates by placing a microlens array in front of the plane IP (Figure 1.2). After passing through a phase

object, due to the thickness and refraction index variations, the light gets delayed and bends the ray, causing a distorted wavefront. The distorted wave is split and focused by the microlens array, forming a focal spot array on IP. A local tilt of the wavefront gives rise to the lateral shift of the corresponding focal spot. The wavefront slope can therefore be reconstructed from the lateral shifts by ray tracing, and the phase distribution can be derived from the slope via integration. Characterized at the wavelength of 13.5 nm, it has been demonstrated that the Shack-Hartmann sensor can achieve measurements with an accuracy better than $\lambda/120$ [13]. The spatial resolution of a Shack-Hartmann sensor is mostly limited by the density of its microlens array. However, due to the simplicity and as no coherent light is required, the Shack-Hartmann sensor is particularly popular when the spatial resolution is not critical, such as for correcting atmospheric turbulence.

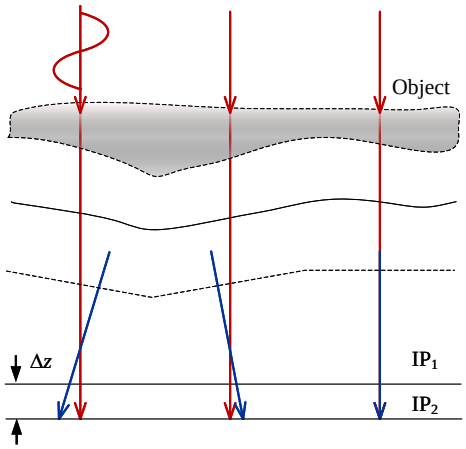

Figure 1.3: Principle of TIE. The slope change of the rays along the propagation direction indicates the associated phase delay.

Transport of intensity. In 1982, a transport-of-intensity equation (TIE) method was developed by Teague to achieve phase retrieval from two-plane irradiance measurements [14]. TIE operates by linking the phase of a wavefront to the partial differential of the intensity along the propagation direction within the framework of the Fresnel diffraction (Figure 1.3). Specifically, a full-field phase distribution can be recovered from two intensity measurements of the tested wavefront, which are taken in two closely spaced planes normal to the propagation direction. The principle can be described by the following second-order differential equation:

$$\frac{2\pi}{\lambda}\frac{\partial I}{\partial z} = -\nabla_\perp \cdot (I\nabla_\perp \varphi), \tag{1.1}$$

where λ represents the wavelength, I represents the infocus image of intensity, z represents the coordinate along the propagation direction, $\nabla_\perp$ stands for the gradient operator in the

lateral dimensions, and φ denotes the phase profile to be recovered. An accuracy better than $\lambda/50$ has been achieved by TIE in the measurement of the strain birefringence in a bent optical fiber [15]. TIE requires no phase unwrapping procedures. Besides, TIE allows non-iterative deterministic phase retrieval with partially coherent light, and therefore it is compatible with all types of brightfield microscopes.

Diffraction

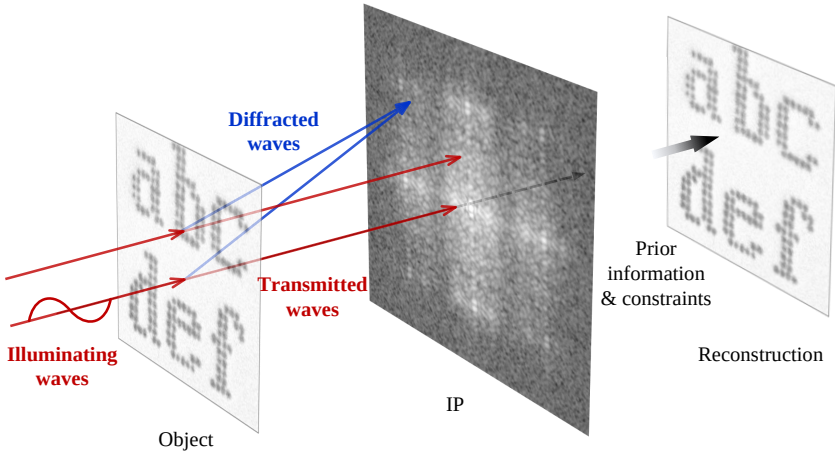

Figure 1.4: Forward-scattering CDI. Coherent waves diffracted from an object produce an image of the far-field (Fraunhofer) diffraction intensity on IP, corresponding to the magnitude of the Fourier transform of the object, and the phase is consequently lost. CDI uses additional reasonable constraints and prior information to ensure the unique image reconstruction.

In crystallography, the phase is essential, as it carries information about the position of atoms and therefore indicates the structure of molecules. In 1952, Sayre suggested that the phase information of a non-crystalline specimen can be reconstructed by oversampling its diffraction pattern at twice the Nyquist frequency [16]. In 1972, Gerchberg and Saxton proposed an iterative algorithm to extract the phase from two intensity images taken at the object plane and the far-field plane, respectively [17]. In 1998, Miao *et al.* successfully recovered the image of a nonperiodic object from its diffraction pattern by combining the oversampling approach and the iterative algorithm, and they termed the method coherent diffraction imaging (CDI) [4]. The far-field diffraction of non-crystalline samples is continuous rather than limited to discrete Bragg peaks, as compared with Bragg's X-ray crystallography [18]. Phase retrieval techniques of non-crystalline specimens allow imaging structures much larger than that attainable with conventional X-ray crystallography, such as small whole cells or large subcellular structures.

CDI utilizes a special property of electromagnetic waves: the far-field diffraction pattern of an object corresponds to its true Fourier transform. Theoretically, the complex field of the object can be totally reconstructed from its far-field magnitude and phase. However, the phase is lost in the square-law detection of the far-field diffraction. CDI achieves the reconstruction by oversampling the far-field magnitude in data collecting and applying iterative algorithms in numerical reconstruction (Figure 1.4). The oversampling procedure overcomes the usually unavoidable limitation of the phase loss. Supported by some prior knowledge and constraints, such as the enclosing boundary of objects, iterative phase retrieval algorithms can recover the object image from the oversampled intensity of the far-field diffraction.

Achieving *lensless imaging* is the motivation of CDI, which is somewhat similar to that of Gabor's holography. Lens-based imaging systems use microscope objective lenses to perform the inverse transform for imaging, and therefore the resolution is fundamentally limited by diffraction. Light sources of a shorter wavelength such as electrons and X-rays are usually required to achieve higher resolution. However, lenses and other "optical" components are very difficult to make in these spectral regions, where refraction almost disappears. For example, creating lenses for hard X-rays requires fabrication techniques with picometer resolution. The existing X-ray lenses suffer from large aberrations and limit the resolution of X-ray microscopy to ∼30-50 nm. To recover the structure of nanometric samples, alternative lensless methods must be established. As an example of lensless imaging, the practical resolution of CDI is limited by the exposure time and the computing power, while the theoretical ultimate resolution is limited only by the wavelength of X-rays.

1.1.2 Established methods

In the visible region, the well-established methods that use phase retrieval for imaging purposes include Zernike phase contrast imaging [19], interferometry [8], holography [20], TIE [21], and Shack-Hartmann wavefront sensing [13] (Figure 1.5). In the region of shorter wavelengths, where high-quality lenses of large numerical apertures are not available, imaging without lenses can avoid aberrations and potentially allows the atomic resolution microscopy of unstained biological molecules. Well-established lensless microscopy methods include X-ray [1] and electron [5] Gabor (in-line) holography, X-ray TIE imaging [22], X-ray [4] and electron [23] CDI, and X-ray [24, 25] and electron [26] ptychography (scanning CDI). Qualitative phase contrast imaging with a shorter wavelength has also been achieved by utilizing special optical devices, such as the X-ray Zernike phase contrast microscopy using Fresnel zone plates [27] and the Nomarski X-ray differential phase contrast microscopy using gratings [28]. In the past decade, the concept of ptychography

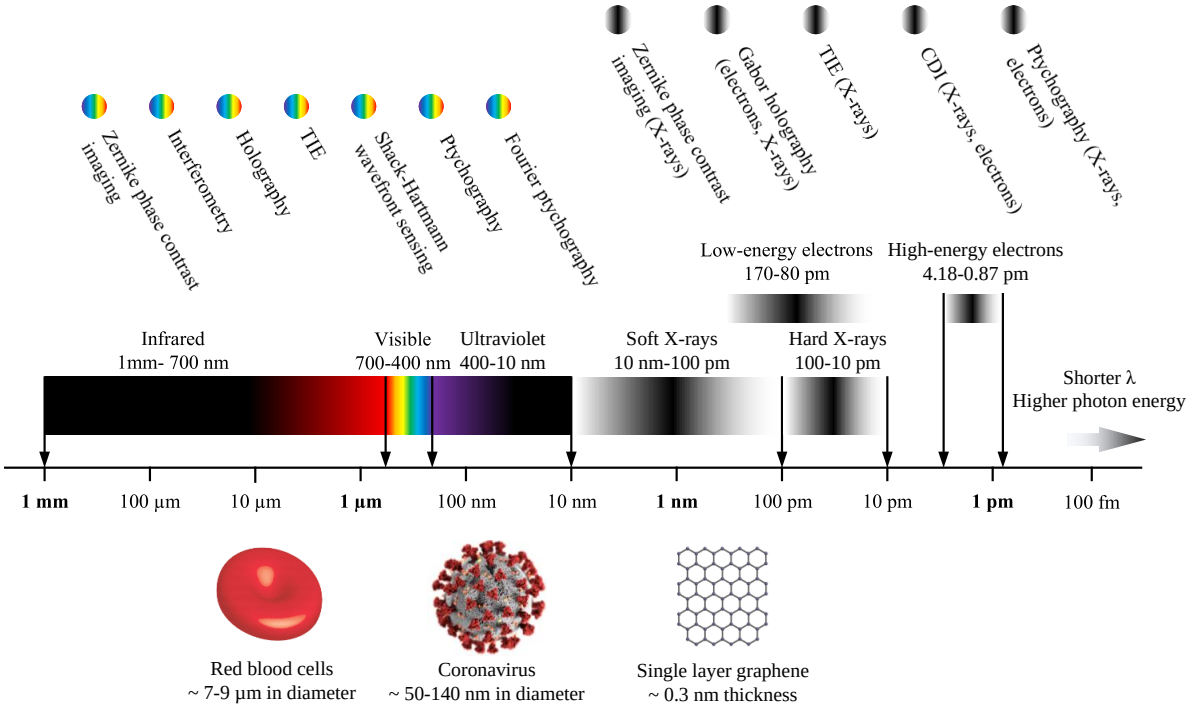

Figure 1.5: Electromagnetic spectrum and established imaging methods of phase retrieval.

has also been applied in the visible region to achieve special imaging capabilities, example of which includes optical laser ptychography [29] and Fourier ptychography [30].

1.2 Interferometric phase imaging

We define *interferometric phase imaging* as any technique that renders phase variations visible through wave interference. Modern interferometric methods permit extremely accurate phase measurements, mostly thanks to the rapid development of laser technology, photoelectric detectors, and computer technology. The aim of this section is to briefly review some of the significant stages in the development of interferometric phase imaging. Theoretical details on the related topics will be discussed in Chapter 2.

1.2.1 History of ideas

Zernike phase contrast microscopy

In the 1930s, phase contrast microscopy (PCM) was invented by Zernike to directly visualize phase objects from a single intensity measurement [19], for which Zernike was awarded the Nobel prize in physics in 1953. PCM converts minute variations in phase to

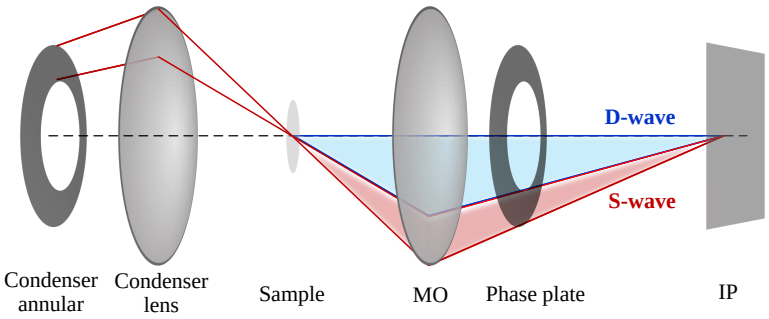

Figure 1.6: Principle of Zernike phase contrast imaging. An illuminating wave directed by a condenser annulus is focused by a condenser lens. After passing through a sample, this wave is divided into two parts: a D-wave (diffracted wave) and a S-wave (surround wave). The two waves are segregated by a phase plate and then recombine in IP, producing high-contrast interference images of transparent objects. MO, microscope objective.

brightness changes by adopting a special interference module (Figure 1.6). PCM provides high-contrast images of transparent specimens, such as living cells, thin tissue slices, and subcellular particles, without labeling. Before Zernike's invention, transparent samples are usually rendered visible by putting the objects out of focus, and then one can see the focal spots and lines, rather than the objects themselves. Zernike's method provides maximum contrast while ensuring that the specimen is accurately in focus. However, the brightness of the PCM amplitude contrast images has a nonlinear relationship with the phase delay, yielding only a qualitative description of objects. Besides, *halo artifacts* caused by the redistribution of light energy also degrade the image quality in PCM.

Gabor in-line holography

In 1948, "a new microscopic principle" was invented by Gabor to solve the spherical aberration problem and to improve the resolving power of electron microscopy [5], for which Gabor was awarded the Nobel prize in physics in 1971. Originating from Bragg's X-ray microscope and Zernike's phase contrast microscopy, Gabor terms his method holography, as a single hologram contains the total information required for reconstructing the object in 3D. Holography involves freezing a light wave in a photographic plate by means of the interference with another (reference) wave and reconstructing it by illuminating the photographic plate with the same reference wave (Figure 1.7). The entire process is therefore a combination of interference and diffraction, which utilizes the wave nature of light. Such a hologram has little resemblance to the object, but contains most of the information to reconstruct the object. Gabor's holography presents several attractive features, including "lens-less imaging", "a complete record of amplitudes and phases", and "total 3D photograph". Besides, the original scene can be reconstructed with only

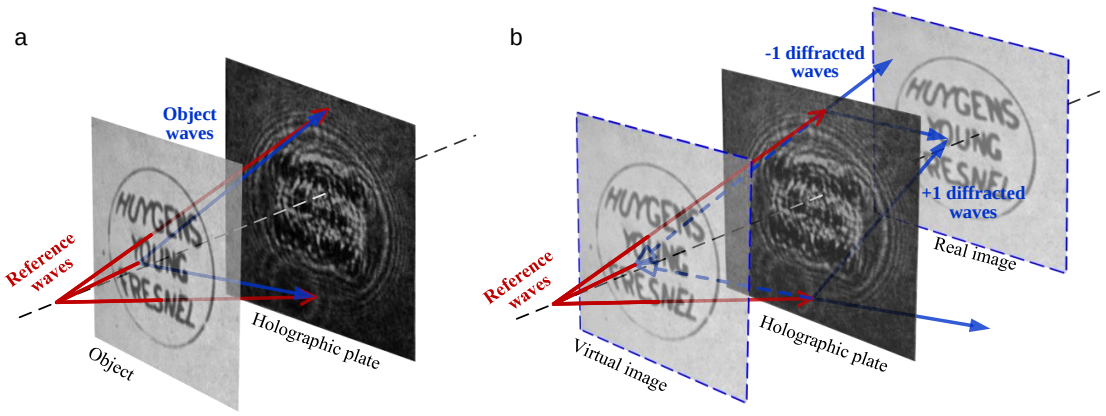

Figure 1.7: Principle of in-line (Gabor) holography. (a) Holographic recording: the interference of a homocentric illuminating (reference) wave and a secondary (object) wave emitted from the object produces a hologram in the holographic plate. (b) Holographic reconstruction: by illuminating the hologram with the same reference wave, diffraction occurs and a real image and a virtual image of the object can be reconstructed simultaneously by the diffracted waves.

a part of the hologram, at the expense of the reduction of resolution and signal-to-noise. However, it has been also troubled by the *twin image* problem caused by the loss of the phase in the holographic recording [31].

Leith-Upatnieks off-axis holography

The twin image problem limits Gabor holography to relatively simple objects that transmit a large proportion of light without scattering, such as transparencies containing dark letters. In 1962, off-axis holography was developed by Leith and Upatnieks to solve this problem [31, 32]. Instead of illuminating the object with only one beam, the Leith-Upatnieks holography eliminates the unwanted terms through two-beam interferometry (Figure 1.8). Leith-Upatnieks holography allows imaging objects that transmit a strong background and objects of continuous tone, which are not possible with Gabor's method. It has also been demonstrated with diffused illumination and irregular 3D objects [32]. The success of holography in the visible region is mostly associated with the invention of off-axis holography, as it permits holographic reconstruction free from flaws and of a quality comparable to the pictures produced by conventional photography with incoherent light. This remarkable feature is achieved by utilizing the fact that a complex signal of bandwidth W can be represented by a real signal of bandwidth $2W$, in which the real signal is derived from the complex one and distributed with a carrier frequency. However, due to the necessity of a carrier frequency, the off-axis recording usually can not make

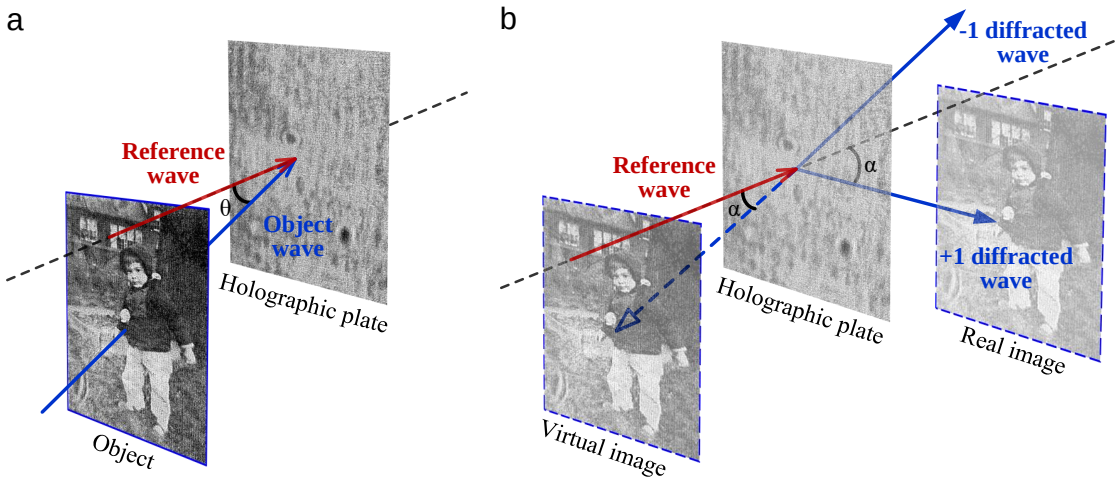

Figure 1.8: Principle of off-axis (Leith-Upatnieks) holography. (a) Holographic recording: a reference wave and an object wave interfere with each other with a small angle, producing fringe patterns superimposed on the Fresnel diffraction pattern of the object. (b) Holographic reconstruction: by illuminating the hologram with the same reference wave, the twin images separated by an angle twice as the introduced one can be reconstructed.

effective use of the bandwidth of detectors, leading to a limited space-bandwidth product (SBP) of Leith-Upatnieks holography. A multibeam array interferometric method is developed to overcome this limitation in phase microscopy in Chapter 6.

Holographic interferometry

Critical requirements of holographic imaging include highly coherent modern lasers, high resolution holographic plates, and highly stable optical elements. Even imperceptible displacements can completely blur out a hologram in the recording process. In 1965, Powell and Stetso invented holographic interferometry for vibration analysis, which utilized the effect that imperceptible displacements could alter a hologram in a manner characterizing the motion itself [33]. The method is basically implemented by recording two exposures containing the wavefronts scattered from a "reference" object and a "live" object, respectively (Figure 1.9). The resultant hologram can be therefore considered as an interferogram of two holograms containing different position information of the object. Any imperceptible surface displacements, e.g., caused by mechanical strains or thermal expansion, can give rise to interference fringes, the centers of which are localized wherever the wavefronts from two exposures are alike, thus mapping contours of constant displacement amplitudes on the object surface between the two exposures. Holographic

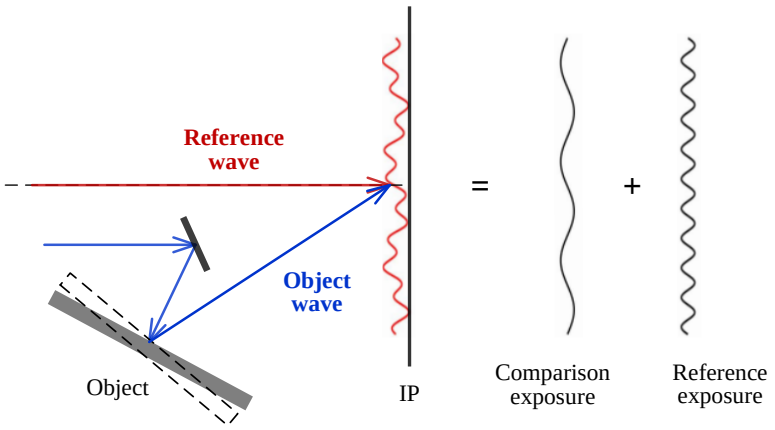

Figure 1.9: Principle of holographic interferometry. The object recorded in the hologram suffers a small surface deformation between exposures. The superposed exposure of the live object and the reference object produces an interferogram that characterizes the deformation itself.

interferometry requires no sample surface modifications, e.g., no fibers need be attached and no special surface preparations such as polishing or coating are required, thus allowing deformation measurements of objects with arbitrary surfaces, which can be either specularly or diffusely reflecting objects of arbitrary shapes. Holographic interferometry is also capable of investigating dynamic phenomena.

Speckle interferometry

Holographic interferometry usually requires holographic plates capable of resolving about 3000 lines/mm to obtain high-quality holograms. However, only the low-frequency phase distribution is essential and significant for metrological purposes. Most of the high-frequency details recorded in a hologram are therefore redundant. The phase carrier of such a high frequency limits holographic interferometry to photographic recording only, rather than using digital detectors. In 1969, Leendertz invented speckle interferometry by utilizing a significant property of laser speckles, namely its ability to carry the phase information of a wavefront [9]. Laser speckle phenomena usually occur when illuminating scattering surfaces with a coherent light source such as a laser. A phase carrier of such a low spatial frequency provides considerably great practical convenience for achieving digital recording. Besides, speckle interferometry also provides flexible sensitivity vectors, allowing measuring physical quantities along various directions. For example, the measurement of pure in-plane surface displacements can be achieved by speckle interferometry, which is not possible via holographic interferometry [10]. By combining a phase-shifting

technique, speckle interferometry overcomes several basic application difficulties of holographic interferometry and has been proved as a high-precision tool with great potential in engineering metrology.

Holographic microscopy

Holographic microscopy originated from both Zernike's phase contrast microscopy and Gabor's holography. The halo artifacts in PCM drive scientists to seek methods that yield quantitative phase images of objects. Attractive features such as "a complete record of amplitudes and phases" and "total 3D photograph" also lead to a massive interest in applying holography in light microscopy.

In 1950, Dyson invented an interferometric microscope to avoid the halo artifacts of PCM [34], which guaranteed maximum visibility of any details in an object and provided quantitative measurements of the optical thickness. In 1965, Leith *et al.* proposed a microscopy method by wavefront reconstruction, in which the two-beam off-axis holography was adopted for holographic imaging [35]. In 1966, Gabor and Goss developed an interference microscopy method capable of recovering the amplitude, phase, and 3D information of an object from two photographs recorded on the same plate [36]. In 1966, Ellis demonstrated "Holomicrography" to simultaneously reconstruct dark-field, phase-contrast, and interference fringe images from a single hologram by modifying the numerical aperture [37]. In 1966, Vanligten and Osterberg reported a holographic microscopy method, which achieved the optimum resolution of l2 µm in a lensless manner, 5 µm when using a microscope objective [38], and a single-hologram depth of view (DOV) of 40 µm. In the 1970s and 1980s, most of the research work on holographic microscopy focused on the applications in the region of X-rays and electrons, as high-NA objective lenses were available in the visible range and therefore the "lens-less imaging" imagery was not demanded urgently in light microscopy. Besides, the reconstruction quality of holography was also limited by the insufficient performance of computers and digital detectors. In 1999, Cuche *et al.* developed a digital holographic microscopy (DHM) [39] method by combining off-axis holography and numerical holographic reconstruction. The axial path-length resolution approaching 10 nm was demonstrated in surface profilometry. This method allows high-precision complex-field imaging at video frequency rates. As it uses objective lenses for microscopic imaging, the transverse spatial resolution up to the coherent resolution limit is also permitted.

1.2.2 High precision phase measurements

High precision interferometric measurements involve recording interferograms with a highly stable system and recovering the phase from interferograms without losing the inherent accuracy. Accurate phase reconstruction can be guaranteed by phase shifting, while common-path configurations ensure a stable interferometric system with high temporal phase stability.

Step phase shifting

In 1966, Gabor and Goss noticed that a single hologram contained only half the information of the object, and "by means of two holograms it must be possible to reconstruct the original wave diffracted by the object totally, in amplitude and in phase, and to obtain a complete optical record of the object" [36]. Due to the attractive features including direct true complex-field reconstruction and high phase accuracy, the step phase-shifting technique was soon adopted in almost all types of interferometric systems. In 1974, Bruning *et al.* applied the phase-shifting method for testing optical surfaces and lenses [40]. In 1982, Hariharan *et al.* developed phase-shifting holographic interferometry to quantify surface deformations [41]. In 1985, Creath proposed phase-shifting speckle interferometry [42]. In 1997, Yamaguchi and Zhang developed digital phase-shifting in-line holography for 3D imaging [43].

Step phase shifting usually involves imposing known phase changes to the reference wave, sequentially capturing interference images during the recording interval, and then reconstructing the phase from the multiple images. Conventional phase shifting usually requires 3, 4, or more shifting steps, but 2-step methods can be also achieved by applying additional numerical algorithms [44, 45]. Step phase shifting can improve the accuracy of phase measurements in interferometry by a factor of 10-100 [2]. However, step phase shifting requires multiple recording steps, which may take a few seconds and consequently reduce the temporary resolution of interferometric systems.

Carrier phase shifting

Spatial carrier phase shifting overcomes the limitation of multiple recordings and achieves single-shot complex-field imaging by combining Leith-Upatnieks off-axis holography and frequency analysis. It has become of practical use since the 1980s, due to the major development of computing power. In 1982, Takeda *et al.* introduced the concept of spatial carrier phase shifting in fringe-pattern analysis by using the fast Fourier transform (FFT) and demonstrated applications of computer-based topography and interferometry [46].

Afterwards, it has been widely adopted in various interferometric systems and other imaging systems using fringe analysis, such as digital speckle interferometry [42], fringe profilometry [47], digital holography [43], and digital holographic microscopy [39].

Spatial carrier phase shifting is normally conducted by modulating the phase information contained in an interferogram through off-axis interferometric recording, which introduces a carrier frequency and separates the multiple components in the spatial domain. Therefore, it can be considered as implementing the phase-shifting steps in the spatial domain, rather than in the temporal domain as compared with the step phase shifting. No moving components are required to achieve such a phase shift, thus ensuring both high acquisition rates and high phase accuracy.

Common-path interferometry

Temporal phase stability is another key parameter to evaluate the performance of an interferometry system. Unlike other techniques, interferometric methods are characterized by a high sensitivity given by the wavelength of illumination. Challenges for applying such methods therefore mostly lie in experimentally improving the stability of the interferometric system. This is mainly due to the fact that most of the interferometric systems require an extra reference beam. Any imperceptible changes in the system, such as mechanical vibrations, thermal deformations, and air fluctuations, may affect the two beams in different ways, leading to unrelated fluctuations in the fringe pattern and low phase stability.

Methods for improving the phase stability in interferometric systems include passive stabilization, active stabilization, and common-path approaches. The passive stabilization is usually implemented by adding additional mechanical oscillations to float the system, e.g., by adopting optical tables. In the famous Michelson-Morley experiment in 1887 [48], the optical system was floated in a bath of mercury to achieve enough accuracy (about $\lambda/50$) for detecting the *aether*. The active stabilization involves continuously monitoring the system noise and introducing a feedback loop, which cancels the detected noise with additional active elements that generate negative signals. The common-path method utilizes the fact that when the reference beam and the object beam travel along the same optical path, or paths that are physically very close to each other, the phase noise in these waves can be very similar, and thus it can be canceled automatically through interference. The common-path method has been successfully applied in various types of geometry in the past. A good illustration is the Zernike PCM [19]. Compared with two-beam interferometers such as a Michelson interferometer or a Mach-Zehnder interferometer, the phase-contrast images obtained with PCM are extremely stable, as the interfering beams

travel along almost the same optical path and pass through the same optical components. Examples of the common-path method also include Gabor in-line holography [5] and Nomarski differential interference contrast microscopy invented in 1955 [49, 50].

The common-path geometry has been adopted in various systems of quantitative phase imaging (QPI). In 1957, Dyson developed two types of common-path interferometers for the interferometric testing of an astronomical reflector [51]. In 1974, Hung and Taylor invented a speckle-shearing interferometric camera for in-plane strain measurements and vibration analyses, which employed a lens and two apertures to achieve quasi common-path interferometry [52] and therefore allowed interferometric measurements in practical fields or factory environments. In 2004, Popescu *et al.* developed a Fourier phase microscopy method by combining the common-path geometry with a programmable phase modulator [53]. This method achieves the phase stability of $\lambda/5500$, allowing imaging nanoscale dynamics in live cells.

1.3 Goal of thesis

By combining the off-axis configuration and the common-path geometry, interferometric methods permit single-shot QPI with high temporal phase stability. However, this approach also presents certain limitations.

Speckle interferometry allows direct measurements of surface displacements or displacement gradients and provides a flexible sensitivity vector. As deformations in nature and engineering are usually in 3D, simultaneous measurements of multiple deformation components have always been in demand. Measuring multiple components by simply integrating interferometers is straightforward, however, difficult to achieve with a common-path and off-axis speckle interferometer which requires a special interferometric configuration, especially the image-shearing type, in which images-shearing devices are required. The single sensitivity limits the applications to 2D measurements. Another drawback of the conventional common-path and off-axis interferometric configuration lies in a limited minimal shear amount. The shear amount is an important parameter in image-shearing interferometry, which significantly affects the measurement results and is usually required to be small enough to obtain certain displacement gradient information. For example, in NDT measurements, a small shear amount ensures that internal defects are visible in the form of singularity areas in phase gradient images, especially in cases where the physical size of defects is relatively small and the entire FOV is large. An excess shear amount can degrade the spatial resolution and deteriorate the shearography approximation, giving rise to immeasurable zones in the target with geometrical discontinuity.

Common-path and off-axis holographic microscopy enables true complex-field reconstruction with high phase (optical path length) stability from a single hologram. In this system, objective lenses, complex spatial filters, and other non-optimal optical components usually distort laser beams containing the object image and lead phase aberrations in the final reconstruction. The phase aberrations can be compensated using a double-exposure approach, which operates by recording a secondary sample-free hologram to estimate the phase aberrations. Single-frame compensation has been in demand, but normally they require numerical fitting, iterative steps, or prior knowledge of the optical parameters of the system. Besides, off-axis digital holographic microscopy achieves high acquisition rates at the expense of insufficient use of the camera bandwidth. The SBP, an important parameter to evaluate the imaging performance of a microscope, is fundamentally limited by the interferometric configuration in off-axis digital holographic microscopy. A low SBP can degrade either the resolution or the FOV, making high-throughput microscopic phase imaging impossible. Single-shot high-throughput quantitative phase imaging is highly desirable, as it is essential for dynamically visualizing and quantifying morphological or biochemical nanoscale phenomena in unstained live samples *in vitro*.

The goal of the work in this dissertation is to develop new interferometric methods to solve the above problems in quantitative phase imaging, particularly in the fields of speckle interferometry and digital holographic microscopy.

1.4 Outline of thesis

Chapter 2 introduces the fundamentals of interferometric phase imaging from the perspectives of both physics and numerical processing. The related knowledge of interference and diffraction, interferometry, Fourier method, and light microscopy is included.

Chapters 3-6 present our own-developed methods that provide phase imaging capabilities/performance previously unachievable.

Chapter 3 presents a dual-sensitive image-shearing speckle interferometer. This system is achieved by integrating off-axis interferometry, common-path image shearing, and symmetric observation. It is capable of simultaneously measuring the distributions of in-plane and out-of-plane strain components in a single shot. For a demonstration, full-field distributions of multiple crack-tip strain components are obtained with the proposed method in mode-I fracture experiments.

Chapter 4 presents a common-path image-shearing speckle interferometer with an unlimited minimal shearing amount. This system is achieved by placing a Wollaston prism near the Fourier plane of a common-path interferometer built by using a quasi-4f imaging

system. It operates without the need to tilt any optical components, which allows a highly stable interferometric configuration and simple optical alignment operations. Using the proposed method, full-field measurements of crack-tip strain components are conducted with various shear amounts in mode-I fracture experiments.

Chapter 5 demonstrates a low-pass filtering compensation (LPFC) method to compensate for wavefront aberrations in common-path digital holographic microscopy. LPFC estimates phase aberrations from a single hologram of objects by Fourier transform and low-pass spatial filtering. LPFC imaging experiments on a Ronchi grating and a human blood smear are carried out to validate the accuracy and capability. LPFC provides phase compensation for both smooth objects and objects containing abrupt edges in a digital holographic system with relatively high-frequency objects and low-frequency slight phase aberrations. It significantly simplifies the process of phase compensation in digital holographic microscopy as compared with conventional methods.

Chapter 6 presents a common-path interferometric microscopy method termed multibeam array interferometric microscopy (MAIM) for single-shot high-throughput quantitative phase imaging. This method is achieved by integrating common-path holographic microscopy, multibeam interference technology, and holographic multiplexing technology. Compared with conventional off-axis digital holographic microscopy, MAIM allows single-shot complex-field imaging with a maximum 5-fold field of view (FOV) increase, while maintaining the subnanometer optical path length stability. We analyze the fundamentals of MAIM and build the prototypes to increase the FOV by factors of 5, 4, and 3, respectively. Proof-of-concept imaging experiments on both natural and artificial samples are conducted to validate the feasibility and the accuracy of our method. We also present biomedical imaging applications, including monitoring subcellular dynamical phenomena in flowing live erythrocytes *in vitro* and label-free micro-refractometry imaging of unstained cancer tissue slices. MAIM potentially enables the (ultra)fast or long-term (time-lapse) imaging of nanoscale dynamics of unstained live samples *in vitro* with a high throughput.

Finally, Chapter 7 summarizes the contribution of this thesis.

Chapter 2

Fundamentals of interferometric phase imaging

Much of the work in this thesis develops new interferometric methods in the fields of speckle interferometry and digital holographic microscopy. In this chapter, we present some theoretical fundamentals essential for our own methods presented in the next chapters. Firstly, the principles of interference and diffraction are introduced, followed by some particular knowledge of interferometry. Then, the basics of the Fourier method and light microscopy are presented.

2.1 Interference and diffraction

The physical understanding of the nature of light involved simple scientific ideas: waves and particles [54, 55]. In 1665, Newton's rings, a phenomenon of interference, was firstly described by Hooke. In 1665, Grimaldi published the first accurate report of diffraction. In 1678, Huygens theorized a model known as Huygens construction to explain the phenomenon of diffraction. In 1803, Young conducted the double-slit interference experiment, which experimentally confirmed the wave theory of light. In 1818, Fresnel calculated light distributions in diffraction with excellent accuracy by expressing Huygens construction and Young's interference principle in quantitative terms. In 1882, Kirchhoff published his diffraction formula, putting the Huygens-Fresnel principle on a sounder mathematical basis. In 1845, Faraday discovered the effect of Faraday rotation, which firstly proved that light was related to electromagnetism. In 1860, Maxwell identified light as an electromagnetic wave. In 1900, Planck proposed the concept of *quanta* to explain black-body radiation. In 1905, Einstein used the light quanta to explain the photoelectric effect. In 1926, Lewis named the particles of light quanta *photons*. Normally, electromagnetic

radiation tends to behave more like classical waves at lower frequencies, and more like classical particles at higher frequencies, but it never completely loses one of these two qualities. Visible light actually occupies a middle ground in frequency.

Interference and diffraction are mostly caused by the wave nature of light. Interference is used to describe the phenomenon in which two waves superimpose to form a resultant wave, and diffraction is defined as the bending of waves around the corners of an obstacle or an aperture. By the Huygens-Fresnel principle, diffraction can be considered as the collective interference of all the waves that travel through the obstacle/aperture, and thus interference becomes a special case of diffraction, in which only several divergent waves superpose with each other. Therefore, *"no one has ever been able to define the difference between interference and diffraction satisfactorily. It is just a question of usage, and there is no specific, important physical difference between them"* (Feynman).

Both interference and diffraction are essential for interferometric phase imaging. Interference can linearly convert variations in phase to the intensity change in an interferogram, allowing quantitative phase imaging. The image formation in conventional microscopy is given by both interference and diffraction, and diffraction imposes a fundamental limit on the spatial resolution.

2.1.1 Light waves

Complex representation

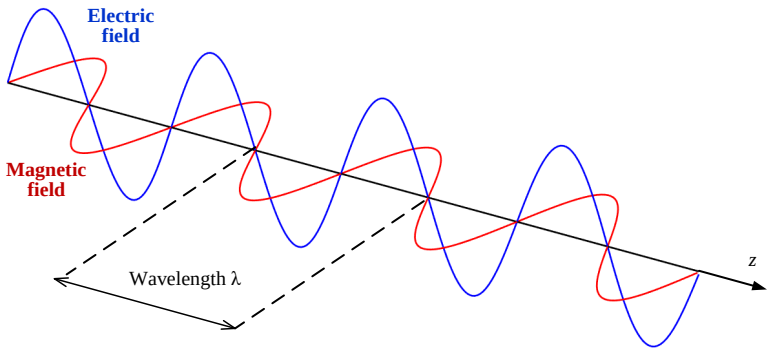

Figure 2.1: A linearly polarized light wave propagating through a homogeneous isotropic medium.

A light wave consists of synchronized electric and magnetic fields, which oscillate perpendicularly in a plane normal to the propagation direction. A simplified example of such a wave is the linearly polarized light wave (2.1), in which the two fields oscillate in a single direction. As the electric and magnetic fields are linked to each other, the wavefront can

be described by a complex field:

$$\mathbf{U}(z,t) = A(z)e^{i[\varphi(z)-\omega t]}, \tag{2.1}$$

where z stands for the coordinate along the propagation direction, t represents the time, A represents the amplitude of oscillations, φ represents the phase, and ω denotes the angular frequency.

Polarization

The transverse wave property of light can be demonstrated by polarization. The polarization state of the electric field $\mathbf{E}$ and the magnetic field $\mathbf{H}$ of light waves can be expressed by the following equation:

$$\begin{aligned} \mathbf{E}(z,t) &= \mathbf{J} \cdot E(z)e^{i[\varphi(z)-\omega t]} \\ \mathbf{H}(z,t) &= \mathbf{z}_0 \times \mathbf{E}(z,t) \\ \mathbf{J} &= \begin{bmatrix} J_x \\ J_y \end{bmatrix}, \end{aligned} \tag{2.2}$$

where $\mathbf{J}$ denotes the normalized Jones vector, and $\mathbf{z}_0$ represents the unit vector along the z-axis. Circular/elliptical polarization corresponds to light waves in which the tip of the electric or magnetic field vector describes a circular/ellipse. Right/left circular polarization indicates that the field rotates in a right-/left-hand sense along the propagation direction.

Coherence

The coherence of light describes the property of correlation between all the physical quantities of a single wave or several waves. Mathematically, the degree of coherence is defined by the coherence function [56]. Experimentally, it can be measured from the contrast (visibility) of an interferogram. Spatial coherence describes the correlation between waves at different points in space, either lateral or longitudinal. Temporal coherence describes the correlation between waves observed at different moments in time. The degree of coherence can be reduced by propagation factors such as dispersion, scattering, or diffraction. The coherence length of a light source indicates the propagation distance over which the light waves maintain a specified degree of coherence, and it's usually defined by the optical path difference with which the self-interfering pattern of the light source reaches the fringe visibility of 37% [57]. Waves with a long coherence length can be regarded as perfect sinusoidal waves. Laser devices emit photons of the same frequency, polarization,

and propagation direction, thus allowing both a remarkably high degree of coherence and a long coherence length.

Detection

Light waves oscillate at a frequency much higher than the temporal sampling frequency of photoelectric sensors, making the direct observation of the oscillation (phase) impossible. The intensity directly detected by photodetectors represents a time average of the amount of photons reaching a unit area normal to the direction of energy (power) flow. Mathematically, the directional energy flux of light can be represented by the Poynting (or Umov-Poynting) vector $\mathbf{S}$, which is defined as the time-averaged of the cross product of $\mathbf{E}$ and $\mathbf{H}$ over a full cycle T:

$$\begin{aligned}\bar{\mathbf{S}} &= \frac{1}{T}\int_0^T |\mathbf{E}\times\mathbf{H}|\mathrm{d}t = \frac{1}{T}\int_0^T EH\ \mathrm{d}t \\ &= \sqrt{\frac{\varepsilon_0\varepsilon_r}{\mu_0\mu_r}}\frac{1}{T}\int_0^T [E\cos(\varphi_0-\omega t)]^2\ \ \mathrm{d}t \\ &= \frac{1}{2}\sqrt{\frac{\varepsilon_0\varepsilon_r}{\mu_0\mu_r}}E_0^2,\end{aligned} \tag{2.3}$$

where ε_0, μ_0, ε_r, and μ_r represent the vacuum permittivity, the vacuum permeability, the relative permittivity, and the relative permeability, respectively. In engineering, the detected intensity I at a given point $\mathbf{r}$ is usually simplified as the time average of the square of amplitudes of the complex field:

$$I = \int U(\mathbf{r},t)U^*(\mathbf{r},t)\ \mathrm{d}t = A^2(\mathbf{r}). \tag{2.4}$$

Hence, photography records the intensity only and the phase is lost due to the square-law detection.

2.1.2 Interference

The total complex field of two-wave interference at any point in space or time is equal to the sum of complex fields of the two individual waves:

$$\mathbf{U}(\mathbf{r},t) = U_1(\mathbf{r})e^{i[\varphi_1(\mathbf{r})-\omega t]} + U_2(\mathbf{r})e^{i[\varphi_2(\mathbf{r})-\omega t]}. \tag{2.5}$$

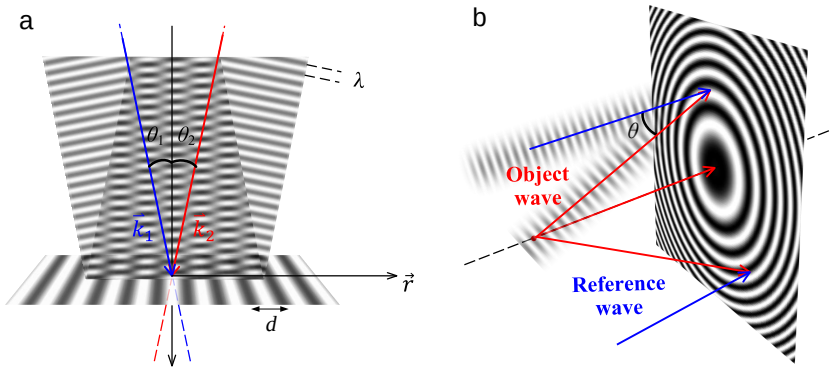

Figure 2.2: Wave interference. (a) The interference of two plane waves. (b) The interference of a plane (reference) wave and a sphere (object) wave.

The intensity of the interferogram is given by the square-law detection (Figure 2.2):

$$\begin{aligned} I(\mathbf{r}) &= \int U(\mathbf{r},t)U^*(\mathbf{r},t)\ \mathrm{d}t \\ &= U_1^2(\mathbf{r}) + U_2^2(\mathbf{r}) + U_1(\mathbf{r})U_2(\mathbf{r})e^{i[\varphi_1(\mathbf{r})-\varphi_2(\mathbf{r})]} + U_1(\mathbf{r})U_2(\mathbf{r})e^{i[\varphi_2(\mathbf{r})-\varphi_1(\mathbf{r})]} \\ &= I_1(\mathbf{r}) + I_2(\mathbf{r}) + 2\sqrt{I_1(\mathbf{r})I_2(\mathbf{r})}\cos\left[\varphi_1(\mathbf{r}) - \varphi_2(\mathbf{r})\right], \end{aligned} \tag{2.6}$$

the visibility of which can be expressed as:

$$\mathcal{C} = \frac{2\sqrt{I_1 I_2}}{I_1 + I_2}. \tag{2.7}$$

The phase difference of two waves is therefore encoded in the visible part of the interferogram. The visibility usually presents in the form of fringe patterns. For example, the interference of two ideal plane waves produces fringes of a constant spacing of d [Figure 2.2(a)], given by the geometrical arrangement of the interfering beams and the screen:

$$d = \frac{\lambda}{(\vec{k}_1 - \vec{k}_2)\cdot\vec{r}} = \frac{\lambda}{(\sin\theta_1 + \sin\theta_2)}, \tag{2.8}$$

where $\vec{k}_j$ represents the 2D wavevector of each interfering beam, and $\vec{r}$ represents the vector of the recording plane.

2.1.3 Diffraction

The scalar diffraction theory describes the diffraction phenomena mathematically based on the Huygens-Fresnel principle, by neglecting the polarization of electromagnetic waves

and assuming that the amplitude and the phase can be adequately described by a scalar variable. This section describes some of the basic diffraction phenomena based on the derivation provided by Kirchhoff [55, 58].

Diffraction integral

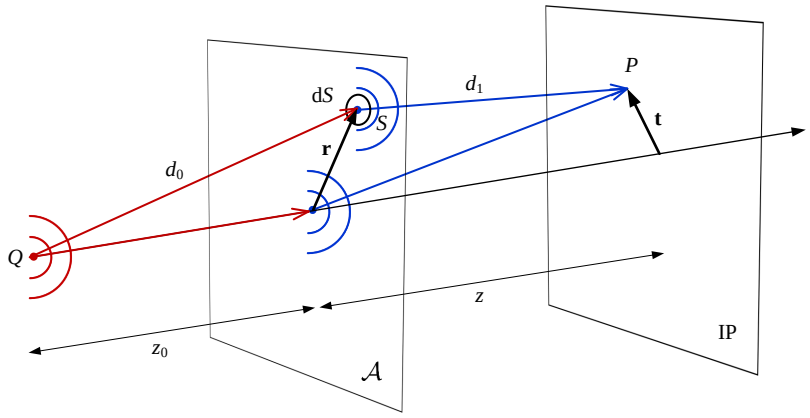

Figure 2.3: Diffraction integral of a point light source. The total complex field received at P in IP is equal to the sum of complex fields of the waves originating from the point source Q and diffracted by the mask $\mathcal{A}$.

The spherical wave emitted from Q of strength A_Q can be expressed as a scalar variable at S on $\mathcal{A}$ (Figure 2.3):

$$\mathbf{U}_S = \frac{A_Q}{d_0} e^{\mathrm{i}k_0 d_0}, \quad k_0 = \frac{2\pi}{\lambda}, \tag{2.9}$$

where k_0 represents the angular wavenumber. After $\mathbf{U}_S$ interacts with $\mathcal{A}$, the secondary emission occurs:

$$\mathbf{U}'_S = b f_S \mathbf{U}_S, \tag{2.10}$$

where b represents the strength with which the reradiation occurs, and f_S is the transmission function of $\mathcal{A}$ at S. Therefore, the total complex field observed at P on IP, which is caused by a collective effect of the secondary emission, can be expressed as an integral over $\mathcal{A}$:

$$\mathbf{U}_P = \iint_{\mathcal{A}} \frac{\mathbf{U}'_S}{d_1} e^{\mathrm{i}k_0 d_1} \mathrm{d}S = b A_Q \iint_{\mathcal{A}} \frac{f_S}{d_0 d_1} e^{\mathrm{i}k_0 (d_0 + d_1)} \mathrm{d}S. \tag{2.11}$$

By restricting the illumination to a plane wave, the total complex field can be rewritten

as:

$$\begin{aligned}\mathbf{U}_P &= \underbrace{\frac{bA_Q e^{\mathrm{i}k_0 d_0}}{d_0}}_{B} \iint_{\mathcal{A}} \frac{f(\mathbf{r})}{d_1} e^{\mathrm{i}k_0 d_1} \mathrm{d}^2\mathbf{r} \\ &\approx B \iint_{\mathcal{A}} \frac{f(\mathbf{r})}{z} e^{\mathrm{i}k_0 d_1} \mathrm{d}^2\mathbf{r} \\ &\propto \iint_{\mathcal{A}} \frac{f(\mathbf{r})}{z} e^{\mathrm{i}k_0 d_1} \mathrm{d}^2\mathbf{r}.\end{aligned} \tag{2.12}$$

Diffraction in near field and far field

Given by the interference mechanism, the intensity of a diffraction pattern is mainly determined by the phase part of light, i.e., the way in which $k_0 d_1$ changes across $\mathcal{A}$. The binomial expansion of $k_0 d_1$ can be expressed as:

$$\begin{aligned}k_0 d_1 &= k_0 z \sqrt{1 + \left(\frac{\mathbf{r}-\mathbf{t}}{z}\right)^2} = k_0 z \left[1 + \frac{1}{2}\left(\frac{\mathbf{r}-\mathbf{t}}{z}\right)^2 + \cdots\right] \\ &\approx k_0 \left[z + \frac{1}{2z}(r^2 - 2\mathbf{r}\cdot\mathbf{t} + t^2)\right].\end{aligned} \tag{2.13}$$

Herein, all the terms of high orders have been ignored by assuming that $\mathbf{r}$ and $\mathbf{t}$ are much smaller than z, which is also called the Fresnel approximation. Diffraction phenomena therefore can be classified into the Fresnel (near-field) type and the Fraunhofer (far-field) type, by the way in which d_1 changes with $\mathbf{r}$. The Fresnel diffraction occurs when the Fresnel number F verifies:

$$F = \frac{\rho^2}{\lambda z} \geq 1, \tag{2.14}$$

where ρ represents the radius of the mask $\mathcal{A}$. The integral of the Fresnel diffraction can be derived based on Equation 2.12:

$$\begin{aligned}\mathbf{U}(\mathbf{t},z) &= \frac{Be^{\mathrm{i}k_0 z}}{z} \iint_{\mathcal{A}} f(\mathbf{r}) e^{\frac{\mathrm{i}k_0(\mathbf{r}-\mathbf{t})^2}{2z}} \mathrm{d}^2\mathbf{r} = f(\mathbf{t}) \circledast \mathbf{h}(\mathbf{t},z) \\ \mathbf{h}(\mathbf{t},z) &= \frac{Be^{\mathrm{i}k_0 z}}{z} e^{\frac{\mathrm{i}k_0 \mathbf{t}^2}{2z}},\end{aligned} \tag{2.15}$$

where $\circledast$ represents the convolution operator. In other words, the total complex field of the Fresnel diffraction is proportional to the convolution of the transmission function $f(\mathbf{t})$ and the function $\mathbf{h}(\mathbf{t},z)$. Hence, $\mathbf{h}(\mathbf{t},z)$ is also called the impulse response of free space propagation.

The Fraunhofer diffraction is defined when F verifies:

$$F = \frac{\rho^2}{\lambda z} \ll 1. \tag{2.16}$$

In this case, the term r^2 in Equation 2.13 can be ignored and the basic integral in Equation 2.12 can be written as:

$$\begin{aligned} \mathbf{U}(\mathbf{t},z) &= \frac{Be^{\mathrm{i}k_0(z+\frac{t^2}{2z})}}{z} \iint_{\mathcal{A}} f(\mathbf{r}) e^{-\frac{\mathrm{i}k_0 \mathbf{r}\cdot\mathbf{t}}{z}} \mathrm{d}^2\mathbf{r} \\ &\propto [\widetilde{f}(\mathbf{t})](\frac{\mathbf{t}}{\lambda z}), \end{aligned} \tag{2.17}$$

where $\widetilde{f}(\mathbf{t})$ represents the Fourier transform of $f(\mathbf{t})$. Therefore, the total complex field of the Fraunhofer diffraction of a transmission function $f(\mathbf{t})$ is proportional to the true complex Fourier transform of the transmission function itself.

Fraunhofer diffraction by a slit

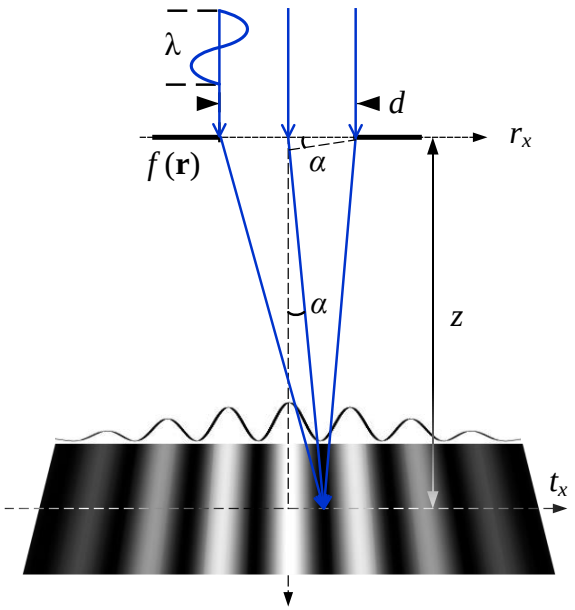

Figure 2.4: Fraunhofer diffraction by a slit, which illustrates the diffraction angles of fringe patterns.

The transmission function $f(\mathbf{r})$ is basically determined by the geometry of obstacles in the optical path. In the case of a slit of width d (Figure 2.4), the corresponding transmission

function can be expressed by:

$$f(r_x, r_y) = \begin{cases} 1 & |r_x| \leq d/2 \\ 0 & |r_x| > d/2 \end{cases}, \tag{2.18}$$

the total field of the Fraunhofer diffraction by the slit can be therefore expressed as the following based on Equation 2.17:

$$\begin{aligned} \mathbf{U}(t_x, t_y) &= \frac{Be^{\mathrm{i}k_0(z+\frac{t^2}{2z})}}{z} \iint_{\mathcal{A}} f(\mathbf{r}) e^{-\frac{\mathrm{i}k_0 \mathbf{r}\cdot\mathbf{t}}{z}} \mathrm{d}^2\mathbf{r} \\ &\propto \int_{-d/2}^{d/2} e^{-\frac{\mathrm{i}k_0 t_x r_x}{z}} \mathrm{d}r_x \int_{-\infty}^{\infty} e^{-\frac{\mathrm{i}k_0 t_y r_y}{z}} \mathrm{d}r_y \\ &\propto \mathrm{sinc}(\frac{\pi d t_x}{\lambda z}) \int_{-\infty}^{\infty} e^{-\frac{\mathrm{i}k_0 t_y r_y}{z}} \mathrm{d}r_y, \end{aligned} \tag{2.19}$$

where $\mathrm{sinc}(x)$ represents $\sin(x)/x$. The corresponding intensity distribution along the axis $t_y = 0$ is thus given by:

$$\begin{aligned} |\mathbf{U}(t_x, 0)|^2 &\propto \mathrm{sinc}^2(\frac{\pi d t_x}{\lambda z}) \\ &\propto \mathrm{sinc}^2(\frac{\pi d \sin\alpha}{\lambda}), \end{aligned} \tag{2.20}$$

where α represents the observation angle. The intensity function has its minima at $\mathrm{sinc}(x) = 0$, which indicates the diffraction angle α_m caused by a fringe pattern:

$$\sin\alpha_m = m\lambda/d. \tag{2.21}$$

Fraunhofer diffraction by an aperture

The Fraunhofer diffraction by an aperture is highly important (Figure 2.5), as most optical components for imaging in the industry are characterized by a centrosymmetric pupil function, such as imaging lenses. To describe the diffraction caused by centrosymmetric transmission functions, the basic integral in Equation 2.17 can be expressed with the polar coordinates:

$$\begin{aligned} \mathbf{U}(t, \phi) &\propto \int_0^{2\pi} \int_0^{\infty} e^{-\frac{\mathrm{i}k_0}{z}(rt\cos\phi\cos\theta + rt\sin\phi\sin\theta)} r \ \mathrm{d}r \ \mathrm{d}\theta \\ &\propto \int_0^{2\pi} \int_0^{\infty} e^{-\frac{\mathrm{i}k_0}{z} rt\cos(\phi-\theta)} r \ \mathrm{d}r \ \mathrm{d}\theta. \end{aligned} \tag{2.22}$$

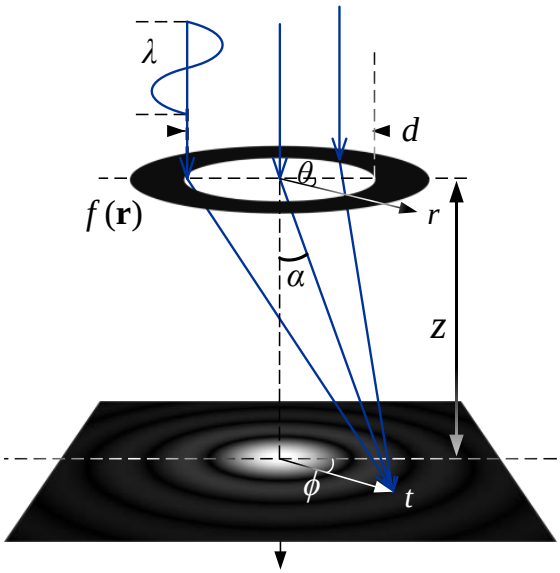

Figure 2.5: Fraunhofer diffraction by an aperture, which illustrates the spatial resolution of diffraction-limited optical systems.

By assuming the transmission function to be a centrosymmetric annulus with the larger circle of radius $(a+\delta a)$ and the smaller circle of radius a, Equation 2.22 can be rewritten as:

$$\begin{aligned}
\mathbf{U}_A(t,0) &\propto \int_0^{2\pi}\int_a^{a+\delta a} e^{-\frac{\mathrm{i}k_0}{z}rt\cos\theta} r\ \mathrm{d}r\ \mathrm{d}\theta \\
&\propto a\delta a\int_0^{2\pi} e^{-\frac{\mathrm{i}k_0}{z}at\cos\theta}\ \mathrm{d}\theta \\
&\propto a\delta a\cdot 2\pi J_0(\frac{k_0 at}{z}) \\
&\propto a\delta a\cdot 2\pi J_0(k_0 a\sin\alpha),
\end{aligned} \tag{2.23}$$

where J_0 represents the zero-order Bessel function. Equation 2.23 can be further extended to describe the Fraunhofer diffraction by a circular aperture of radius R:

$$\begin{aligned}
\mathbf{U}_C(\sin\alpha,0) &\propto 2\pi\int_0^R r\cdot J_0(k_0 r\sin\alpha)\ \mathrm{d}r \\
&\propto 2\pi\frac{1}{(k_0\sin\alpha)^2}\int_0^{(k_0\sin\alpha)R} k\cdot J_0(k)\ \mathrm{d}k \\
&\propto 2\pi R^2\frac{J_1[(k_0\sin\alpha)R]}{(k_0\sin\alpha)R},
\end{aligned} \tag{2.24}$$

where J_1 represents the first-order Bessel function. The intensity function has its first

minimum at $J_1(x) = 0$, which indicates the angular resolution α of optical imaging systems (see detailed discussion in Section 2.4):

$$\begin{aligned} &\mathbf{U}_C(\sin\alpha, 0)^2 \propto \{J_1[(k_0 \sin\alpha)R]\}^2 = 0 \\ &\frac{\pi d \sin\alpha}{\lambda} = 3.8317, 7.0156, \cdots \\ &\sin\alpha \approx 1.22\frac{\lambda}{d}, \cdots . \end{aligned} \tag{2.25}$$

2.1.4 Holographic reconstruction

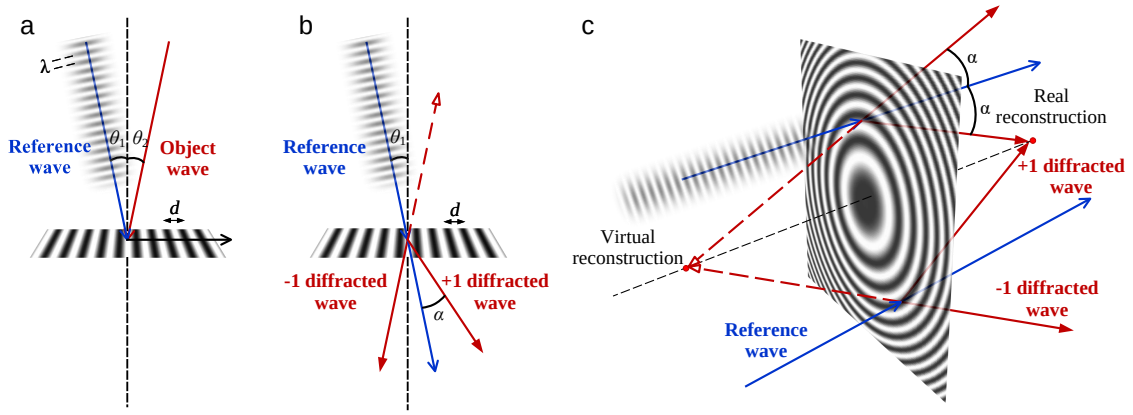

Figure 2.6: Principle of holographic reconstruction. (a) Interferometric recording: a hologram is produced by the interference of two plane waves, and it can be considered as a diffraction grating of frequency $1/d$. (b) Holographic reconstruction: by illuminating the hologram with the same reference wave, the fringe pattern in the hologram diffracts the reference wave with a diffraction angle of α. (c) A real image and a virtual image can be reconstructed simultaneously by the ± 1 diffracted waves.

Holographic recording is achieved by interfering the object wave with a reference wave [Figure 2.6(a)]. The spacing d of interference fringes in a hologram is given by Equation 2.8. The holographic reconstruction can be described by considering the hologram as a diffraction grating [Figure 2.6(b)]. By combining Equations 2.8 and 2.21, the angle of the first-order diffraction α can be calculated by:

$$\sin\alpha = \lambda/d = \sin\theta_1 + \sin\theta_2. \tag{2.26}$$

Hence, by illuminating the hologram with a wave identical to the reference wave, a real image and a virtual image of the object can be reconstructed simultaneously by the ± 1 diffracted waves [Figure 2.6(c)].

2.2 Optical interferometry

In the 1880s, a Michelson interferometer was firstly employed to disprove the existence of *aether* [48], a postulated medium proposed most famously by Fresnel for light propagation. Since the 1960s, optical interferometers were identified as a natural fit for the detection of gravitational waves in space and time. In 2015, the first direct detection of gravitational waves was achieved by LIGO [11], which was awarded the Nobel Prize in Physics in 2017. Now, optical interferometry has been applied for various metrology purposes. This section illustrates three types of interferometric configurations and some basic knowledge of speckle interferometry, which are involved in the own developed methods in the next chapters.

2.2.1 Interferometric configurations

Off-axis interferometers

An off-axis (Leith-Upatnieks) interferometer normally operates by tilting one of the interfering waves to introduce a small angle. The complex field of an oblique incident wave can be expressed as:

$$\mathbf{U}_j(\mathbf{r}) = U_j(\mathbf{r})e^{i\left[\varphi_j(\mathbf{r})+\vec{k}_j\cdot\vec{r}\right]}, \tag{2.27}$$

where $\vec{k}_j$ represents the 3D wavevector of the wavefront, and $\vec{r}$ represents the vector of the recording plane. The superposition of such two waves gives rise to an interferogram expressed by:

$$\begin{aligned} I(\mathbf{r}) = [\mathbf{U}_1(\mathbf{r}) + \mathbf{U}_2(\mathbf{r})]^2 &= \{U_1(\mathbf{r})e^{i\left[\varphi_1(\mathbf{r})+\vec{k}_1\cdot\vec{r}\right]} + U_2(\mathbf{r})e^{i\left[\varphi_2(\mathbf{r})+\vec{k}_2\cdot\vec{r}\right]}\}^2 \\ &= D(\mathbf{r}) + C(\mathbf{r})e^{i\left(\vec{k}_1-\vec{k}_2\right)\cdot\vec{r}} + C^*(\mathbf{r})e^{-i\left(\vec{k}_1-\vec{k}_2\right)\cdot\vec{r}}, \end{aligned} \tag{2.28}$$

and its Fourier transform can be expressed as:

$$\tilde{I}(\mathbf{k}) = \tilde{D}(\mathbf{k}) + \tilde{C}\left(\mathbf{k}-\boldsymbol{\nu}\right) + \tilde{C}^*\left(\mathbf{k}+\boldsymbol{\nu}\right), \tag{2.29}$$

where the vector $\boldsymbol{\nu}$ represents the vector of carrier frequencies in the frequency domain (Fourier domain or k-space), which equals $(\vec{k}_1 - \vec{k}_2)/\lambda$.

Off-axis interferometry achieves single-shot phase imaging at the expense of a limited SBP. SBP is a fundamental parameter to evaluate the performance or the price of an optical system, which is defined as the pure number that counts the degree of freedom for imaging. For a system with an input area of size $|x| < \Delta x/2$ and the sampling spacing

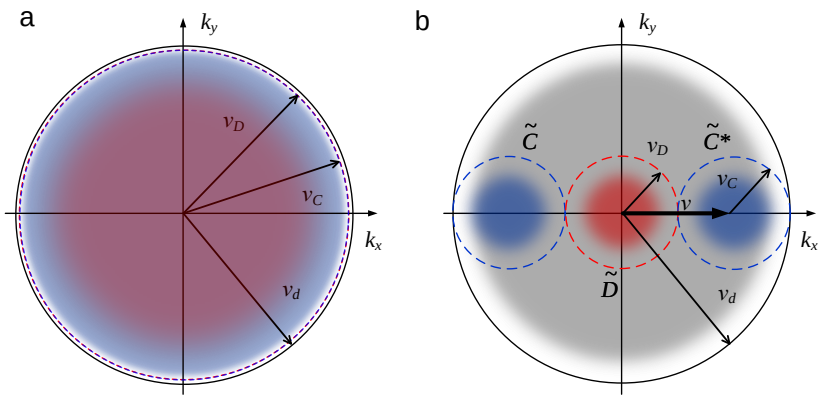

Figure 2.7: The Fourier spectra of (a) an in-line interferometer and (b) an off-axis interferometer. ν_D, the maximal frequency of the direct current (DC) term. ν_C, the maximum frequency of the conjugate (cross-correlation) terms. ν_d, the maximal sampling frequency of the detector.

δx, the SBP can be calculated from the Wigner distribution by:

$$\mathcal{S} = \Delta x/\delta x = \Delta x \Delta \nu, \tag{2.30}$$

where $\Delta\nu$ represents the sampling frequency. For a digital imaging system, the SBP is basically determined by both the optical components and the digital detectors. The SBP of off-axis interferometry is usually limited by the digital detectors, due to the necessity of a carrier frequency (Figure 2.7). For a given detector, the SBP can be illustrated by calculating the percentage of the area occupied by the conjugate terms in the frequency domain. As both the phase and the amplitude channels contribute independently in a complex-field imaging system, the SPB of an off-axis interferometer can be quantified as the following [Figure 2.7(b)]:

$$\mathcal{S}_{\text{off-axis}} = 2\left(\frac{\nu_C}{\nu_d}\right)^2 \cdot \mathcal{S}_d = \frac{2}{9}\mathcal{S}_d, \tag{2.31}$$

where $\mathcal{S}_d$ represents the maximum SBP permitted by the detector, which equals $\sim$1/4 of its pixel number by the Nyquist–Shannon sampling theorem.

Image-shearing interferometers

For the measurements of strains or bending moments, the displacement components directly obtained with interferometry must be differentiated once or twice to yield slopes or curvatures, which is time-consuming and may lead to errors in the final results. The

first-order differential operation can be performed optically by using an image-shearing interferometer. Instead of interfering the object wave with a separate reference wave, the image-shearing interferometer compares the object wave with a shifted copy of itself. For example, a lateral-shearing interferometer operates by using a laterally shifted copy of the object wave:

$$I(\mathbf{r}) = I_1(\mathbf{r}) + I_2(\mathbf{r}+\delta\mathbf{r}) + 2\sqrt{I_1(\mathbf{r})I_2(\mathbf{r}+\delta\mathbf{r})}\cos\left[\varphi_1(\mathbf{r}) - \varphi_2(\mathbf{r}+\delta\mathbf{r})\right], \tag{2.32}$$

where $\delta\mathbf{r}$ represents the lateral shear amount. A common-path image-shearing interferometric system can be simply achieved by adopting optical shearing devices, such as partial reflectors, double-layer glass plates, gratings, Fresnel prisms, or cube beam splitters. The sensitivity of the first-order differential of displacements and the robust common-path configuration make image-shearing interferometers especially useful in industrial NDT.

Point diffraction interferometers

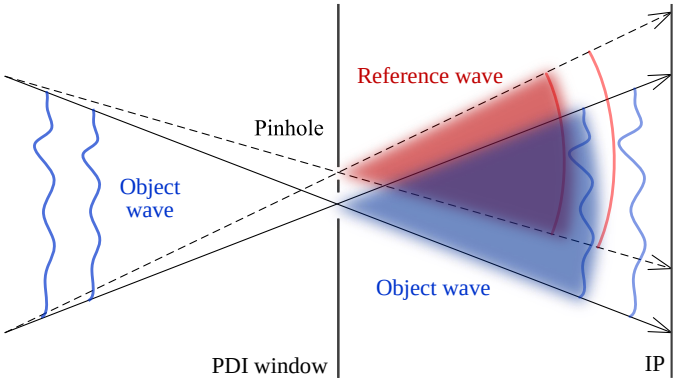

Figure 2.8: Principle of PDIs. A portion of the object wave is diffracted by a pinhole to generate a quasi plane reference wave.

A point diffraction interferometer (PDI) can be achieved by spatial filtering (Figure 2.8). In this configuration, a small portion of the object wave is diffracted to generate a reference wave, which travels through almost the same optical path as the transmitted object wave. A PDI is sensitive to a wavefront itself, rather than its first-order differential, while maintaining a quasi common-path configuration. This feature is highly demanded in the field of digital holographic microscopy, where both high temporal phase stability and a large FOV are required.

2.2.2 Speckle interferometry

By utilizing the laser speckle effect, speckle interferometry is capable of measuring a variety of mechanical properties of surfaces with arbitrary microstructures, including displacements, strains, surface roughness, rotations, and vibrations.

Speckle effect

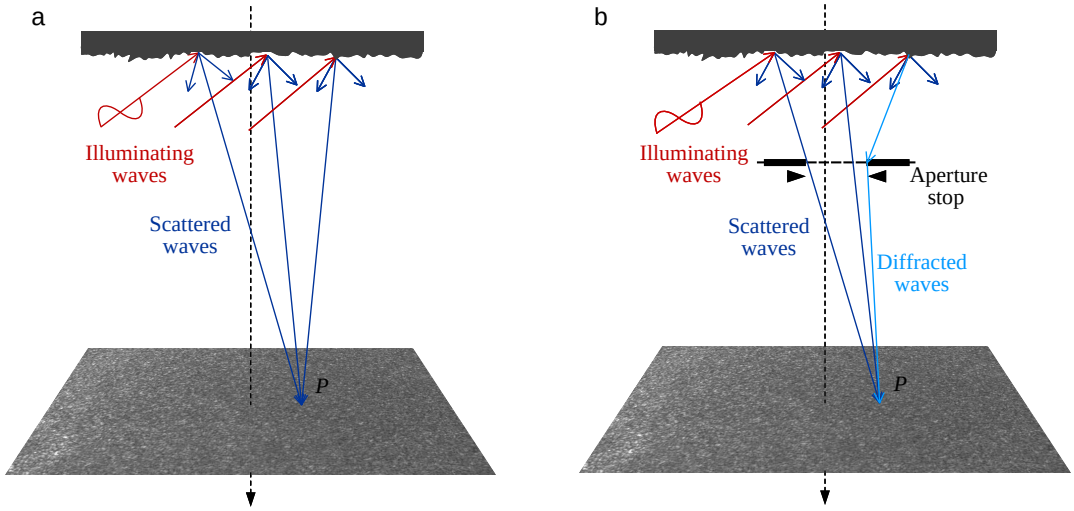

Figure 2.9: Formation of laser speckles. (a) Objective speckles: the waves scattered from an optically rough surface recombine in the observation screen and interfere to produce speckle patterns. (b) Subjective/imaged speckles: the waves scattered from an optically rough surface pass through an aperture and diffraction occurs. The scattered waves and the diffracted waves recombine in the observation screen and interfere to produce speckle patterns.

The speckled appearance of diffuse surfaces under coherent illumination is usually referred to as the laser speckle effect. In this phenomenon, highly coherent incident waves interact with an optically rough surface and get scattered. The scattered waves of random phases act as secondary coherent light sources and interfere with each other on an observation screen. When no imaging system is involved, grainy or speckled patterns termed objective speckles appear [Figure 2.9(a)]. When an imaging system is placed between the rough surface and the screen, speckles with a grain size limited by the numerical aperture of the system can be observed, which are termed subjective/imaged speckles [Figure 2.9(b)]. All the waves contribute to the final intensity at each point on the screen: the sum of amplitudes determines the average intensity, while the sum of phases gives rise to the distinct maxima and minima. The total complex field at each point on the screen can be

expressed as:

$$\mathbf{U}_P = \frac{1}{\sqrt{N}} \sum_{m=1}^{N} U_m \cdot e^{i\varphi_m}. \tag{2.33}$$

Sensitivity vectors

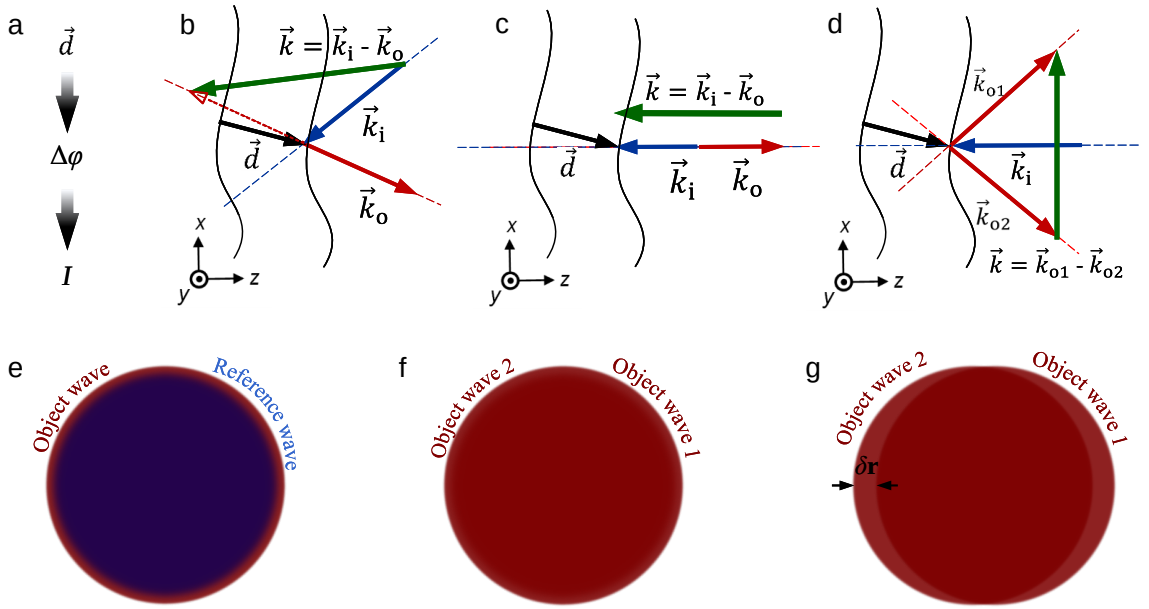

Figure 2.10: Sensing mechanism of speckle interferometry. (a) The simplified process of displacement sensing. A generalized sensitivity vector (b), and the customized sensitivity vectors for measuring (c) pure out-of-plane displacements and (d) pure in-plane displacements. (e) and (f), The corresponding wave interference arrangements of (c) and (d). (g) The wave interference arrangement for measuring phase gradients with shear amount δr.

The capability of speckle interferometry to measure surface displacements is achieved by extracting phase changes from the speckle field reorientation (intensity changes) [Figure 2.10(a)]. Sensitivity vectors determine the way in which the relative phase [or optical path difference (OPD)] changes with the surface displacement. The arrangement of wave interference defines which physical quantity the obtained phase corresponds to and converts the phase variation to the intensity difference in an interferogram. The sensitivity vector is defined by the difference between the wave vectors of illumination $\vec{k}_i$ and observation $\vec{k}_o$ [Figure 2.10(b)]. By considering the total effect of the surface displacements $\vec{d}$ along all directions on the optical path change, the phase difference $\Delta\varphi$ can be calculated by using a sensitivity vector:

$$\Delta\varphi = \frac{2\pi}{\lambda}(\vec{k}_i - \vec{k}_o) \cdot \vec{d} = \frac{2\pi}{\lambda}\vec{k} \cdot \vec{d}. \tag{2.34}$$

A flexible sensitivity can be achieved by eliminating the effect of unwanted components from the initial result. For example, $\vec{k}_i$ and $\vec{k}_o$ can be designed to be in opposite directions normal to the sample surface for measuring pure out-of-plane displacements [Figure 2.10(c)]. A pure in-plane sensitivity vector can be also achieved by setting two observation vectors ($\vec{k}_{o1}$ and $\vec{k}_{o2}$) symmetric about the normal direction of the sample surface [Figure 2.10(d)]. The phase change caused by the out-of-plane displacements [Figure 2.10(c)] can be recorded by interfering the object wave with a reference wave [Figure 2.10(e)], while the phase change caused by pure in-plane measurements can be recorded by interfering the two object waves symmetrically observed in Figure 2.10(d) [Figure 2.10(f)]. Phase gradients can be measured by interfering two object waves with a shear amount [Figure 2.10(g)].

2.3 Fourier method

In 1822, the Fourier series was introduced to express some functions as a sum of discrete sinusoidal harmonics of their fundamental frequencies [55], which eventually developed into Fourier transform. Fourier transform and the related methods provide a "language" in which many phenomena in physics and engineering can be easily discussed, not only for the analysis but also for the synthesis purposes. The Fourier method is especially useful in the field of communication, in which systems are designed to collect information. It has also achieved significant advances in the fields of optics and imaging, such as interferometry, holography, and microscopy, which deal with wave phenomena and frequencies.

2.3.1 Fourier transform

Fourier series

Fourier series expand a periodic function $f(t)$ to an infinite sum of sines and cosines:

$$\begin{aligned} f(t) &= A_0 + \sum_{n=1}^{\infty} A_n \cos\left(n\omega t - \varphi_n\right) \\ &= A_0 + \sum_{n=1}^{\infty} \underbrace{A_n \cos\varphi_n}_{a_n} \cos(n\omega t) + \sum_{n=1}^{\infty} \underbrace{A_n \sin\varphi_n}_{b_n} \sin(n\omega t), \end{aligned} \tag{2.35}$$

where $\cos(n\omega t)$ and $\sin(n\omega t)$ are orthogonal to each other, forming an orthonormal basis of the space. Therefore, the associated parameters can be determined by considering the

orthogonality:

$$\begin{aligned} A_0 &= \int f(t)\ \mathrm{d}t \\ a_n &= \int f(t) \cdot \cos(n\omega t)\ \mathrm{d}t \\ b_n &= \int f(t) \cdot \sin(n\omega t)\ \mathrm{d}t. \end{aligned} \tag{2.36}$$

By using Euler's formula, $\cos(n\omega t - \varphi_n)$ can be also expressed in the form of complex functions:

$$\begin{aligned} \cos(n\omega t - \varphi_n) &= \frac{1}{2} e^{i(n\omega t - \varphi_n)} + \frac{1}{2} e^{-i(n\omega t - \varphi_n)} \\ &= \frac{1}{2} e^{-i\varphi_n} \cdot e^{in\omega t} + \frac{1}{2} e^{i\varphi_n} \cdot e^{-in\omega t}, \end{aligned} \tag{2.37}$$

with which $f(t)$ can be expressed as:

$$f(t) = \sum_{n=-N}^{N} c_n \cdot e^{in\omega t}, \tag{2.38}$$

and the parameters can be determined by:

$$c_n = \left\{ \begin{array}{lll} A_0, & & n = 0 \\ \frac{1}{2} A_n e^{-i\varphi_n} & = \frac{1}{2}(a_n - ib_n), & n > 0 \\ \frac{1}{2} A_n e^{i\varphi_n} & = \frac{1}{2}(a_n + ib_n), & n < 0 \end{array} \right\} = \int f(t) \cdot e^{-in\omega t}\ \mathrm{d}t. \tag{2.39}$$

Thus, the Fourier series of a function can be derived by measuring the harmonics with the orthonormal vectors by multiplication.

Fourier transform

The term "Fourier transform" usually represents both the mathematical transforming operation and the Fourier domain representation. The mathematical operation of the Fourier transform decomposes a function of space or time into the corresponding function of spatial or temporal frequencies, i.e., its Fourier transform representation. The representation is a complex function, whose magnitudes (absolute values) indicate the amounts of the basic sinusoids at the corresponding frequencies in the original function, while the arguments (angles) represent the corresponding phases of the sinusoids. Mathematically, the 1D Fourier transform of function $f(t)$ is defined by:

$$\mathcal{F}[f(t)](\xi) = \widetilde{f}(\xi) = \int_{-\infty}^{\infty} f(t) e^{-i2\pi\xi t}\ \mathrm{d}t, \quad \forall \xi \in \mathbb{R}, \tag{2.40}$$

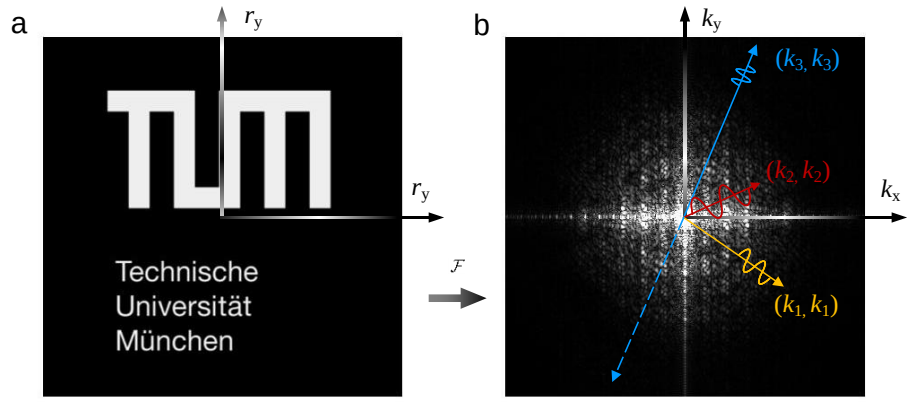

Figure 2.11: 2D Fourier transform. (a) A sample image and (b) its Fourier transform.

where t represents the variable of time or space, and ξ represents the variable of temporal or spatial frequencies. The inverse Fourier transform $\mathcal{F}^{-1}$ recovers the original function from its frequency domain representation via an integral operation with the inverse orthonormal basis, $e^{i2\pi t}$. The 1D Fourier transform can be easily extended to higher dimensional spaces. For example, the 2D Fourier transform of $f(\mathbf{r})$ can be expressed by a double integral (Figure 2.11):

$$\widetilde{f}(\mathbf{k}) = \int_{-\infty}^{\infty}\int_{-\infty}^{\infty} f(\mathbf{r})e^{-i2\pi\mathbf{k}\cdot\mathbf{r}}\ \mathrm{d}\mathbf{r}. \tag{2.41}$$

2.3.2 Convolution theorem

Convolution is a mathematical operation that represents two functions by a third function to show how the shape of one function is modified by the other one. The 1D convolution of $f(t)$ and $g(t)$ is defined by:

$$[f(t) \circledast g(t)](\tau) = \int_{-\infty}^{\infty} f(t)g(\tau - t)\ \mathrm{d}t. \tag{2.42}$$

Basically, the result of convolution indicates the area under $f(t)$ weighted by $g(-t)$ shifted by τ, emphasizing different parts of $f(t)$. Convolution can be performed through Fourier transform. More specifically, under suitable conditions, the convolution of two functions in time or space is equivalent to the pointwise product of their Fourier transforms in the frequency domain, which is known as the *convolution theorem* and can be simply proved

by:

$$\begin{aligned}
\mathcal{F}\{[f(t) \circledast g(t)](\tau)\}(\xi) &= \int_{-\infty}^{\infty} \left[\int_{-\infty}^{\infty} f(t) g(\tau - t) \, \mathrm{d}t \right] e^{-2\pi i \xi \cdot \tau} \, \mathrm{d}\tau \\
&= \int_{-\infty}^{\infty} f(t) \left[\int_{-\infty}^{\infty} g(\tau - t) e^{-2\pi i \xi \cdot \tau} \, \mathrm{d}\tau \right] \, \mathrm{d}t \\
&= \int_{-\infty}^{\infty} f(t) \left[\int_{-\infty}^{\infty} g(y) e^{-2\pi i \xi \cdot (y+t)} \, \mathrm{d}y \right] \, \mathrm{d}t \\
&= \int_{-\infty}^{\infty} f(t) e^{-2\pi i \xi \cdot t} \, \mathrm{d}t \int_{-\infty}^{\infty} g(y) e^{-2\pi i \xi \cdot y} \, \mathrm{d}y \\
&= \widetilde{f}(\xi) \cdot \widetilde{g}(\xi).
\end{aligned} \tag{2.43}$$

2.3.3 Hilbert transform

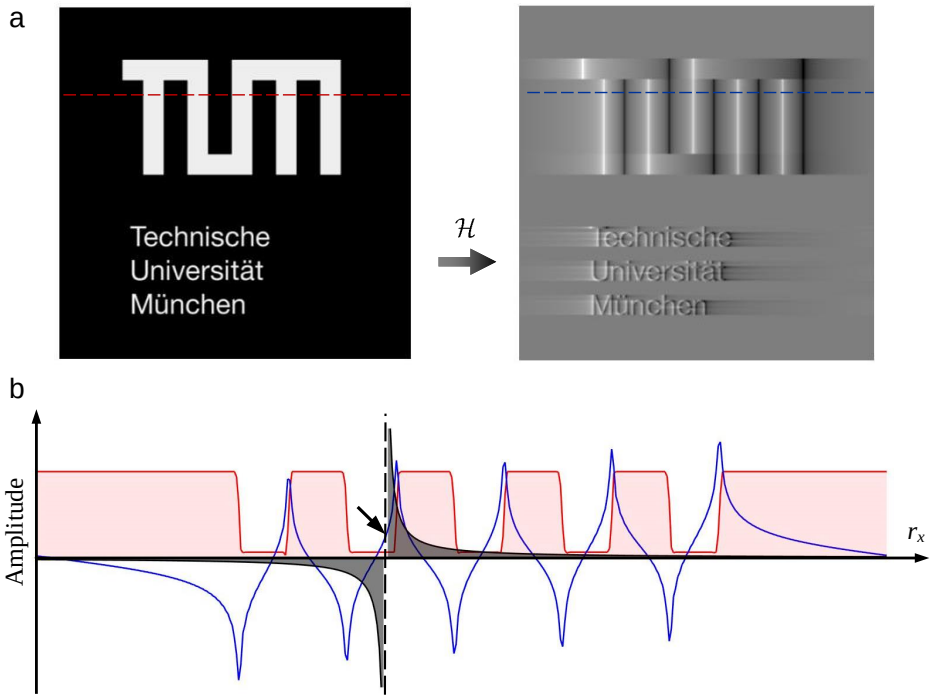

Figure 2.12: Principle of Hilbert transform. (a) A sample image and its Hilbert transform. (b) The convolutional representation of the Hilbert transform. The data is taken along the dashed lines in (a).

The Hilbert transform is another linear operator, which can convert a real-valued signal into another real-valued signal with a phase shift under suitable conditions. It is often used to compute the imaginary part from the real part of a function (or vice versa). In engineering, it is also known by the name the Kramers–Kronig relations.

Mathematically, the Hilbert transform of $f(t)$ is defined as the convolution of $f(t)$ with the Cauchy kernel, $g(t) = 1/t$. Since $1/t$ is not integrable at $t = 0$, the Hilbert transform can be represented with the Cauchy principal value (Figure 2.12):

$$\begin{aligned}\mathcal{H}[f(t)](\tau) &= f(t) \circledast \frac{1}{\pi t} \\ &= \frac{1}{\pi}\mathrm{p}\cdot\mathrm{v}\cdot\int_{-\infty}^{+\infty}\frac{f(t)}{\tau - t}\mathrm{d}t \\ &= -\frac{1}{\pi}\lim_{\varepsilon\to 0}\int_{\varepsilon}^{\infty}\frac{f(t+\tau) - f(-t+\tau)}{t}\mathrm{d}t.\end{aligned} \tag{2.44}$$

The phase-shifting property of the Hilbert transform can be proved through the convolution theorem:

$$\begin{aligned}\mathcal{F}\{\mathcal{H}[f(t)]\}(\xi) &= \widetilde{f}(\xi)\cdot\mathcal{F}(\frac{1}{\pi t}) \\ &= -i\,\mathrm{sgn}(\xi)\cdot\widetilde{f}(\xi),\end{aligned} \tag{2.45}$$

where $-i\,\mathrm{sgn}$ is defined by:

$$-i\,\mathrm{sgn}(\xi) = \begin{cases} i = e^{+\frac{i\pi}{2}}, & \xi < 0 \\ 0, & \xi = 0 \\ -i = e^{-\frac{i\pi}{2}}, & \xi > 0 \end{cases} \tag{2.46}$$

Hence, the Hilbert transform works as a multiplier operator which acts on a function by altering its Fourier transform. After applying a Hilbert transform, the phase of the negative frequency components of $f(t)$ can be shifted by $+\pi/2$, while the phase of the positive parts can be shifted by $-\pi/2$. Naturally, applying the Hilbert transform twice can shift the phase of the negative and the positive frequency components by $+\pi$ and $-\pi$, respectively. However, the Hilbert transform is not suitable for nonstationary and nonlinear real-world signals. To overcome this limitation, the Hilbert-Huang transform (HHT) is developed, which operates by decomposing a signal into so-called intrinsic mode functions (IMFs) along with a trend iteratively through the empirical mode decomposition (EMD) and applying the Hilbert transform to the IMFs to obtain the instantaneous frequency data [59].

2.3.4 Instantaneous phase retrieval

Fourier transform can convert a linear operation performed in one domain into the corresponding operation in another domain for easier operations. One example is that the Fourier transform has been proved to be particularly useful for the instantaneous phase retrieval of fringe patterns. Interferograms obtained using off-axis interferometers can be

described by Equation 2.28, in which the amplitude of the carrier frequency is required to be at least 2-times larger than the maximum frequency of the DC term [Figure 2.7(b)]. Therefore, after applying a Fourier transform, multiple components of the interferogram can be separated in the frequency domain. By selecting one of the conjugate terms (C and C^*) and applying an inverse Fourier transform, the instantaneous phase or the local phase carried by the carrier frequency can be totally extracted:

$$\varphi(\mathbf{r}) = \arg\{\mathcal{F}^{-1}[\tilde{C}(\mathbf{k} - \boldsymbol{\nu})]\}. \tag{2.47}$$

Instantaneous phase retrieval can be also achieved by utilizing the digital phase-shifting property of Hilbert transform and applying HHT:

$$\varphi(t) = \arg\{f(t), \mathcal{H}[f(t)]\}. \tag{2.48}$$

2.3.5 Optical Fourier transform by a lens

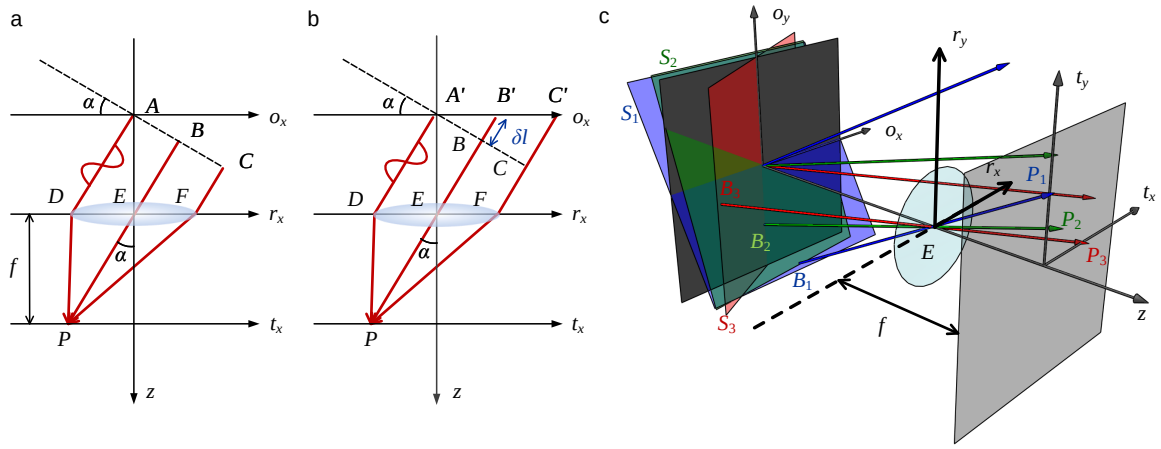

Figure 2.13: The physical Fourier-transforming property of a lens. (a) The plane wave ABC is focused at P on the focal plane of a lens. (b) The optical path of the plane wave $A'B'C'$ passing through the same lens. (c) The optical path in 3D. The plane wave S_1 with the normal vector B_1-P_1 is focused at P_1 on the focal plane.

One remarkable property of a converging lens is its inherent ability to perform the optical 2D Fourier transform. By the principle of geometric optics, a plane wave can be focused at a point on the focal plane by an imaging lens [Figure 2.13(a)]. According to Fermat's principle, the path lengths from the various points on the wavefront to their focal point are all equal, i.e., $l_{ADP} = l_{BEP} = l_{CFP}$. The optical path length of any points on the wavefront $A'B'C'$ can be consequently represented by the sum of the constant path length l_{ADP}

and a path length change δl [Figure 2.13(b)]. For example, the path length $l_{B'EP}$ can be calculated from the 3D plane function of ABC [Figure 2.13(c)]:

$$\begin{aligned} &lx + my + z = 0 \\ &l_{B'EP} = l_{BEP} + \delta l_B = l_{BEP} - (lx + my), \end{aligned} \tag{2.49}$$

and the basic diffraction integral in Equation 2.12 can be therefore rewritten as:

$$\begin{aligned} \mathbf{U}_p &= B \iint \frac{f(\mathbf{r})}{z} e^{\mathrm{i}k_0 d_1} \mathrm{d}^2\mathbf{r} \\ &= \frac{B}{f} \iint f(x,y) e^{\mathrm{i}k_0 l_{B'EP}} \mathrm{d}x \ \mathrm{d}y \\ &= \frac{B}{f} e^{\mathrm{i}k_0 l_{BEP}} \iint f(x,y) e^{-\mathrm{i}k_0(lx+my)} \mathrm{d}x \ \mathrm{d}y \\ &= \frac{B}{f} e^{\mathrm{i}k_0 l_{BEP}} \mathcal{F}[f(x,y)](\frac{l}{\lambda}, \frac{m}{\lambda}). \end{aligned} \tag{2.50}$$

Hence, the total complex field on the focal plane of a lens represents the true complex 2D Fourier transform of the transmission function $f(\mathbf{r})$, revealing a well-known theory of image formation: in a lens-based imaging system, the image, which is an inverted and magnified copy of the object, is formed through a Fourier transform caused by the Fraunhofer diffraction and an inverse Fourier transform caused by the lens focusing.

2.4 Light microscopy

Light microscopy can date back to at least the 17th century. Over centuries, much of the effort has been devoted to improving the performance in two main aspects: resolution and contrast.

In microscopy, as the sample size is usually equal to or even less than the wavelength of illumination, light bends and diffraction occurs due to the wave nature. Geometrical optics considers light waves as rays, giving no information on the ultimate resolving power of a microscope. The improvement of lens manufacturing techniques mainly solves the problem of image distortions and chromatic aberrations. In 1835, Airy reported "the form and brightness of the rings or rays surrounding the image of a star as seen in a good telescope". This phenomenon is also known as the *Airy disc* or the *Airy pattern* [60], which indicates that the resolving power of an optical imaging system is no longer limited by imperfections in the lens but only by diffraction. In 1873, Abbe published a theory to explain the diffraction limit of microscopy [61, 62]. Abbe's theory illustrates the ultimate resolution limit of an optical system given by diffraction, which is known as *Abbe*

diffraction limit. In 1879, based on Airy's work, Rayleigh proposed a criterion to describe the ability of a diffraction-limited system to distinguish small details in objects [63]. Over the past two decades, several fluorescence microscopy techniques have been invented to achieve "super-resolution" imaging by circumventing the Abbe limit, including structured illumination microscopy (SIM) [64], stimulated emission depletion technology (STED) [65], fluorescence photoactivation localization microscopy (PALM) [66], and stochastic optical reconstruction microscopy (STORM) [67].

Contrast enhancements are usually achieved by utilizing special light-matter interactions. For example, phase contrast imaging utilizes the fact that the phase-shift section can be much larger than the absorption section in certain spectrum regions, such as X-rays [1]. Fluorescence microscopy uses fluorescence instead of or in addition to, scattering, reflection, attenuation, or absorption to generate images [68].

2.4.1 Diffraction-limited imaging

Airy Disk

Caused by the Fraunhofer diffraction by a circular aperture (Equation 2.24), the Airy disk is featured by a bright central region, together with a series of concentric rings around. The Airy disk describes the best-focused spot of light that a perfect lens-based imaging system can make, limited by diffraction. Optical systems in which the resolution is no longer limited by imperfections in the lenses, but rather by diffraction, are said to be diffraction-limited.

Abbe's theory of image formation

"The microscope image is the interference effect of a diffraction phenomenon" (Abbe). Abbe's theory clearly illustrates the relationship between the resolution limit and the wavelength in a diffraction-limited system [69]. It describes image formation as a two-step process: diffraction in the object plane and interference in the imaging plane (Figure 2.14). The sample of microscopy is simplified as a diffraction grating, and the interference fringes represent a magnified image of the grating. The following phenomena can be observed, which illustrates the essence of the resolution limit: if no diffracted waves from the grating are collected by the objective, no image appears on IP; if only the diffracted waves of low orders are collected, interference fringes of relatively large spacing can be generated; if the diffracted waves of high orders are collected, interference fringes of small spacing can be generated. For example, assuming that only the diffracted waves of a maximum order of +2 are collected, the minimum spacing d, which represents the finest

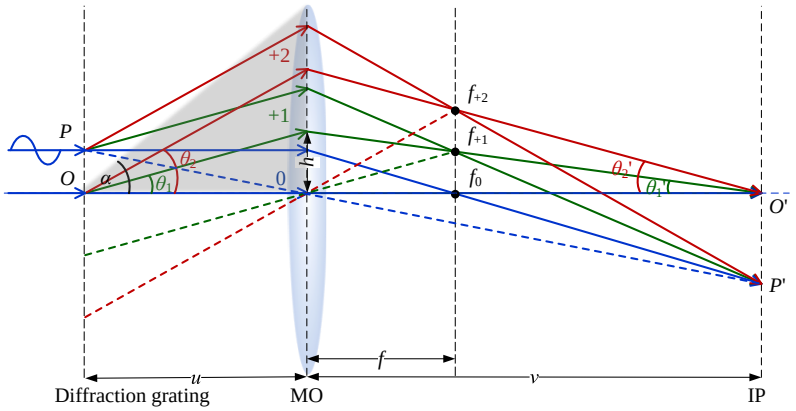

Figure 2.14: Abbe's theory of image formation. The object is simplified as a diffraction grating of spacing d. The grating diffracts the illumination wave, and only some of the diffracted waves are collected by the objective lens and focused on the focal plane. The focused spots recombine on IP, producing interference fringes of spacing d'.

observable details, can be calculated by combining Equations 2.8 and 2.21:

$$d = \frac{d'}{M} = \frac{\lambda}{M \sin \theta_2'} = \frac{\lambda}{\sin \theta_2} \geq \frac{\lambda}{\sin \alpha}, \tag{2.51}$$

where M denotes the magnification factor and equals v/u, and α stands for the maximum angle transmitted by the objective lens. By assuming the object to be an infinite grating, the minimum spacing $\lambda / \sin \alpha$ can be achieved, which represents the resolution limit of the current imaging system.

2.4.2 Spatial resolution

Abbe diffraction limit

Abbe introduced the concept of numerical aperture (NA) to describe the spatial resolution of diffraction-limited imaging systems. By Snell's law, when a light wave of wavelength λ in air propagates in a medium of refractive index n, its wavelength will be λ/n. Under coherent illumination, in which the illumination beam is parallel to the optical axis, the period of the smallest features observable by a microscope is given by:

$$d_{\min} = \frac{\lambda}{n \sin \alpha} = \frac{\lambda}{\mathrm{NA}}, \tag{2.52}$$

which is also known as the *coherent resolution limit*. The resolution can be effectively

improved by adopting incoherent illumination. Specifically, by illuminating the sample with a cone of light of semi-angle α to the optical axis, the minimum period resolvable can be improved twice:

$$d_{\min} = \frac{\lambda}{2\mathrm{NA}}. \tag{2.53}$$

This resolution is also known as the *Abbe's diffraction limit*, which represents the ultimate resolution that can be achieved by conventional microscopy.

Rayleigh criterion

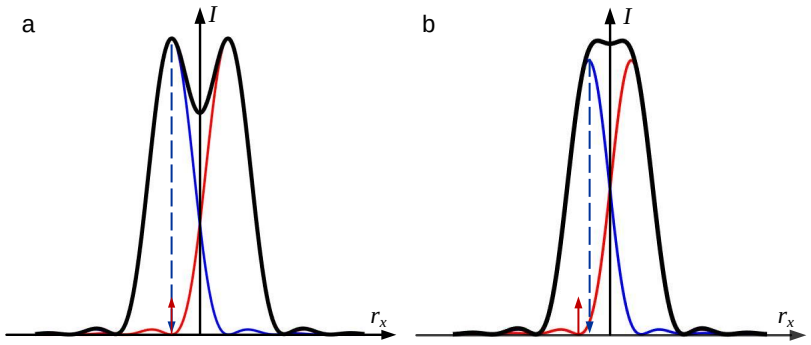

Figure 2.15: Spatial resolution criteria. (a) The Rayleigh criterion: two points are considered to be distinguishable if the central maximum of the Airy pattern of one point lies outside the first minimum of the other one. (b) The Sparrow criterion: two points are considered to be distinguishable if their resultant profile has a minimum between their centers.

Based on Airy's theory, Rayleigh refined the Abbe diffraction limit by quantifying the measure of the necessary separation between two Airy patterns [Figure 2.15(a)]. With the Rayleigh criterion, the corresponding angular separation limit can be calculated based on Equation 2.25:

$$I(\alpha) \propto \{J_1[(k_0 \sin\alpha)d]\}^2 = 0, \quad \alpha_{min} = 1.22\frac{\lambda}{d}. \tag{2.54}$$

Sparrow criterion

The Rayleigh resolution criterion may fail when the diffraction pattern has no well-defined zeros. In 1916, Sparrow proposed a criterion to overcome this limitation [70] [Figure 2.15(b)]. Mathematically, the angular separation limit given by the Sparrow criterion can

be expressed by:

$$\frac{\mathrm{d}^2 I(\alpha)}{\mathrm{d}\alpha^2} = 0, \quad \alpha_{min} = 0.95\frac{\lambda}{d}. \tag{2.55}$$

The Sparrow resolution limit is approximately 2/3 of the Rayleigh resolution limit, and it's closer to the theoretical resolution limit given by diffraction, i.e., the Abbe limit.

2.4.3 Fourier analysis in microscopy

The work of Abbe and Rayleigh laid the foundations for applying the Fourier analysis in microscopy [55]. In 1946, Duffieux published a book on the use of the Fourier methods in optics [71]. Now, frequency analysis has become a fundamental tool in microscopy, which can be utilized not only to characterize but also to improve the performance of imaging, in the aspects of both resolution and contrast.

Point spread function

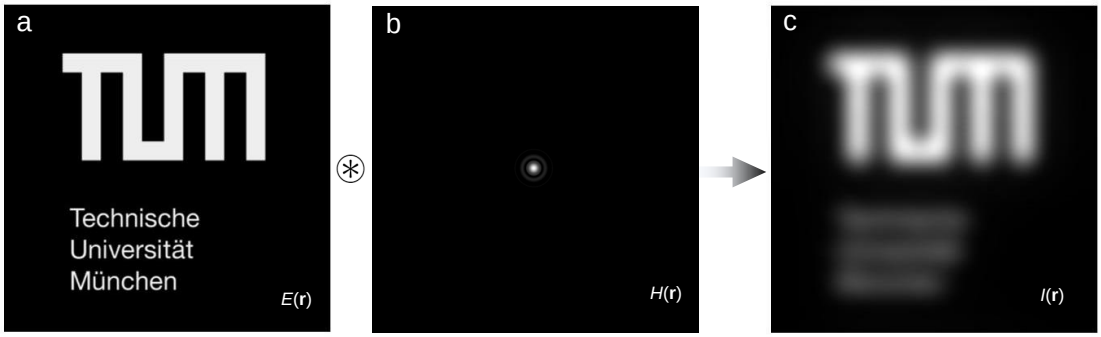

Figure 2.16: Simulated convolutional image formation in microscopy. (a) The original object, (b) the PSF of the simulated optical imaging system, and (c) the microscopic image simulated by convolution.

Airy's work illustrates that the image of a single point in a distant object corresponds to the Fraunhofer diffraction by the aperture function of the optical imaging system. Such a diffraction pattern in 3D is referred to as the point spread function (PSF). PSF describes the response of an imaging system to a point light source or a point object, and the Airy disk represents the PSF of a perfect optical imaging system. An extended object can be considered as a collection of such points which produce PSFs on the imaging plane individually. Thus, the final observed image of the object, $I(\mathbf{r})$, represents the sum of the intensity of the individual PSFs, which exactly corresponds to the convention of the

object emission, $E(\mathbf{r})$, and the PSF, $H(\mathbf{r})$, of the imaging system (Figure 2.16):

$$I(\mathbf{r}) = E(\mathbf{r}) \circledast H(\mathbf{r}). \tag{2.56}$$

The PSF can be obtained either by theoretical simulations, such as utilizing a mathematical model of diffraction or by experimental methods, such as acquiring 3D images of a fluorescent bead or a quantum dot. The 3D PSF of a perfect imaging system is supposed to be axial symmetric about the x-y plane and radial symmetric about the z-axis. The deviations of the PSF usually indicate aberrations, which may be caused by irregularities or misalignments of the components, especially the objective lenses, in the optical train.

Optical transfer function

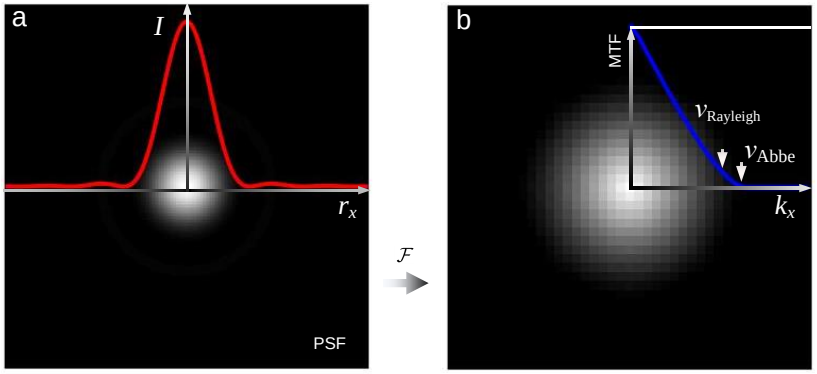

Figure 2.17: (a) PSF and (b) MTF of an ideal diffraction-limited optical imaging system. ν_{Rayleigh}, the frequency of the Rayleigh resolution limit. ν_{Abbe}, the frequency of the Abbe resolution limit.

The optical transfer function (OTF) is invented to quantify the ability of a microscope to transfer contrast from an object to its image at specific frequencies (Figure 2.17). Mathematically, the OTF is defined by the Fourier transform of the PSF:

$$\text{OTF}(\mathbf{k}) = \tilde{H}(\mathbf{k}) = \text{MTF}(\mathbf{k}) e^{i\,\text{PhTF}(\mathbf{k})}, \tag{2.57}$$

where MTF represents the modulation transfer function, and PhTF denotes the phase transfer function. The OTF incorporates the resolution and the contrast data into a single specification, allowing for evaluating both the two parameters simultaneously in a quantitative manner. It's especially useful for evaluating systems with the same resolving power but different aberrations, which may provide different image contrast at certain frequencies and therefore present different image quality.

Deconvolution

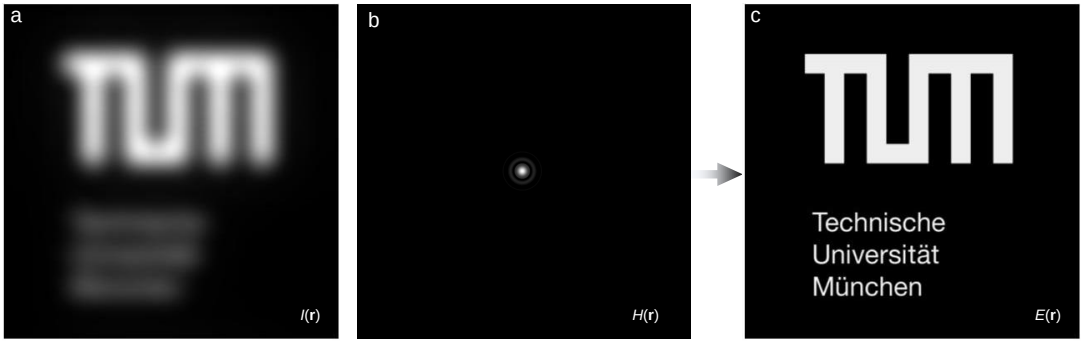

Figure 2.18: Principle of deconvolution microscopy. Simulated microscopic images (a) before and (c) after deconvolution. (b) The PSF of the simulated optical system.

In microscopy, noise and blurring are two sources that arise image degradation. Noise is usually caused by the random fluctuations of the photon number detected at a point. Blurring occurs usually due to the diffraction-limited imaging system itself, out-of-focus light, or measurement imperfections. Deconvolution is an image processing technique, which can mitigate the distortion caused by the microscope, thereby removing the blur from the original microscopic images and achieving the maximal resolution obtainable by the imaging system [72, 73]. Deconvolution can be performed by utilizing the convolution theorem. After obtaining the Fourier transform of the observed image $\tilde{I}(\mathbf{r})$ and the MTF of the imaging system, the object emission $E(\mathbf{r})$ can be recovered by applying a division operation in the frequency domain and an inverse Fourier transform (Figure 2.18):

$$E(\mathbf{r}) = \mathcal{F}^{-1}[\tilde{I}(\mathbf{k}) / \operatorname{MTF}(\mathbf{k})]. \tag{2.58}$$

As an image processing technique, no lost signals can be restored by deconvolution.

Chapter 3

In-plane and out-of-plane dual-sensitive speckle interferometer

This chapter presents a dual-sensitive image-shearing speckle interferometer [74], which is capable of measuring in-plane and out-of-plane strain components simultaneously in a single shot. This system is achieved by combining integrating off-axis interferometry, common-path image shearing, and symmetric observation. A spatial multiplexing technique is employed for the simultaneous phase retrieval of multiple components. Two customized slit filters and a common-path images-shearing module are adopted to improve the performance of phase imaging. Mode-I fracture experiments of three-point bending are conducted to validate the feasibility and the capability of the proposed method.

3.1 Introduction

Interferometric methods allow full-field, non-invasive optical measurements of shapes [75–79], displacements [9, 80, 81], strains [10, 82], and curvatures [83] of both specularly or diffusely reflecting surfaces. Deformations in nature and engineering are usually in 3D, requiring methods capable of measuring multiple components simultaneously. Speckle interferometry achieves simultaneous multi-component measurements by integrating interferometers and adopting multiplexing techniques [84–86]. Such a multi-component measurement system can be both single-sensitive and multi-sensitive. Speckle interferometers designed for simultaneous measurements of out-of-plane displacements and the associated different order derivatives, such as displacement and slope [84, 87], or slope and curvature [88, 89], utilize sensitivity vectors in one dimension only and therefore can be referred to as single-sensitive techniques. Multi-sensitive systems usually provide both

in-plane and out-of-plane sensitivity vectors [86, 90–94], or even 3D sensitivity vectors [86, 95].

The main challenges in achieving multi-sensitive measurements include building in-plane sensitivity vectors. Conventional in-plane-sensitive speckle interferometry operates by using two sensitivity vectors. Therefore, symmetric dual-beam systems are commonly adopted for measuring in-plane displacements or in-plane strains [9, 96, 97]. The symmetric dual-beam systems with both in-plane and out-of-plane sensitivities have also been demonstrated in a stepwise fashion [91, 98]. However, single-shot multi-sensitive analysis is still challenging, especially when the in-plane strain components are involved. To achieve dynamic multi-sensitive measurements of displacements, several attempts have been made by utilizing spatial-carrier phase shifting [97], different wavelengths [99], polarization [96], different coherence lengths [100], and spatial multiplexing [92]. For the multi-sensitive measurements of strain components, methods achieved by two-step recording and temporal phase shifting have been reported [90, 93, 94, 98, 101], permitting the static analysis only.

In this chapter, a dual-sensitive image-shearing speckle interferometer is developed for single-shot simultaneous in-plane and out-of-plane strain measurements. An interferometric configuration with two symmetric observation beams and one illumination beam is built to obtain the dual strain sensitivity. A spatial multiplexing method is applied to record synchronous interferograms with the same spatial-carrier frequency but different sensitivities and to reconstruct the multiple phase components simultaneously. Two customized slit spatial filters and a common-path image-shearing module are employed to improve the phase imaging quality. To verify the feasibility and the capability of the developed method, simultaneous measurements of in-plane and out-of-plane strain components are carried out in Mode-I fracture experiments of three-point bending.

3.2 Results

3.2.1 Principle of in-plane and out-of-plane dual-sensitive interferometry

The schematic of the dual-sensitive imaging-shearing speckle interferometer is presented in Figure 3.1(a). The sample is illuminated by a collimated laser beam normal to the sample surface and observed from two symmetric directions of the same angle θ. Assuming the observation direction lies in the plane y=0, the wave vectors of the illuminating beam $\vec{k}_1$

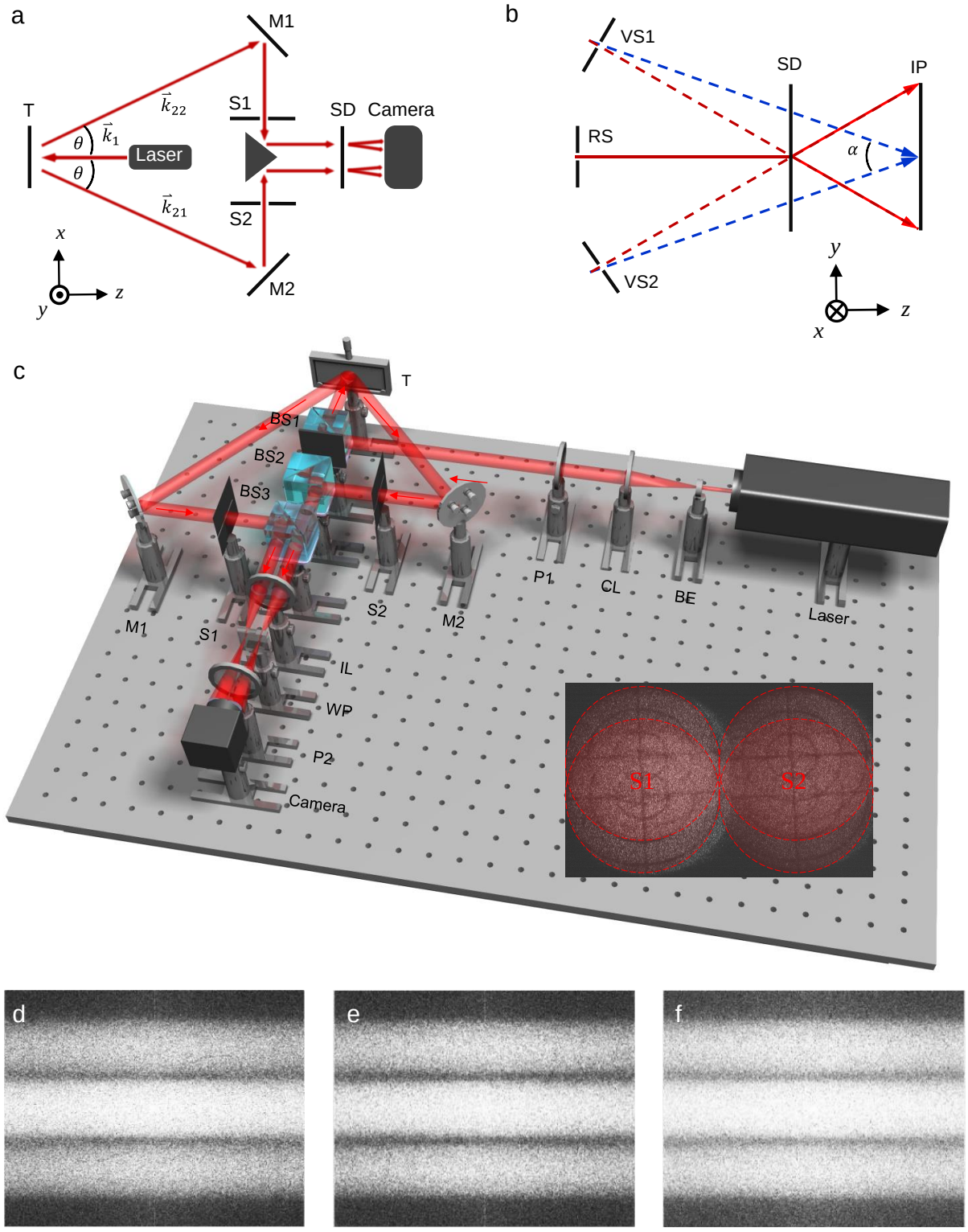

Figure 3.1: See next page for caption.

Figure 3.1: Principle and implementation of dual-sensitive speckle interferometry. (a) The symmetric dual-chancel interferometric configuration. M1 and M2: mirrors; S1 and S2: slits; SD: shearing device. (b) The spatial carrier frequency generated by the common-path image-shearing device. VS1 and VS2: virtual slits; RS: real slit. (c) The experimental setup and the obtained interferograms. BE: beam expander; CL: collimating lens; P1 and P2: polarizers; T: target; BS1, BS2, and BS3: beam splitters. IL: imaging lens; WP: Wollaston prism. (d) and (e), The spectra of the interferograms acquired by the left channel (S1) and the right channel (S2), respectively. (f) The resultant spectrum.

and two observation beams $\vec{k}_{21}$, $\vec{k}_{22}$ can be expressed as:

$$\begin{aligned}\vec{k}_1 &= \frac{2\pi}{\lambda}(-\vec{w}_0)\\ \vec{k}_{21} &= \frac{2\pi}{\lambda}(-\sin\theta\cdot\vec{u}_0+\cos\theta\cdot\vec{w}_0)\\ \vec{k}_{22} &= \frac{2\pi}{\lambda}(\sin\theta\cdot\vec{u}_0+\cos\theta\cdot\vec{w}_0),\end{aligned} \tag{3.1}$$

where $\vec{u}_0$, $\vec{v}_0$, and $\vec{w}_0$ are the unit vectors along the positive x-, y-, and z-axes, respectively. Before reaching the camera, the two object beams are reflected by mirrors symmetrically and split into two separate and parallel paths. Then the beams pass through a common-path shearing device, which introduces a variable shear in the y-direction. During a deformation process, the phase changes corresponding to the left observation direction $\vec{k}_{21}$ and right observation direction $\vec{k}_{22}$ are different. The phase change of the left vertical images-shearing interferogram $\triangle\varphi_l$ can be expressed as [86, 98]:

$$\begin{aligned}\triangle\varphi_l &= \vec{k}_l(\vec{u},\vec{v},\vec{w})\cdot\vec{l}(x,y)\\ &= [(\vec{k}_1-\vec{k}_{21})|_{(x,y)}-(\vec{k}_1-\vec{k}_{21})|_{(x,y+\delta y)}]\cdot\vec{l}(x,y)\\ &= \frac{2\pi}{\lambda}\left[-\sin\theta\cdot\frac{\partial l_x}{\partial y}+(1+\cos\theta)\frac{\partial l_z}{\partial y}\right]_{\delta y},\end{aligned} \tag{3.2}$$

where $\vec{k}_l$ is the sensitivity vector corresponding to the left observation beam $\vec{k}_{21}$ and the illuminating beam $\vec{k}_1$, $\vec{l}$ represents the vector of surface displacements, and δy is the shearing amount.

Similarly, the phase change of the right vertical interferogram $\triangle\varphi_r$ can be expressed as:

$$\begin{aligned}\triangle\varphi_r &= \vec{k}_r(\vec{u},\vec{v},\vec{w})\cdot\vec{l}(x,y)\\ &= [(\vec{k}_1-\vec{k}_{22})|_{(x,y)}-(\vec{k}_1-\vec{k}_{22})|_{(x,y+\delta y)}]\cdot\vec{l}(x,y)\\ &= \frac{2\pi}{\lambda}\left[\sin\theta\cdot\frac{\partial l_x}{\partial y}+(1+\cos\theta)\frac{\partial l_z}{\partial y}\right]_{\delta y},\end{aligned} \tag{3.3}$$

where $\vec{k}_r$ is the sensitivity vector given by the right observation direction $\vec{k}_{22}$ and the illuminating beam $\vec{k}_1$.

$\triangle\varphi_l$ and $\triangle\varphi_r$ are both in-plane and out-of-plane sensitive. The pure out-of-plane strain component $\partial l_z/\partial y$ can be determined by adding $\triangle\varphi_l$ and $\triangle\varphi_r$:

$$\triangle\varphi_l + \triangle\varphi_r = \frac{4\pi}{\lambda}\left[(1+\cos\theta)\frac{\partial l_z}{\partial y}\right]_{\delta y}. \tag{3.4}$$

Furthermore, the pure x-direction in-plane strain component $\partial l_x/\partial y$ can be determined by subtracting $\triangle\varphi_l$ and $\triangle\varphi_r$:

$$\triangle\varphi_l - \triangle\varphi_r = -\frac{4\pi}{\lambda}\left[(\sin\theta)\frac{\partial l_x}{\partial y}\right]_{\delta y}. \tag{3.5}$$

In this system, the shearing direction can be adjusted to obtain other derivatives of displacements, such as $\partial l_x/\partial x$.

3.2.2 Spatial multiplexing

The multiple phase components can be extracted simultaneously by using spatial multiplexing [92]. In each channel, the two split object beams reach the detector with the same angle [Figure 3.1(b)]. The complex fields of the associated wavefronts can be expressed as the following:

$$\begin{aligned}\mathbf{U}_{11}(x,y) &= U_{11}(x,y)e^{i\left[\varphi(x,y)+\vec{k}_{11}\cdot\vec{r}\right]}\\ \mathbf{U}_{12}(x,y+\delta y) &= U_{12}(x,y+\delta y)e^{i\left[\varphi(x,y+\delta y)+\vec{k}_{12}\cdot\vec{r}\right]},\end{aligned} \tag{3.6}$$

where $U_{11}(x,y)$ and $U_{12}(x,y+\delta y)$ represent the amplitudes of complex fields, and $\vec{k}_{11}$ and $\vec{k}_{11}$ denote the wavevectors. The intensity of the left interferogram $I_l(x,y)$ is therefore given by [46]:

$$\begin{aligned}I_l(x,y) &= [U_{11}(x,y)+U_{12}(x,y+\delta y)]\cdot[U_{11}(x,y)+U_{12}(x,y+\delta y)]^*\\ &= U_{11}(x,y)\cdot U_{11}^*(x,y)+U_{12}(x,y+\delta y)\cdot U_{12}^*(x,y+\delta y)\\ &+ U_{11}(x,y)\cdot U_{12}^*(x,y+\delta y)+U_{12}(x,y+\delta y)\cdot U_{11}^*(x,y),\end{aligned} \tag{3.7}$$

where U_{11}^* denotes the complex conjugate of U_{11}. By using FFT, the intensity image can be transformed from the space domain into the frequency domain:

$$\widetilde{I}_l(k_x,k_y) = \widetilde{D}_l(k_x,k_y)+\widetilde{C}_l(k_x-\nu_x,k_y-\nu_y)+\widetilde{C}_l^*(k_x+\nu_x,k_y+\nu_y), \tag{3.8}$$

where $\widetilde{D}_l$ represents the direct-current component of the image. k_x and k_y represent the coordinates in the frequency domain. ν_x and ν_x represent the carrier frequencies. The conjugate terms $\widetilde{C}_l$ and $\widetilde{C}_l^*$ contain the phase information of the interferograms. The inverse Fourier transform can be applied to one of the conjugate terms to reconstruct the phase distribution from the interferogram. The phase change caused by the object deformation is therefore given by:

$$\triangle\varphi_l(x,y) = \triangle \arg\{\mathcal{F}^{-1}[\tilde{C}_l(k_x,k_y)]\}. \tag{3.9}$$

The left and the right interferograms, which are characterized by different sensitivity vectors but the same carrier frequency, are recorded synchronously by the same camera. The phase change of the right interferogram $\triangle\varphi_r$ is given by:

$$\triangle\varphi_r(x,y) = \triangle \arg\{\mathcal{F}^{-1}[\tilde{C}_r(k_x,k_y)]\}. \tag{3.10}$$

3.2.3 Experimental setup

Figure 3.1(c) illustrates the experimental setup and the obtained interferograms of the dual-sensitive image-shearing interferometric system. A He-Ne laser (HNLS008L-EC, Thorlabs) with a wavelength of 632.8 nm and a power of 0.8 mW was used as the light source. The laser beam was expanded and collimated by two lenses with focal lengths of -6 mm and 100 mm, respectively. BS1 was used to ensure that the illuminating beam was perpendicular to the object surface. M1/M2 and BS2/BS3 were used to ensure that the two observation beams were parallel to each other and perpendicular to the camera. WP was employed as a polarized shearing device. P1 and P2 were used to match the polarization states of the split object beams and to generate high contrast interference fringe patterns in the interferogram. The shearing amount could be adjusted by changing the distance between the image plane and the shearing device. A complementary metal-oxide semiconductor (CMOS) camera (DCC1545M, Thorlabs) was used as the detector, and the two slits were used as spatial filters. The spectra corresponding to the left, the right, and the resulting interferogram are shown in Figures 3.1 (d)-(f), respectively. These spectra were adjusted to be identical. The 2D space shift between the left and the right interferograms on the imaging plane was calibrated to ensure pixel-level image matching.

3.2.4 Demonstration in mode-I fracture experiments

Mode-I fracture experiments of three-point bending were conducted for experimental demonstrations. The mechanical loading device is shown in Figure 3.2. To achieve the small-scale yielding, a polymethyl methacrylate (PMMA) specimen was prepared, due

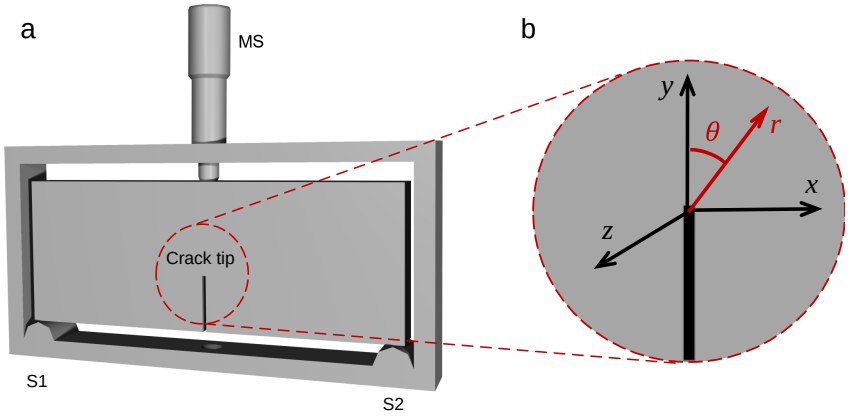

Figure 3.2: (a) The loading device and the PMMA specimen (105×40×10 mm^3) used for the three-point bending fracture experiments. MS: micrometer screw. S1/S2: supports of three-point bending. (b) The crack-tip area.

to its isotropic mechanical property and relatively high yield strength. The specimen (105×40×10 mm^3) with a notch (1×15×10 mm^3) was coated with white spray paint to increase the reflectivity. A micrometer screw was used for loading. A vertical force was loaded in the center of the specimen to achieve standard three-point bending.

The in-plane and out-of-plane strain fields on the crack-tip area were measured simultaneously. By using the spatial multiplexing method, the wrapped 2π-modulo phase maps corresponding to the interferograms in Figure 3.1(c) were obtained, as shown in Figures 3.3(a) and (b). Both the two phase images contain in-plane and out-of-plane strains simultaneously as described in Equations 3.9 and 3.10. In this measurement, a vertical shear amount parallel to the notch direction was applied. The points 1 and 2 in Figure 3.3(a) present the positions of two sheared crack tips of the object waves $\mathbf{U}_{11}$ and $\mathbf{U}_{12}$. The corresponding in-plane and out-of-plane strain fields of the sample surface [Figures 3.3(c) and (d)] were reconstructed by adding and subtracting the initial phase images based on Equations 3.4 and 3.5. The calibration of the position difference between the left and the right interferogram on the imaging plane ensured pixel-level image matching between the initial phase maps. Figure 3.3(c) shows a full-field phase distribution of the out-of-plane strain component $\partial l_z/\partial y$ obtained by adding the complementary phase maps shown in Figures 3.3(a) and (b). As the shearing amount δy corresponds to a real physical size of approximately 4 mm, each 2π variation in the phase images corresponds to a strain difference of 46 $\mu\varepsilon$ given by Equation 3.4. Figure 3.3(d) shows the in-plane strain component $\partial l_x/\partial y$ obtained through the subtraction of the initial phase images, and each 2π phase variation corresponds to a strain difference of 112 $\mu\varepsilon$.

To verify the experimental results, the simulation of 3D strain distributions on the crack

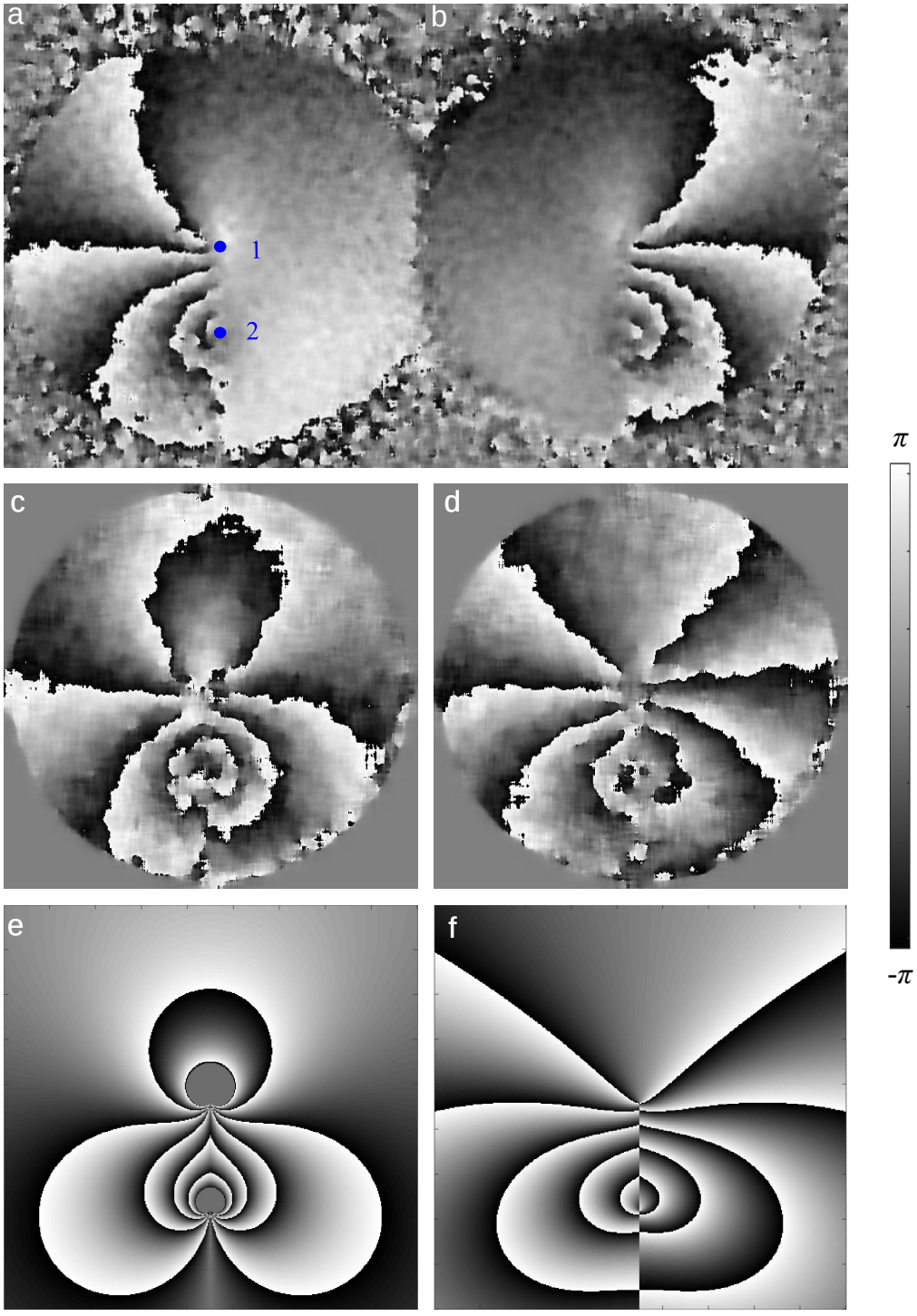

Figure 3.3: Experimental results. The initial phase images obtained from (a) the left and (b) right channels. The reconstructed phase images of (c) the out-of-plane crack-tip strain component $\partial l_z/\partial y$ and (d) the in-plane crack-tip strain component $\partial l_x/\partial y$. The corresponding analytical solutions of (e) $\partial l_z/\partial y$ and (f) $\partial l_x/\partial y$ obtained by linear elastic fracture mechanics.

tip area of three-point bending mode-I fracture was conducted by using the theory of linear elastic fracture mechanics [Figures 3.3(e) and 5(f)]. The coordinate system of the simulation is shown in Figure 3.2(b). Mathematically, the corresponding displacement fields U, V, and W can be expressed as [93, 94, 102]:

$$\begin{aligned} U &= \frac{(1+\nu)K_1}{2E}\sqrt{\frac{r}{2\pi}}\left[(2k+1)\sin\frac{\theta}{2} - \sin\frac{3\theta}{2}\right] \\ V &= \frac{(1+\nu)K_1}{2E}\sqrt{\frac{r}{2\pi}}\left[(2k-1)\cos\frac{\theta}{2} - \cos\frac{3\theta}{2}\right] \\ W &= \frac{-\nu h K_1}{E}\sqrt{\frac{1}{2\pi r}}\cos\frac{\theta}{2}, \end{aligned} \tag{3.11}$$

where ν is Poisson's ratio, E is Young's modulus, k equals $(3-\nu)/(1+\nu)$, h is the thickness of the specimen, and K_1 is the stress intensity factor corresponding to the pure mode-I fracture of three-point bending [102]. The value of K_1 was assumed to be 1 in the simulation, as it is a constant term under a given load and therefore unrelated to the general shape, the orientation, and the symmetry properties of the simulated strain fields. The pixel shearing amount was obtained from the distance between the sheared crack tips contained in the two object beams $\mathbf{U}_{11}$ and $\mathbf{U}_{12}$. Taking this pixel shearing amount as the interval of the gradient, the simulated out-of-plane and in-plane crack-tip strain components $\partial l_z/\partial y$ and $\partial l_x/\partial y$ were obtained from the displacement fields W and U, respectively, as shown in Figures 3.3(e) and 5(f). Due to the singularity of the crack-tip deformation, for comparison, the singular strain values in the simulated field $\partial l_z/\partial y$ have been eliminated as shown in Figure 3.3(e). The figure shows that the theoretical out-of-plane strain field $\partial l_z/\partial y$ is symmetric about the y-axis, and the in-plane strain field $\partial l_x/\partial y$ is antisymmetric about the y-axis. Hence, considering the existence of stress singularity on the crack-tip area and the non-uniformity of the material, the general shape, the orientation, and especially the symmetry properties of the measured surface strain fields using the proposed method agree with the theoretical results.

3.3 Discussion

A dual-sensitive image-shearing speckle interferometer is developed for single-shot simultaneous in-plane and out-of-plane strain measurements. The method is achieved by combining integrating off-axis interferometry, common-path image shearing, and symmetric observation. A spatial multiplexing technique was adopted for the single-shot phase retrieval of multiple components. Two customized slit spatial filters and a common-path image-shearing module were employed to improve the phase imaging quality. For a demonstration, single-shot measurements of multiple strain components were conducted

in mode-I fracture experiments of three-point bending. The experimental results agreed with the theoretical simulations. The proposed method potentially allows industrial applications such as dynamic in-plane and out-of-plane dual-sensitive NDT measurements.

To measure the deformations of high strain gradients in the crack-tip area, two improvements were made in the proposed system to improve the imaging quality. Firstly, we employed two customized slits for spatial filtering. Temporal phase shifting can be achieved through phase-stepping procedures, and therefore it's limited to static or quasi-static measurements. To achieve single-shot phase imaging, carrier phase-shifting methods use apertures [84, 85, 97] as spatial filters to generate the cutoff frequency. However, the apertures also impose limitations on the light efficiency and the maximum spatial frequency of the system, which can degrade the imaging quality. On contrast, slits pass more incident light, thus allowing better imaging performance. Secondly, the image-shearing module was built with a Wollaston prism. This compact and robust common-path interferometric configuration permits higher temporal phase stability as compared with conventional image-shearing solutions such as a Michelson or a Mach-Zehnder interferometer.

Another concern lies in the synchronous acquisition of interferograms with the two channels. To achieve single-shot multiple strain component measurements, another strategy is to build different carrier frequencies in the left and the right interferometric channels and spatially overlap the two interferograms on the imaging plane. Thus, the phase distribution corresponding to the two different sensitivity vectors can be separated in the frequency domain after applying a Fourier transform and then totally reconstructed using the carried phase-shifting algorithm. However, achieving such a scheme requires additional procedures to avoid the cross interference between the two symmetric channels.

Chapter 4

Speckle interferometer with an unlimited minimal shear amount

This chapter develops a single-aperture common-path speckle interferometer with an unlimited minimal shear amount [103]. This unlimited shear amount is introduced when a Wollaston prism is placed near the Fourier plane of a common-path interferometer, which is built by using a quasi-4f imaging system. The fundamentals of the shear amount and the spatial carrier frequency generation are analyzed mathematically, and the theoretical predictions are validated by a static experiment. Mode-I fracture experiments through the three-point bending are conducted to prove the feasibility and the capability of this method in full-field strain measurement with various shear amounts. A remarkable feature of this setup is that no tilt is required between the optical components to produce the unlimited shear amount in off-axis holography.

4.1 Introduction

The single-aperture common-path speckle interferometer combines the benefits of common-path geometry and off-axis holography [74, 104], as a result, it provides instant phase change maps with subwavelength level accuracy. In this system, the common-path configuration is used to improve temporal stability in a variety of surroundings [53, 105, 106]. The aperture is used to generate the carrier frequency and the cut-off frequency for dynamic measurements [46, 84, 85, 97]. Hence, the acquisition time of this method is only limited by the recording device.

The image-shearing interferogram obtained with the common-path speckle interferometer offers full-field displacement gradient sensitivity, in which the directional derivatives

of the displacement on the deformed surface can be obtained. The shear amount is an important parameter to control the measurement performance. In some cases, the shear amounts need to be small enough to obtain the required displacement gradient information, especially when the physical size of the entire field of view is relatively large. For example, a small shear amount is required in NDT to ensure that the internal defects are reflected in the surface strain by singularity areas [10, 107]. Additionally, the excess shear amount may deteriorate the spatial resolution and shearography approximation, and may cause an immeasurable zone in the target with geometrical discontinuity [107, 108]. However, the minimal shear amount in a conventional single-aperture common-path speckle interferometer is limited by the single-lens system.

In this chapter, we developed a quasi-4f common-path optical imaging system to generate an unlimited shear amount in the image-shearing interferograms, which has the potential to increase the spatial resolution for crack detection. This robust and simple imaging setup operates without the need to tilt any optical components, which prevents alignment procedures and achieves a highly stable and compact system.

4.2 Results

4.2.1 Limitation of the conventional setup

The limited minimal shear amount in the conventional single-aperture common-path speckle interferometer is shown in Figure 4.1(a). This interferometer is arranged by placing WP between L and IP, and A in front of L [104]. As a result, the minimal shear amount δ_{min} is limited by:

$$\delta_{min} = 2d_{min} \cdot \tan(0.5\beta), \tag{4.1}$$

and the distance d_{min} becomes zero only when the beam splitting plane is on the surface of the image sensor, which is impractical due to the size of the beam splitter and the existence of the polarizer or the other optical components between WP and IP.

4.2.2 Principle of shear-unlimited speckle interferometry

A quasi-4f imaging system is introduced to produce the unlimited shear amount [Figures 4.1(b) and (c)]. The developed interferometer is arranged by placing WP between L_1 and L_2, near FP, P between L_2 and IP, and A in front of L_1. WP is employed as a shearing device, and P is used to adjust the polarization of the two split object beams to obtain interferograms with high-quality interference fringes. A is used to generate the cut-off frequency in the spectral domain. As shown in the magnified diagrams in Figures 4.1, δ

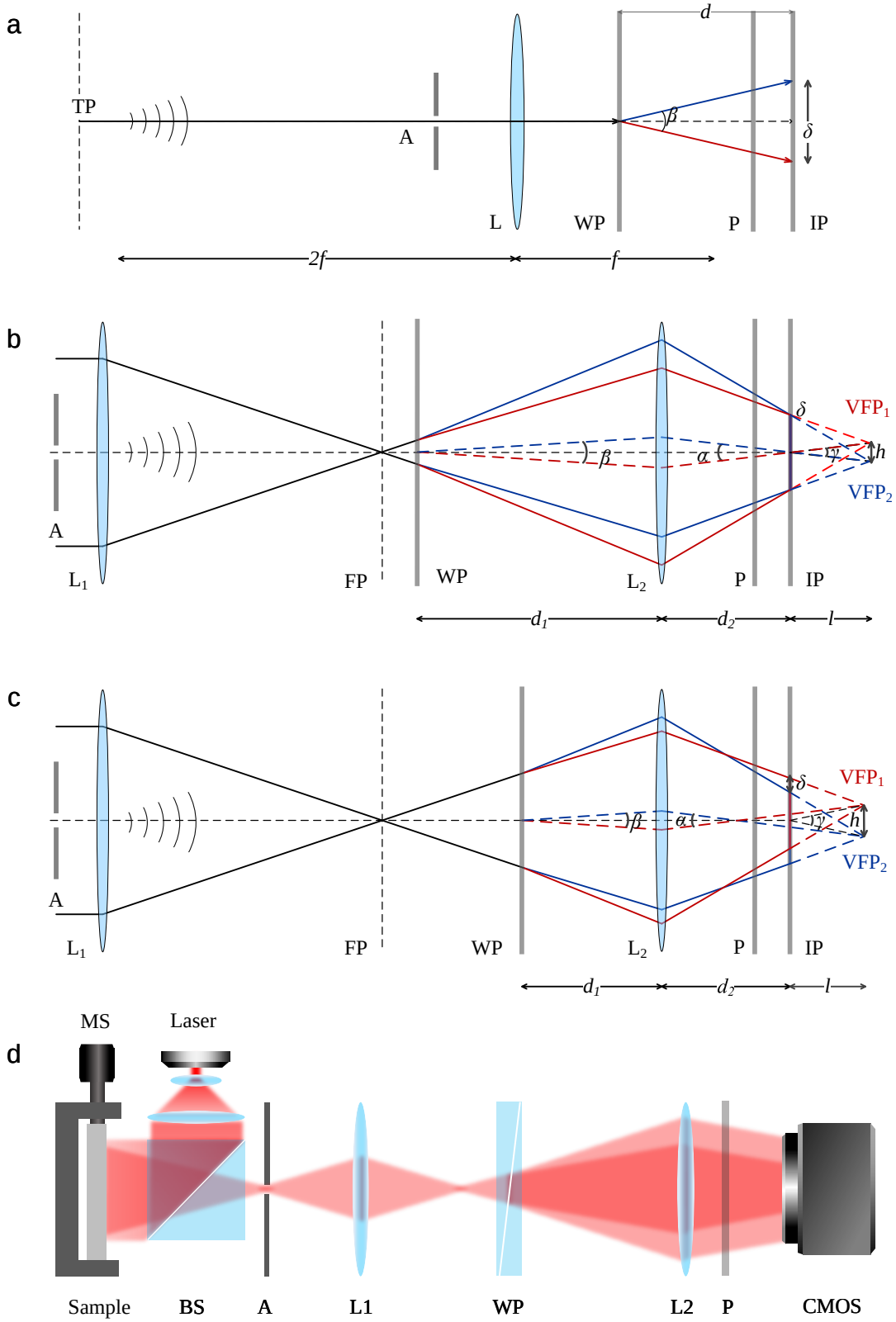

Figure 4.1: See next page for caption.

Figure 4.1: (a) The minimal shear amount limit in the conventional single-aperture common-path speckle interferometer. TP: target plane; A: aperture; L: imaging lens; WP: Wollaston prism; P: polarizer. f represents the focal length of L, β represents the beam separation angle of WP, d is the distance between WP and IP, and δ is the shear amount. (b) and (c) The optical arrangement of the shear-unlimited common-path speckle interferometer. L_1 the first lens; FP the Fourier plane of L_1; L_2 the second lens; $VFP_{1/2}$ virtual focal point 1/2. d_1 is the distance between WP and L_2, d_2 is the distance between L_2 and IP, l is the distance between IP and the virtual focal points, h is the distance between VFP_1 and VFP_2, α is the average incident beam separation angle, and γ is the angle between two incident beams projecting on the same point of IP. (b) and (c) show the schematic diagrams of the light path when δ equals and is more than zero respectively. (d) Schematic of the experimental setup. BS: beam splitter.

can be adjusted by changing the position of WP:

$$\delta = 2d_2 \cdot \tan(0.5\alpha) - 2d_1 \cdot \tan(0.5\beta). \tag{4.2}$$

The carrier frequency ν_0 is determined by γ, which is related to l, h, and the laser wavelength λ:

$$\nu_0 = \frac{2\sin(0.5\gamma)}{\lambda} = \frac{2\sin(\arctan\frac{0.5h}{l})}{\lambda}. \tag{4.3}$$

According to Figure 4.1(c), h is given by:

$$h = \delta + 2l \cdot \tan(0.5\alpha). \tag{4.4}$$

Assuming that l is fixed, the carrier frequency ν_0 and the distance h are positively correlated. In the case when the shear amount δ is zero [Figure 4.1(b)], the distance h, which represents the carrier frequency, equals:

$$h\big|_{\delta=0} = 2l \cdot \frac{d_1}{d_2} \cdot \tan(0.5\beta). \tag{4.5}$$

In the case when δ increases [Figure 4.1(c)], the angle α decreases slightly as the refraction angle decreases from the edge to the center of L_2. However, the reduction of α is relatively small and it can be ignored. Hence, the carrier frequency ν_0 increases when the shear amount increases from zero. The carrier frequency is at a minimum when the shear amount δ is zero:

$$\nu_0\big|_{\delta=0} = \frac{2\sin\{\arctan[\frac{d_1}{d_2} \cdot \tan(0.5\beta)]\}}{\lambda}. \tag{4.6}$$

It is known that the carrier frequency should be large enough so that the spatial phase shifting can be carried out for the phase reconstruction, which is important for the optical design of the off-axis holography. In the shear-unlimited speckle interferometer, Equation 4.6 shows that the minimal carrier frequency can be increased to be large enough by employing a beam splitter with a larger beam separation angle or by increasing d_1/d_2, while no tilt between the optical components is required.

If the aperture in the input plane is illuminated using a uniform object beam, an interferogram with carrier frequency ν_0 and shear amount δ can be obtained in the imaging plane. The phase map φ of the measured object can be derived through Fourier transform [46]:

$$\begin{aligned} \mathbf{C}(x,y) &= \mathcal{F}^{-1}\{\mathcal{F}[I(x,y)] \cdot \mathrm{F_o}\}, \\ \varphi(x,y) &= \arg[\mathbf{C}(x,y)], \end{aligned} \tag{4.7}$$

where $I(x,y)$ is the intensity distribution of the interferogram, $\mathrm{F_o}$ represents the low-pass filtering in either of the two spectra that contain the surface information, and $\mathbf{C}(x,y)$ is the complex amplitude of the filtered interferogram.

4.2.3 Experimental setup

The schematic of the experimental setup is shown in Figure 4.1(d). The sample was fixed by a micrometer screw device, which was also used to apply load to the sample. A He-Ne laser (λ=632.8 nm, HNLS008L-EC, Thorlabs) was used as the light source. The laser beam was expanded and collimated by the lenses, and reflected by BS to ensure the illumination beam is approximately perpendicular to the sample surface. The focal lengths of $\mathrm{L_1}$ and $\mathrm{L_2}$ are f_1=100 mm and f_2=30 mm, respectively. A WP with a beam separation angle $\beta = 1^\circ$ was used as the beam splitter, which can provide sample's birefringence information as compared to a diffraction grating or a Fresnel biprism. A CMOS camera of 1024 × 1280 pixels and 256 gray levels was employed to record the interferograms. A with a diameter of 1.5 mm was fixed in front of $\mathrm{L_1}$.

4.2.4 Demonstration in static measurements

The image-shearing interferograms of a static pattern were obtained to show the unlimited minimal shear obtained with the shear-unlimited common-path speckle interferometer. The shear amounts of these four interferograms were $\delta_x = \delta_y \approx 0$, 1.0, 1.5, and 2.0 mm, respectively [Figures 4.2(a)-(d)], and the corresponding d_1 were about 27, 20, 17, and 15 mm, respectively. The periodic fringe structures in the zoomed in interferograms represent the generated carrier frequencies [Figures 4.2(e)-(h)]. To quantify the carrier frequency, the interferograms were transformed into the Fourier domain [Figures 4.2(i)-

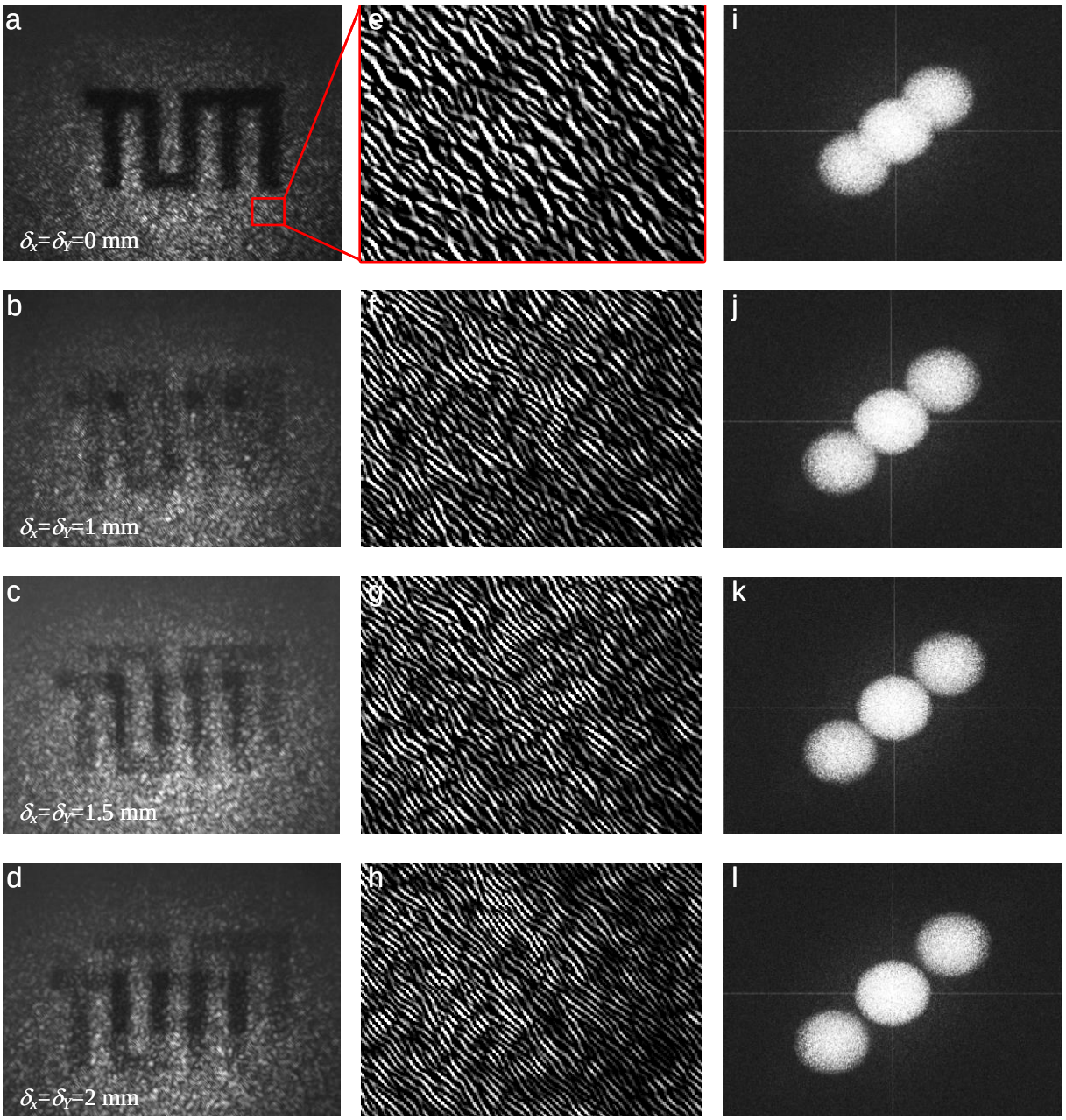

Figure 4.2: (a-d) The image-shearing interferograms of a static pattern with the shear amounts of $\delta_x = \delta_y$=0, 1, 1.5, and 2 mm, respectively. (e-h) The corresponding periodic fringes in the zoomed in interferograms. (i-l) The corresponding Fourier spectra obtained from the interferograms in (a-d).

(l)]. The separation distance between the sidelobes represents the value of the carrier frequency. Figure 4.2 shows that there is no limit for the minimal shear amount, and it can be zero, which provides the potential to increase the spatial resolution for crack detection. The carrier frequency is at the minimum when the shear amount δ is zero, which is large enough for phase reconstruction with the spatial phase-shifting method. The carrier frequency increases slightly when the shear amount increases from zero. The experimental results agree with the theoretical predictions (Equations 4.2-4.6).

4.2.5 Demonstration in mode-I fracture experiments

To validate the feasibility and the capability of this imaging setup in strain measurements, a mode-I fracture test through three-point bending was carried out [Figure 4.3]. A polymethyl methacrylate (PMMA) substrate was used as the model material under conditions of small-scale yielding. A specimen ($105 \times 40 \times 10$ mm^3) with a vertical notch ($1 \times 15 \times 10$ mm^3) in the lower middle was coated with white spray paint (100 μm) to increase its reflectivity. The obtained interferograms on the crack-tip area with the shear amounts of $\delta_x = \delta_y$= 0.5, 1, 2, and 3 mm are shown in Figures 4.3(a)-(d), respectively. Then, the PMMA sample was loaded by a symmetric three-point bending, which was carried out by applying a downward force on the upper middle of the sample, and two upward supporting forces on the lower left and the lower right symmetrically. The corresponding unwrapped phase change maps before and after loading, $\Delta\varphi(x,y)$, which stand for the out-of-plane strain fields [74], were calculated with Equation 4.7 [Figures 4.3(e)-(h)]. Figures 4.3(e)-(h) show that all the positions of the notch in the interferograms with different shear amounts can be located quantitatively from the singularity areas in the measured phase maps, even in the interferogram with the shear amount of $\delta_x = \delta_y$= 0.5 mm, in which the two virtual images of the notch partly overlap with each other. It should be noted that $\delta_x = \delta_y$= 0.5 mm is not the shear amount limit, it can be even smaller, but theoretically, the directional derivatives of the displacement will be zero and the singularity areas will disappear if the shear amount equals zero. To verify these results, the simulated out-of-plane strains with corresponding shear amounts on the crack tip of mode-I fracture under the three-point bending were obtained by the theory of linear elastic fracture mechanics [74, 102] [Figures 4.3(i)-(l)]. Figures 4.3(i)-(l) show the general shapes and the orientation of the measured strain fields with different shear amounts agree well with the corresponding theoretical results, which proves the accuracy of the developed method. In general, Figure 4.3 validates that the developed common-path speckle interferometer is capable of measuring full-field strain accurately with unlimited shear amounts.

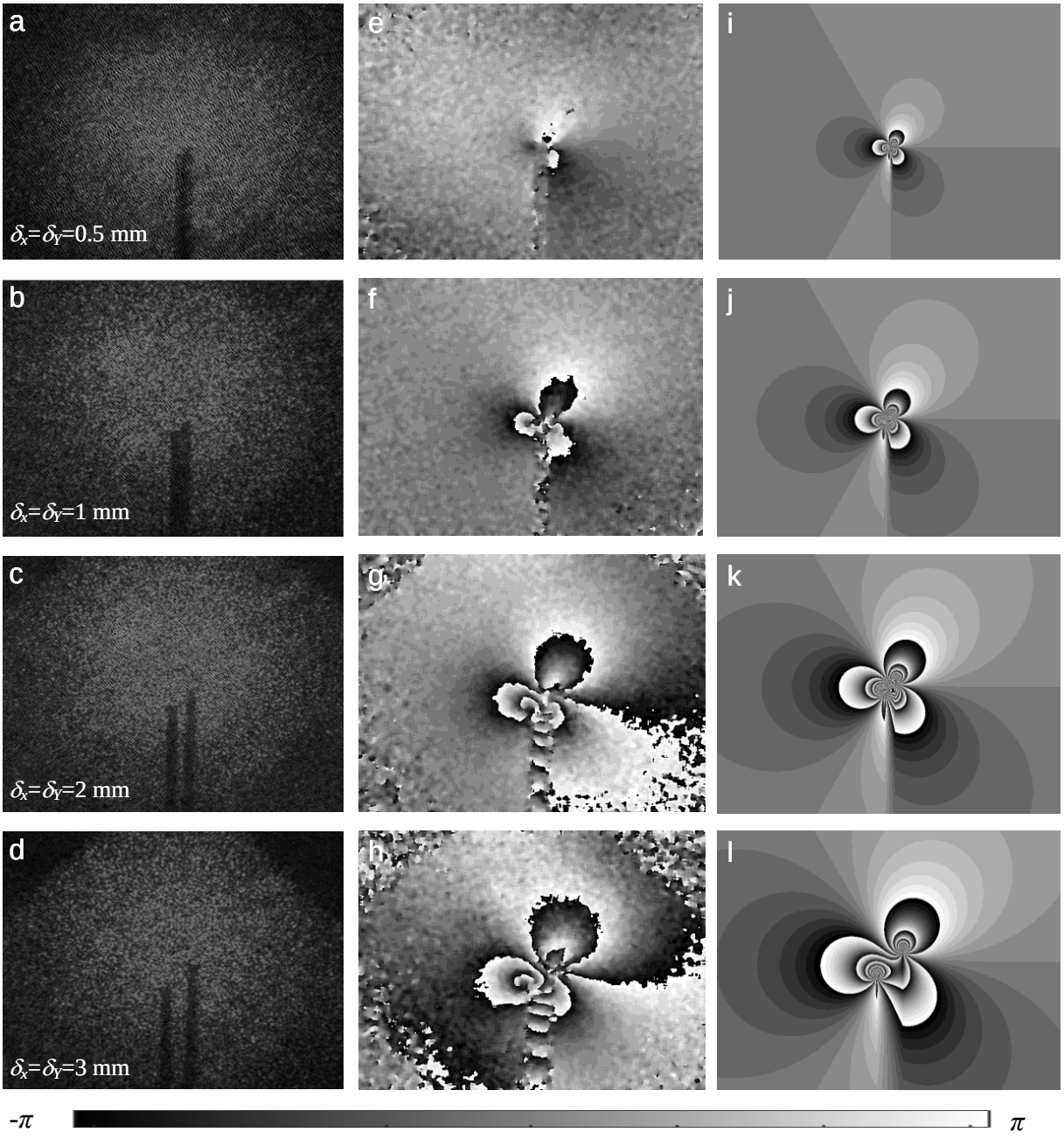

Figure 4.3: (a-d) The image-shearing interferograms on the crack-tip area with the shear amounts of $\delta_x = \delta_y$= 0.5, 1, 2, and 3 mm, respectively. (e-h) The corresponding phase change maps due to the mechanical load measured with the developed method. (i-l) The corresponding simulated phase change maps obtained by the theory of linear elastic fracture mechanics.

4.3 Conclusion

In conclusion, a shear-unlimited common-path speckle interferometer is developed, which provides full-field strain measurements with unlimited shear amounts, and the acquisition time is only limited by the recording device due to the off-axis holography feature. The fundamentals of the shear amount and the spatial carrier frequency generation are analyzed mathematically, and the theoretical predictions are validated by the static experiment. The mode-I fracture experiment proves that the new common-path speckle interferometer is capable of measuring full-field strain accurately with unlimited shear amounts. A unique attribute of this imaging method is that no tilt between the optical components is required to produce the unlimited shear amount.

Chapter 5

Low-pass filtering compensation in digital holographic microscopy

This chapter presents a low-pass filtering compensation (LPFC) method to compensate for phase aberrations in point diffraction-based common-path digital holographic microscopy [109]. This method estimates the phase aberration from the object hologram by Fourier transform and low-pass spatial filtering. The estimated phase aberration is subtracted from the object phase image to achieve single-hologram phase compensation. The accuracy and capability of LPFC for phase compensation were demonstrated by experiments on a Ronchi grating and a human blood smear. LPFC provides phase compensation for both smooth objects and objects containing abrupt edges, in the special case of a system with relatively high-frequency objects and low-frequency slight phase aberrations. LPFC operates without the need for fitting procedures, iterative steps, or prior knowledge of the optical parameters, which substantially simplifies the process of phase compensation in quantitative phase imaging.

5.1 Introduction

Digital holographic microscopy has been developed for a wide range of applications in the examination of cell pathophysiology [110, 111], semiconductors [112], and 2D materials [113]. The common-path DHM combines common-path geometry and off-axis holography, hence it provides subnanometer level OPD imaging with high temporal stability and the acquisition speed is limited only by the detector [114–117]. Point diffraction-based common-path DHM uses a spatial filter to generate holograms with uniform reference fields, resulting in a compact system with a full field of view [118–122]. In these setups, the zeroth-order beam is low-pass filtered by a pinhole in the Fourier plane of the spatial

filtering lens, which is generally assumed to be a uniform field at the surface of the image sensor [120, 122]. However, due to the uses of a microscope objective (MO) and the complex spatial filter, or a non-optimal imaging system, the zeroth-order beam can be distorted, which introduces phase aberrations to the original off-axis holograms. An automatic aberration compensation is desirable to extract the sample phase images.

Various approaches have been proposed to estimate the phase aberrations in DHM. Commonly used double-exposure compensation (DEC) relies on the manual double-exposure operation [123], allowing the calibration of the DHM setup from the second specimen-free hologram. This method requires that the wavefronts of the specimen-free hologram and the specimen hologram are parallel to each other strictly. Zernike polynomial fitting calculates the phase aberration through numerical processing such as computational fitting procedures, which requires prior knowledge about the optical parameters, or iterative procedures [124–126]. Methods based on deep learning convolutional neural network (CNN) [127], phase variation minimization[128], sparse optimization[129], and synthetic difference[130] use complex algorithms to estimate residual aberrations. The self-overlapping approach has been applied without fitting procedures, but it limits the FOV due to the overlapping operations [131]. The concept of self-reference conjugated hologram was introduced for the phase compensation of smooth objects in a modified Mach-Zehnder interferometer [132]. However, its accuracy is still to be demonstrated quantitatively.

In this chapter, a low-pass filtering compensation (LPFC) method is proposed to compensate for phase aberrations of both smooth objects and objects with abrupt edges in a point diffraction-based common-path DHM, which generates holograms with relatively high-frequency objects and low-frequency slight phase aberrations (the phase contribution due to the aberrations of the whole hologram is less than 10 rad). The capability and accuracy of LPFC are quantitatively proved by the compensation results of a Ronchi grating with abrupt edges and a human blood smear. LPFC requires no fitting procedures, iterative steps, or prior knowledge of the optical parameters, which substantially simplifies the process of phase compensation in quantitative phase imaging.

5.2 Results

5.2.1 Common-path digital holographic microscopy

The schematic of the experimental setup is shown in Figure 5.1(a). A He-Ne laser beam (632 nm, 0.8 mW, HNLS008R-EC, Thorlabs) was expanded and collimated for plane illumination. M1, M2, BE1, and C1 were used to provide illumination in transmission mode. BS1, BE2, C2, and BS2 were for illumination in reflection mode. An infinity-

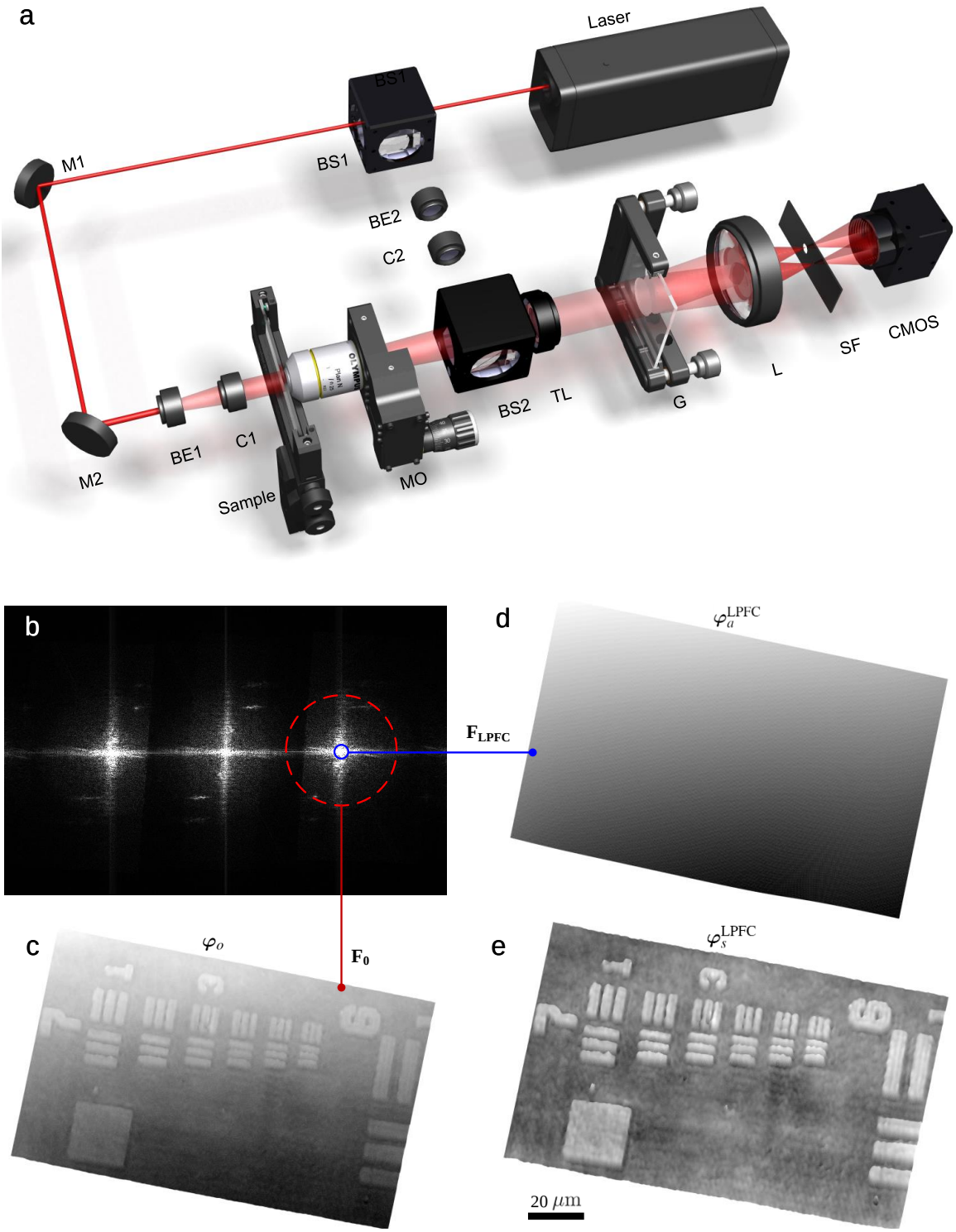

Figure 5.1: See next page for caption.

Figure 5.1: (a) Schematic of the common-path DHM setup. BS1, BS2 beam splitter; M1, M2 mirror; BE1, BE2 beam expander; C1, C2 collimator; MO microscope objective; TL tube lens; G diffraction grating; L lens; SF spatial filter. (b)-(e) Principle of LPFC for phase aberration compensation. (b) The spectrum of the original hologram. $\mathrm{F_o}$, the digital low-pass filtering by the red circle, which delimits the frequency for the object phase image. $\mathrm{F_{LPFC}}$, the digital low-pass filtering with the small blue circle, which delimits the frequency for the phase aberration image. (c) φ_o, the object phase image retrieved from the original hologram without phase compensation. (d) $\varphi_a^{\mathrm{LPFC}}$, the estimated phase aberration image from the original hologram with LPFC. (e) $\varphi_s^{\mathrm{LPFC}}$, the compensated object phase image by subtracting the estimated phase aberration image in (d) from the retrieved original phase image in (c).

corrected MO (NA = 0.25, Plan N, Olympus) was used to produce a magnified image of the sample. TL was used to collimate the light from MO. G (40 c/mm, Applied Image Inc.) was placed at the image plane to separate the magnified image field into multiple orders. L (f=100 mm) was used for imaging and spatial filtering simultaneously. The multiple order image fields were isolated in the Fourier plane (the back focal plane) of L, where SF was placed. SF allowed for passing the entire zeroth diffraction order beam, which was used as the sample field. The first order was physically low-pass filtered by a pinhole, which was used as the reference field. All the other diffraction orders were blocked. A CMOS camera (1280 x 1024 pixels, monochrome sensor, DCC1545M, Thorlabs) was used as the detector.

5.2.2 Principle of low-pass filtering compensation

The hologram of a 1951 USAF test target obtained with the common-path DHM setup in reflection mode was processed to illustrate the steps involved in LPFC [Figures 5.1(b)-(e)]. The intensity image of the original hologram obtained by the detector, $I_o(x,y)$, is generally given by:

$$\begin{aligned} I_o(x,y) &= (R+O)(R+O)^* \\ &= |R|^2 + |O|^2 + R^*O + O^*R, \end{aligned} \tag{5.1}$$

where (x,y) represents the position of the hologram pixels, R and O indicate the reference field and the object field respectively, and the $*$ notation denotes complex conjugate. $|R|^2+|O|^2$ is the DC component. R^*O and O^*R contain the phase information of the sample. To extract the phase image from the original hologram, $I_o(x,y)$ is Fourier transformed and filtered with $\mathrm{F_o}$ [Figure 5.1(b)]:

$$\begin{aligned} \mathbf{C}_o(x,y) &= \mathcal{F}^{-1}\{\mathcal{F}[I_o(x,y)] \cdot \mathrm{F_o}\} \\ &= |R||O|^{i[\varphi_s(x,y)+\varphi_a(x,y)+k_x x+k_y y]}, \end{aligned} \tag{5.2}$$

where $\mathbf{C}_o(x,y)$ is the complex amplitude of the filtered hologram, φ_s is the sample phase image, φ_a is the phase aberration image, and (k_x, k_y) represents the 2D spatial carrier frequency caused by the off-axis holography.

LPFC utilizes the fact that for a system with relatively high-frequency objects and low-frequency slight phase aberrations, the low-frequency components of the local objects are still higher than the frequency of the phase aberrations. The low-frequency components of the whole hologram, which are physically corresponding to the phase aberrations, can be effectively extracted with an appropriate spatial filter. I_o is Fourier transformed and filtered by $\mathrm{F_{LPFC}}$ to estimate the phase aberration image [Figure 5.1(b)]. The diameter of the blue circle ($\mathrm{F_{LPFC}}$) is defined to be as small as possible to eliminate all the high-frequency information, which represents the sample phase image, but sufficiently large to cover all the low-frequency phase aberration of the original hologram. The operator calibrates the diameter of the blue circle only once for the optical system with the same parameters. The complex amplitude of the phase aberration image obtained with LPFC is given by:

$$\begin{aligned}\mathbf{C}_a^{\mathrm{LPFC}}(x,y) &= \mathcal{F}^{-1}\{\mathcal{F}[I_o(x,y)] \cdot \mathrm{F_{LPFC}}\} \\ &= |R||O|^{i[\varphi_a^{\mathrm{LPFC}}(x,y)+k_x x+k_y y]}.\end{aligned} \tag{5.3}$$

The phase images can be extracted from the complex amplitude images by:

$$\varphi(x,y) = \arg[\mathbf{C}(x,y)]. \tag{5.4}$$

φ_o and $\varphi_a^{\mathrm{LPFC}}$ were retrieved from the original hologram of the 1951 USAF [Figures 5.1(c) and 5.1(d)]. To show φ_o and $\varphi_a^{\mathrm{LPFC}}$ clearly, the integer-pixel spectrum-centering processing [133] was used to eliminate the main part of the phase tilt caused by the off-axis holography. $\varphi_s^{\mathrm{LPFC}}$ [Figure 5.1(e)] can be obtained by subtracting $\varphi_a^{\mathrm{LPFC}}$ from φ_o:

$$\varphi_s^{\mathrm{LPFC}}(x,y) = \varphi_o(x,y) - \varphi_a^{\mathrm{LPFC}}(x,y). \tag{5.5}$$

For comparison, the DEC-compensated phase image φ_s^{DEC} can be obtained by subtracting the retrieved phase aberration image φ_a^{DEC} from the retrieved phase image of the original hologram φ_o [123]:

$$\varphi_s^{\mathrm{DEC}}(x,y) = \varphi_o(x,y) - \varphi_a^{\mathrm{DEC}}(x,y), \tag{5.6}$$

where φ_a^{DEC} is obtained from the second specimen-free hologram by:

$$\begin{aligned}\mathbf{C}_a^{\mathrm{DEC}}(x,y) &= \mathcal{F}^{-1}\{\mathcal{F}[I_{\mathrm{DEC}}(x,y)] \cdot \mathrm{F_o}\} \\ &= |R||O|^{i[\varphi_a^{\mathrm{DEC}}(x,y)+k_x x+k_y y]},\end{aligned} \tag{5.7}$$

where I_{DEC} represents the intensity image of the second specimen-free hologram, and $\mathbf{C}_a^{\mathrm{DEC}}$ is the complex amplitude of the second hologram.

5.2.3 LPFC imaging of a Ronchi grating

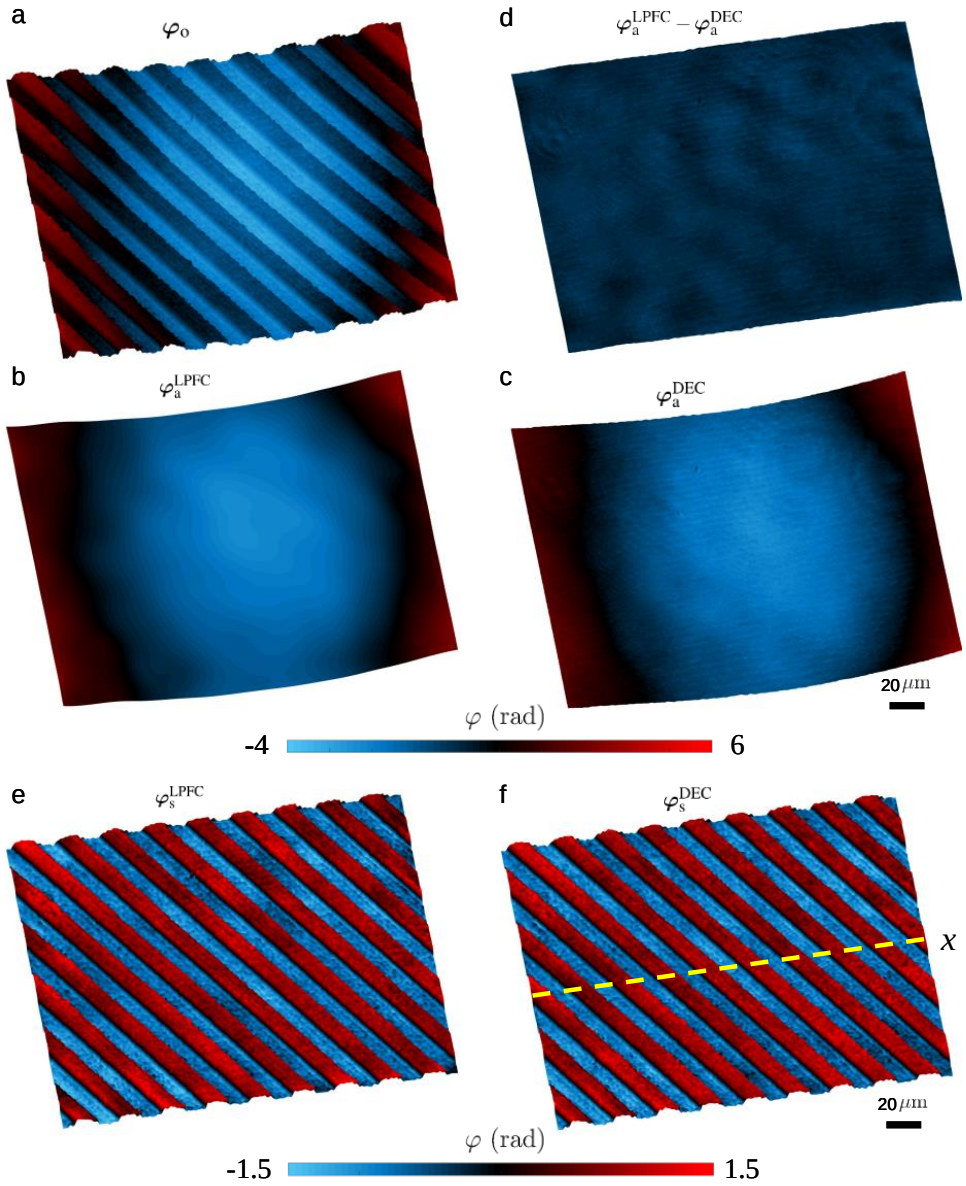

Figure 5.2: Phase compensation of a Ronchi grating. (a) φ_{o}, (b) $\varphi_{\mathrm{a}}^{\mathrm{LPFC}}$, (c) $\varphi_{\mathrm{a}}^{\mathrm{DEC}}$, (d) $\varphi_{\mathrm{a}}^{\mathrm{LPFC}} - \varphi_{\mathrm{a}}^{\mathrm{DEC}}$, (e) $\varphi_{\mathrm{s}}^{\mathrm{LPFC}}$, and (f) $\varphi_{\mathrm{s}}^{\mathrm{DEC}}$.

To demonstrate the feasibility of the developed method, a Ronchi grating (40 c/mm) was tested based on the common-path DHM setup in transmission mode (Figure 5.2). φ_{o} [Figure 5.2(a), after the integer-pixel spectrum-centering processing and phase unwrap-

ping] shows that the large parabolic phase aberration hides the phase contribution of the specimen. $\varphi_{\mathrm{s}}^{\mathrm{LPFC}}$ [Figure 5.2(e)] was obtained by subtracting $\varphi_{\mathrm{a}}^{\mathrm{LPFC}}$ [Figure 5.2(b)] from φ_{o} [Figure 5.2(a)]. For comparison, a second hologram without the sample was captured as the reference hologram to estimate the phase aberration image with DEC. $\varphi_{\mathrm{s}}^{\mathrm{DEC}}$ [Figure 5.2(f)] was obtained by subtracting $\varphi_{\mathrm{a}}^{\mathrm{DEC}}$ [Figure 5.2(c)] from φ_{o} [Figure 5.2(a)]. $\varphi_{\mathrm{a}}^{\mathrm{LPFC}} - \varphi_{\mathrm{a}}^{\mathrm{DEC}}$ [Figure 5.2(d)], the residual image (defined as the difference between the LPFC-estimated and the DEC-estimated phase aberration image) fluctuated around zero. Both LPFC and the conventional DEC eliminated the parabolic phase aberration and extracted φ_{s} effectively [Figures 5.2(e) and 5.2(f)], and the compensation results were in agreement.

The compensation results in Figure 5.2 were further quantitatively compared to verify the accuracy of LPFC (Figure 5.3). $\varphi_{\mathrm{s}}^{\mathrm{LPFC}}|_x$ and $\varphi_{\mathrm{s}}^{\mathrm{DEC}}|_x$ [Figure 5.3(a)] agreed well with each other, and they were consistent with the periodic structure of the Ronchi grating. ΔOPD [Figures 5.3(b) and 5.3(c)] was measured from the histograms of the phase images [Figures 5.2(a), 5.2(e), and 5.2(f)]. $\Delta\mathrm{OPD}_{\mathrm{LPFC}}$ and $\Delta\mathrm{OPD}_{\mathrm{DEC}}$ were 162.6 nm and 163.3 nm, respectively ($\approx$ 99.6% agreement). Figures 5.3(a)-5.3(c) quantitatively proved that the compensation results of LPFC and DEC were in good agreement. A digital low-pass spatial filter with a radius of 6 pixels was used for phase aberration compensation of the Ronchi grating. The geometric center of the filter was located in the peak position in the spectrum. The performances of the low-pass spatial filters with different sizes (r=2, 6, and 25 pixels, respectively) were evaluated by comparing the LPFC_{1-3}-estimated aberration images with the original phase image and the DEC-estimated aberration image [Figure 5.3(d)]. Unlike $\varphi_{\mathrm{a}}^{\mathrm{LPFC}_3}|_x$, $\varphi_{\mathrm{a}}^{\mathrm{LPFC}_2}|_x$ was much smoother, indicating that LPFC_2 eliminated all the sample information. $\varphi_{\mathrm{a}}^{\mathrm{LPFC}_1}|_x$ fluctuated irregularly as LPFC_1 did not contain the complete low-frequency phase aberration of the original hologram. $\varphi_{\mathrm{a}}^{\mathrm{LPFC}_2}|_x$ and $\varphi_{\mathrm{a}}^{\mathrm{DEC}}|_x$ were in agreement.

5.2.4 LPFC imaging of red blood cells

Experiments on a human blood smear specimen with high-density red blood cells (RBCs) were performed based on the same DHM setup in transmission mode (Fig. 5.4). Both $\varphi_{\mathrm{a}}^{\mathrm{LPFC}}$ and $\varphi_{\mathrm{a}}^{\mathrm{DEC}}$ [Figs. 5.4(b) and 5.4(c)] presented the phase aberrations of φ_{o} [Fig. 5.4(a)]. The residual image $\varphi_{\mathrm{a}}^{\mathrm{LPFC}} - \varphi_{\mathrm{a}}^{\mathrm{DEC}}$ [Fig. 5.4(d)] fluctuated around zero. Figs. 5.4(e) and 5.4(f) showed that both LPFC and DEC revealed an overall cell distribution of the blood smear. The magnified images [Figs. 5.4(g) and 5.4(h)] showed that both LPFC and DEC presented the complete discocytic morphology of the individual RBCs. The quantitative comparison between $\varphi_{\mathrm{s}}^{\mathrm{LPFC}}|_x$ and $\varphi_{\mathrm{s}}^{\mathrm{DEC}}|_x$ [Fig. 5.4(i)] illustrated the compensation results of LPFC agreed with that of DEC.

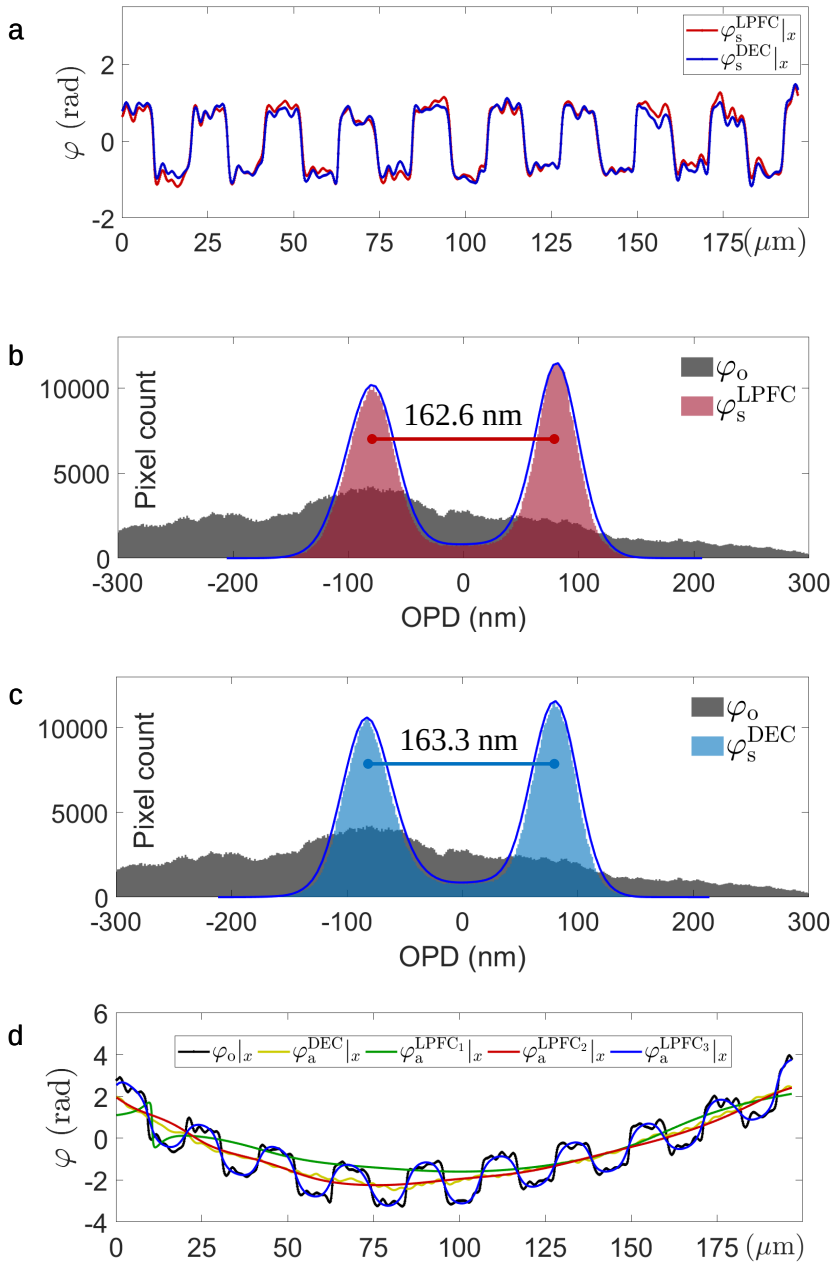

Figure 5.3: Accuracy analysis of LPFC. (a) $\varphi_s^{LPFC}|_x$ and $\varphi_s^{DEC}|_x$, the phase profiles of φ_s^{LPFC} and φ_s^{DEC} [Figures 5.2(e) and 5.2(f)] along the dotted line x [Figure 5.2(f)], respectively. (b) The histograms of the phase images φ_o and φ_s^{LPFC} [Figures 5.2(a) and 5.2(e)]. (c) The histograms of the phase images φ_o and φ_s^{DEC} [Figures 5.2(a) and 5.2(f)]. ΔOPD_{LPFC} (162.6 nm) and ΔOPD_{DEC} (163.3 nm), the top-bottom OPD difference of the Ronchi grating by LPFC and DEC, respectively. (d) The performances of the low-pass filters $LPFC_{1-3}$ (r=2, 6, and 25 pixels, respectively). $\varphi_o|_x$, $\varphi_a^{DEC}|_x$, and $\varphi_a^{LPFC_{1-3}}|_x$, the profiles of φ_o [Figure 5.2(a)], φ_a^{DEC} [Figure 5.2(c)], and $\varphi_a^{LPFC_{1-3}}$ along the dotted line x [Figure 5.2(f)], respectively.

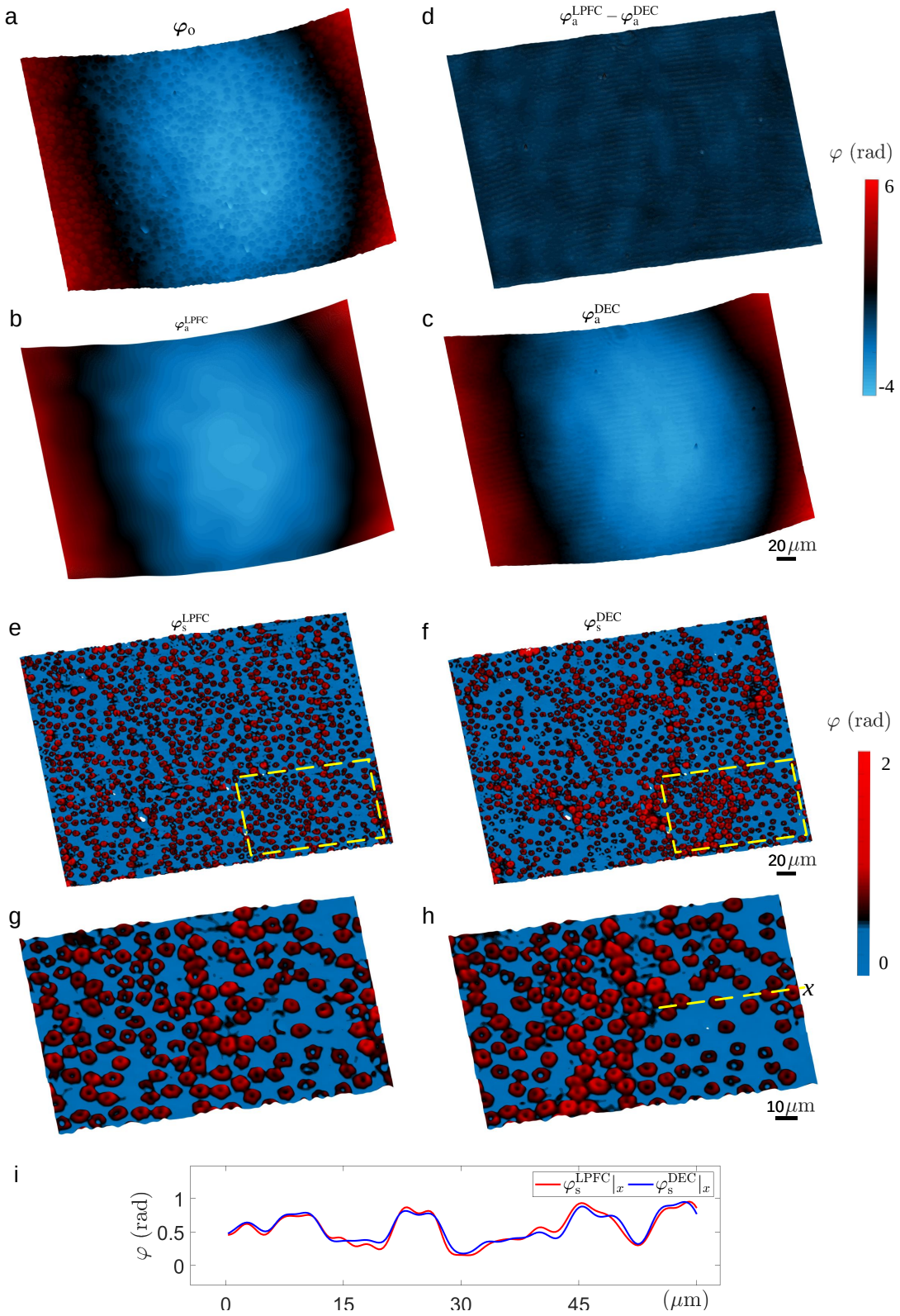

Figure 5.4: See next page for caption.

Figure 5.4: Phase compensation of a human blood smear specimen. (a) φ_{o}, (b) $\varphi_{\mathrm{a}}^{\mathrm{LPFC}}$, (c) $\varphi_{\mathrm{a}}^{\mathrm{DEC}}$, and (d) $\varphi_{\mathrm{a}}^{\mathrm{LPFC}} - \varphi_{\mathrm{a}}^{\mathrm{DEC}}$. (e) $\varphi_{\mathrm{s}}^{\mathrm{LPFC}}$ and (f) $\varphi_{\mathrm{s}}^{\mathrm{DEC}}$, the phase images of the whole human blood smear compensated with LPFC and DEC, respectively. (g) and (h), the magnified images of (e) and (f) to show the morphology of individual RBCs. (i) $\varphi_{\mathrm{s}}^{\mathrm{LPFC}}|_x$ and $\varphi_{\mathrm{s}}^{\mathrm{DEC}}|_x$, the phase profiles of (g) and (h) along the dotted line x in (h).

5.3 Conclusion

In conclusion, we developed the LPFC method for single-hologram phase aberration compensation of both smooth objects and objects with abrupt edges, in the special case of a system with relatively high-frequency objects and low-frequency slight phase aberrations. The accuracy and capability of LPFC were quantitatively validated through experiments on a Ronchi grating with abrupt edges and a human blood smear based on a point diffraction-based common-path DHM. No fitting procedures, iterative steps, or prior knowledge of the optical parameters are required to remove the unwanted aberrations with LPFC, which substantially simplifies the process of phase aberration compensation in quantitative phase imaging.

Chapter 6

Multibeam array interferometric microscopy

High-throughput microscopic imaging is highly desirable in biomedical applications. Advances in computational microscopy have achieved high space-bandwidth products and even permitted gigapixel imaging in a stepwise fashion, yet temporal resolution remains challenging for investigating live-sample dynamics. In this chapter, we report multibeam array interferometric microscopy (MAIM) for a single-shot high space-bandwidth product [134]. The MAIM method overcomes the limitations of conventional digital holographic microscopy, providing complex field reconstruction with a maximum 5-fold FOV increase in a single camera acquisition, while maintaining subnanometer optical path-length stability. This is achieved by integrating common-path holographic microscopy, multibeam interference technology, and holographic multiplexing technology. The temporal resolving power of MAIM is significantly higher than that of computational illumination microscopy. MAIM has major advantages over previous holographic multiplexing techniques in that it integrates more wavefronts and offers high temporal stability. The fundamentals of MAIM are analyzed theoretically. As a demonstration, we build MAIM prototypes to increase the FOV by factors of 5, 4, and 3, respectively. We present proof-of-concept MAIM imaging results of both natural and artificial samples and show biomedical applications such as monitoring subcellular dynamical phenomena in flowing live erythrocytes *in vitro* and label-free micro-refractometry imaging of unstained cancer tissue slices. MAIM gives rise to (ultra)fast or long-term (time-lapse) imaging of nanoscale dynamics of unstained live samples *in vitro* with a high throughput.

6.1 Introduction

The SBP characterizes the throughput of an imaging system by counting the number of the minimum resolvable spots in the maximum FOV [135]. For a digital microscope, its SBP is fundamentally limited by both the objective lens and the detector. Although modern objective lenses provide a high SBP (∼5-35 megapixels), only part of the information transmitted by the optical system can be sampled or digitized due to the limited number of pixels of most commercial image sensors. This "SBP gap" caused by the mismatch between objective lenses and optoelectronic sensors is in general bridged by matching the effective pixel size to the optical resolution, resulting in major sacrifices of FOV. For example, the combination of a 20× objective lens (e.g., 0.8 NA, 26.5 FN, ∼23.8-megapixel SBP at 632 nm) and a commercial CMOS sensor (e.g., 1024×1080, ∼1.3 megapixels) would waste >90% FOV of the objective lens. This gap limits many biomedical applications that require large-scale high-resolution imaging, such as digital pathology [136, 137], cell detecting [138, 139], and imaging flow cytometry [140–142].

Increasing the SBP of optical microscopes has garnered great interest in recent decades. Mechanical scanning methods rely on precise control over actuation, and moving elements can introduce extra vibration noise. synthetic-aperture and computational illumination techniques increase the resolving power of low NA objective lenses by mechanically or electrically scanning in Fourier space (FS), thus expanding the pupil function of their optical systems to achieve a high SBP [30, 143–148]. Since the enlarged pupil functions are built from multiple low-resolution image sets, these approaches usually require multiple recordings and computation-intensive digital reconstructions. For example, synthetic-aperture digital holographic microscopy requires at least 4 holograms with azimuthal angles at 90° intervals [144], the computational out-of-focus imaging method combines at least 3-5 slightly out-of-focus images [147], synthetic-aperture on-chip microscopy operates at 22 different illumination angles [145], and Fourier ptychographic microscopy (FPM) records over 100 sequential images [30]. FPM that adopts a source-coded strategy or a data-driven strategy requires fewer images [146, 149, 150]. Multiple-recording limits these high-SBP techniques for high temporal-resolved *in vitro* imaging.

Holographic multiplexing permits recovering multiple complex wavefronts in a single camera acquisition by integrating several object waves into one single spatially multiplexed hologram [74, 151–153]. The single-shot capability and the compatibilities with various holographic imaging devices of holographic multiplexing allow for high temporal-resolved optical imaging applications such as ultrafast pulse holography [154, 155], single-step synthetic-aperture holography [156–158], high-speed holographic tomography [159], and snapshot multispectral imaging [160]. Holographic multiplexing-based large-FOV quan-

titative phase imaging methods increase the SBP without compromising other imaging parameters, such as temporal resolution [117, 161–163]. Despite these advantages, these methods also present certain limitations. For example, the maximum number of the multiplexed wavefronts is limited by the complex multichannel interferometric setup. Adding channels (wavefronts) can significantly increase the optomechanical complexity and alignment requirements such as interference angle controls and FOV calibrations.

In this work, we report a new single-shot QPI method with high-SBP. This method, termed multibeam array interferometric microscopy (MAIM), increases the SBP of conventional DHM by a maximum factor of 5, while maintaining subnanometer optical pathlength stability and camera frame rate-limited temporal resolution. This is achieved by combining common-path geometry from point-diffraction interferometry [109, 118, 120, 164], single-shot recording associated with multibeam interference [165–168], and multiple-wavefront recovery from holographic multiplexing [152]. The multibeam array is generated through orthogonal grating modulation (OGM) and filtered by a customized 2D aperture array to achieve reconstructable multibeam array interference. Complex amplitude images corresponding to variable subsets of a sample can be extracted from the spatially multiplexed interferogram and stitched to generate a synthetic image with large FOV. MAIM overcomes the limitation of conventional holographic microscopy and allows for quantifying (ultra)fast or long-term (time-lapse) nanoscale dynamics of live samples with high throughput.

The concept of multibeam array interference requires neither complex and bulky optical components nor optical component tiltings, which significantly reduces the optomechanical complexity of optical setups for holographic multiplexing and permits integrating more waves. This compactness also results in high temporal stability and easy operations. For example, tilting-free leads to fewer optical alignments such as precise controls over the interference angles, compared with the systems based on multiple tilted mirrors [117, 162]. In addition, although the method requires a FOV calibration, it calibrates by varying distances among the optical components, and no image rotation occurs [117, 161]. Not limited to FOV multiplexing, the concept can be potentially applied to other holographic imaging devices that require multiple wavefronts recoveries, such as high-speed synthetic-aperture holographic microscopy [158] and high-speed holographic tomography [159].

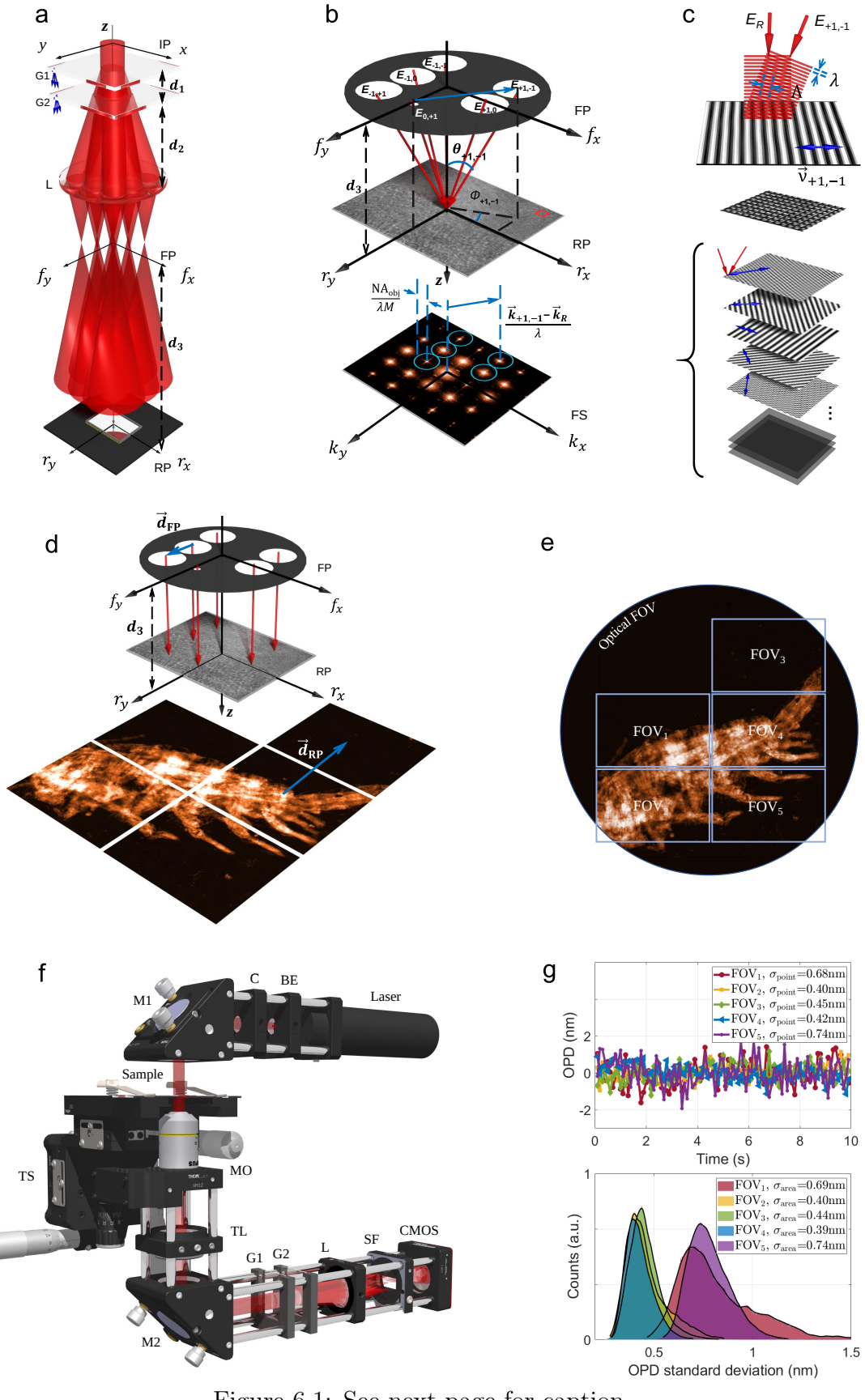

Figure 6.1: See next page for caption.

Figure 6.1: Basic principles, prototype setup, and characterization of MAIM. (a) The common-path multibeam array interference module. IP, imaging plane; G1/G2, Ronchi gratings; L, lens; FP, Fourier plane of L; RP, recording plane; d_1-d_3, distances between G1 and G2, G2 and L, and FP and RP. (b) The customized 2D spatial filter (SF) for 5-fold FOV enlargement. A spatially multiplexed interferogram generated by the 6-beam interference and the corresponding FS components are shown in the plane RP and FS, respectively. (c) Generation of 2D frequency shifts in FS. The periodic 2D lattice structures are magnified from the box area of the spatially multiplexed interferogram in (b). The single-frequency fringes are reconstructed from the lattice structure pattern by inverse Fourier transform. (d) 2D space shift vectors among the multiple sample image subsets. (e) The relations among the optical FOV, the camera FOV, and the synthetic MAIM FOV. (f) Transmissive MAIM prototype setup. BE, beam expander; C, collimator; M1/M2, mirrors; TS, 3D translation stage; MO, microscope objective; TL, tube lens. (g) Temporal stability characterization. The single-point OPD fluctuations from the 5 FOV subsets have standard deviations of 0.68 nm, 0.40 nm, 0.45 nm, 0.42 nm, and 0.74 nm, respectively. The histograms of the 2D OPD standard deviation maps corresponding to the entire individual FOV subsets show peaks at 0.69 nm, 0.40 nm, 0.44 nm, 0.39 nm, and 0.74 nm, respectively.

6.2 Results

6.2.1 Principle of multibeam array interferometric microscopy

MAIM integrates multiple object images into one digital hologram by utilizing the "third" dimension space of the camera, the dynamic range. Figure 6.1(a) illustrates the common-path multibeam array interference module based on OGM. Two identical Ronchi grating layers (G1/G2) with a diffraction angle of $\theta_{\pm 1} = \sin^{-1}(\lambda/d)$ (λ, wavelength of illumination; d, line pair width of the gratings) are assembled orthogonally after the imaging plane (IP). G1 and G2 replicate the microscope image twice to generate a 3×3 diffraction beam array. A lens (L) is used for spatial filtering and imaging simultaneously. A custom-built 2D spatial filter (SF) is placed at the Fourier plane (FP) of L [Figure 6.1(b)], where the diffraction beams are focused and spatially separated.

The 2D aperture array arrangements of SF are the key innovation of this imaging method. Without the aperture array, the 3×3 multibeam array generates non-reconstructable interference consisting of C_9^2 single-frequency interferograms on the recording plane (RP). The total electric field can be described by:

$$\mathbf{E}(\mathbf{r}) = \sum_{m=-1}^{1} \sum_{n=-1}^{1} \mathbf{E}_{m,n}(\mathbf{r}) e^{i[\varphi_{m,n}(\mathbf{r}) + \vec{k}_{m,n} \cdot \vec{r}]}, \tag{6.1}$$

where $\mathbf{E}_{m,n}(\mathbf{r})e^{i[\varphi_{m,n}(\mathbf{r})+\vec{k}_{m,n}\cdot\vec{r}]}$ indicates the grating-modulated electric field with a diffraction order of (m,n), $\vec{k}_{m,n}$ represents the 2D wave vector induced by OGM, which is related to the 3D incident angle of the diffraction beam $\mathbf{E}_{m,n}$ with respect to the plane RP, and $\vec{r}$ represents the spatial vector in the plane RP. The 2D aperture array passes the entire frequency content of the selected orders from the diffraction beam array, providing a group of sample waves corresponding to variable FOV subsets. Another beam is low-pass filtered by a pinhole (∼30 μm diameter) and works as a reference wave. All the other beams are blocked. The custom-built 2D aperture array transforms the non-reconstructable interferogram caused by 3×3 multibeam array interference into a reconstructable one. As an example, the role of a 2D aperture array for reconstructable 6-beam interference, i.e., capable of 5-fold FOV enlargement, is illustrated in Figure 6.1(b). After passing through SF, six diffraction beams interfere on the CMOS sensor: (m,n)= (-1, -1), (-1, 0), (-1, +1), (0, +1), (+1, -1), and (+1, 0), respectively. $\mathbf{E}_{0,+1}$ is low-pass filtered and works as the reference wave. The corresponding total electric field includes C_6^2 single-frequency interferograms:

$$\mathbf{E}(\mathbf{r}) = \sum_{i=1}^{5} \boldsymbol{\psi}_{\mathrm{i}}(\mathbf{r}) + \boldsymbol{\psi}_{\mathrm{residue}}(\mathbf{r}), \tag{6.2}$$

where $\boldsymbol{\psi}_{\mathrm{i}}$ equals $(E_R + E_{m,n})$, representing the reconstructable single-frequency interferograms generated by the interference between the reference wave and the sample waves from FOV_{1-5}, respectively. The intensity of the reference wave $\mathbf{E}_R$ is proportional to the spatial average of the original diffraction wave $\mathbf{E}_{0,+1}$. The intensity of $\boldsymbol{\psi}_i$ can be described as:

$$I_{\mathrm{i}}(\mathbf{r}) = D_{\mathrm{i}}(\mathbf{r}) + C_{\mathrm{i}}(\mathbf{r})e^{i(\vec{k}_{m,n}-\vec{k}_R)\cdot\vec{r}} + C_{\mathrm{i}}^*(\mathbf{r})e^{-i(\vec{k}_{m,n}-\vec{k}_R)\cdot\vec{r}}, \tag{6.3}$$

where D_{i} equals $(E_R^2 + E_{m,n}^2)$, C_{i} equals $E_R^* E_{m,n} \cdot e^{i(\varphi_{m,n}-\varphi_R)}$, and C_{i}^* denotes the complex conjugate of C_{i}. After applying Fourier transform, the FS components of I_{i} can be written as:

$$\widetilde{I}_{\mathrm{i}}(\mathbf{k}) = \widetilde{D}_{\mathrm{i}}(\mathbf{k}) + \widetilde{C}_{\mathrm{i}}(\mathbf{k}-\boldsymbol{\nu}_{m,n}) + \widetilde{C}_{\mathrm{i}}^*(\mathbf{k}+\boldsymbol{\nu}_{m,n}). \tag{6.4}$$

The frequency shift vector $\boldsymbol{\nu}_{m,n}$ equals $(\vec{k}_{m,n} - \vec{k}_R)/\lambda$. Furthermore, by basic principles of light interference, the vertical and the horizontal components of $\boldsymbol{\nu}_{m,n}$ can be quantified by the polar angles $\theta_{m,n}$ and θ_R and the azimuthal angles $\phi_{m,n}$ and ϕ_R [Figure 6.1(b)]:

$$\boldsymbol{\nu}_{m,n} = 1/\lambda \begin{bmatrix} (\sin\theta_{m,n}\cos\phi_{m,n} - \sin\theta_R\cos\phi_R)\cdot\mathbf{e}_x \\ (\sin\theta_{m,n}\sin\phi_{m,n} - \sin\theta_R\sin\phi_R)\cdot\mathbf{e}_y \end{bmatrix}. \tag{6.5}$$

The frequency shift vector is proportional to the distance between the focused spots of the reference beam and the sample beams in FP [Figure 6.1(b)]. Modulated by the customized

2D aperture array, the multibeam interference containing variable FOV subsets creates fringe patterns with different directions [Figure 6.1(c)]. In addition, the spatial frequency limit is determined by the pupil function (optical transfer function) of an imaging system. Specifically, for the current setup with coherent illumination, since the 2D aperture array allows passing the entire frequency content of the selected diffraction beams, the maximum spatial frequency is mostly limited by the objective lens, corresponding to a spatial frequency of $\leq \mathrm{NA}_{\mathrm{obj}}/\lambda M$, where $\mathrm{NA}_{\mathrm{obj}}$ is the numerical aperture of the objective lens, and M is the transverse magnification factor (Figures 6.8 and 6.9). Thus, by adjusting the frequency shift vector matrix and selecting an appropriate M, MAIM provides a uniformly isolated FS components distribution to avoid crosstalk and maintain spatial resolution [Figure 6.1(b)].

The multibeam array interference module also results in a transverse isotropic space shift matrix. The amounts of the space shifts are determined by the diffraction angles and projection geometry. For example, as $\mathbf{E}_{-1,-1}$, $\mathbf{E}_{-1,0}$, and $\mathbf{E}_{-1,+1}$ share the same first diffraction order [Figure 6.1(d)], no space shift exists among them along r_x in the plane RP, while the shifts are arithmetic along r_y given by the second diffraction orders. The space shift vector between two sample images in the plane RP, $\vec{d}_{\mathrm{RP}}$, equals $(-\vec{d}_{\mathrm{FP}} \cdot M)$, where $\vec{d}_{\mathrm{FP}}$ represents the vector given by two focused spots of the sample waves in the plane FP.

Both the frequency and the space shift vectors are proportional to the spacings among the focused spots in the plane FP. Therefore, the amounts of these shift vectors can be adjusted smoothly by varying the axial distances among the optical components to achieve a uniform FS components distribution and a synthetic FOV without gaps or overlaps. Figure 6.1(e) illustrates the relations among the optical FOV, the camera FOV, and the synthetic FOV of MAIM when the space shift vectors are optimized. The component tilt-free feature significantly simplifies the optical alignment processes such as the FOV calibrations and the interference angle adjustments that are usually required for holographic multiplexing imaging.

Unlike synthetic-aperture methods [30, 144], which achieve high-SBP imaging by combining multiple time-sequential measurements to increase the spatial resolution in a certain FOV, MAIM follows an opposite strategy: expanding FOV with fixed spatial resolution. Synthetic-aperture approaches such as FPM [30, 146] usually require a massive redundancy of the Fourier spectrum to promote fast and robust image convergence. The main design strategy of MAIM is similar to that of mechanical scanning microscopy [169, 170]. However, because no optical component moving or sample scanning is required, our setup eliminates the design challenges associated with scanning detection schemes and thus allows for imaging dynamical phenomena with high sensitivity.

A transmissive MAIM implementation is illustrated in Figure 6.1(f). The laser beam is expanded and collimated by a beam expander (BE) and a collimator (C), respectively, for plane wave illumination. An infinity-corrected microscope objective (MO), together with a precision 3D translation stage (TS) and a tube lens (TL), provides magnified sample images. The multibeam array interference module is introduced after TL to achieve single-shot high-SBP phase imaging. A CMOS sensor is adopted for recording.

As the multiple diffraction beams propagate along the same optical path and traverse the same optical components, our system significantly reduces the longitudinal phase noise. The temporal stability of the MAIM prototype setup for 5-fold FOV enlargement was characterized through a sample-free imaging experiment [Figure 6.1(g)]. A group of 100 sample-free images was recorded at 10 fps, and noise analysis was performed on both the single points and the entire images from the five FOV subsets. The optical path delays (OPDs) associated with the single points and the histograms of the 2D OPD standard deviation maps corresponding to the entire image subsets show that almost all the pixels from the 5 FOVs fluctuate at the subnanometer level. This temporal stability was achieved with a CMOS sensor. The subnanometer optical path-length stability of our MAIM prototype allows for imaging cell dynamics of tens to hundreds of nanometers (considering the refractive index contrast) *in vitro* with high throughput.

6.2.2 Proof-of-concept imaging experiments

In the following, we show three groups of imaging results obtained with the MAIM prototypes that enlarge the FOV by factors of 5, 4, and 3, respectively. We termed these prototypes $5f$-MAIM, $4f$-MAIM, and $3f$-MAIM, respectively. Although $5f$-MAIM provides the highest space-bandwidth efficiency, $4f$-MAIM permits holographic imaging with a regular rectangle imaging field. In addition, $3f$-MAIM provides the widest FOV range and potentially allows for a wider FOV by passing higher-order diffraction beams. As a proof of concept, we imaged both natural and artificial structures, a *Daphnia* cross-section sample and glass microspheres (75 μm mean diameter), respectively. A 10× objective lens (0.25 NA) with a diffraction-limited resolution of 1.1 μm was adopted in the MAIM setups for these experiments.

$5f$-MAIM. The sample-free interferogram contains all the wavefront curvatures and thus is used as the reference to compensate for phase aberrations [Figure 6.2(a)]. The enlargement of the box area shows the asymmetric lattice patterns caused by 6-beam interference [Figure 6.2(b)]. In the typical $5f$-MAIM Fourier spectrum, the cross-correlation elements marked by the blue dotted circles contain the complex amplitudes of the respective FOV subsets [Figure 6.2(c)]. The original sample interferogram records the optical path-length changes of the light wave after passing through a *Daphnia* cross-section sample [Figure

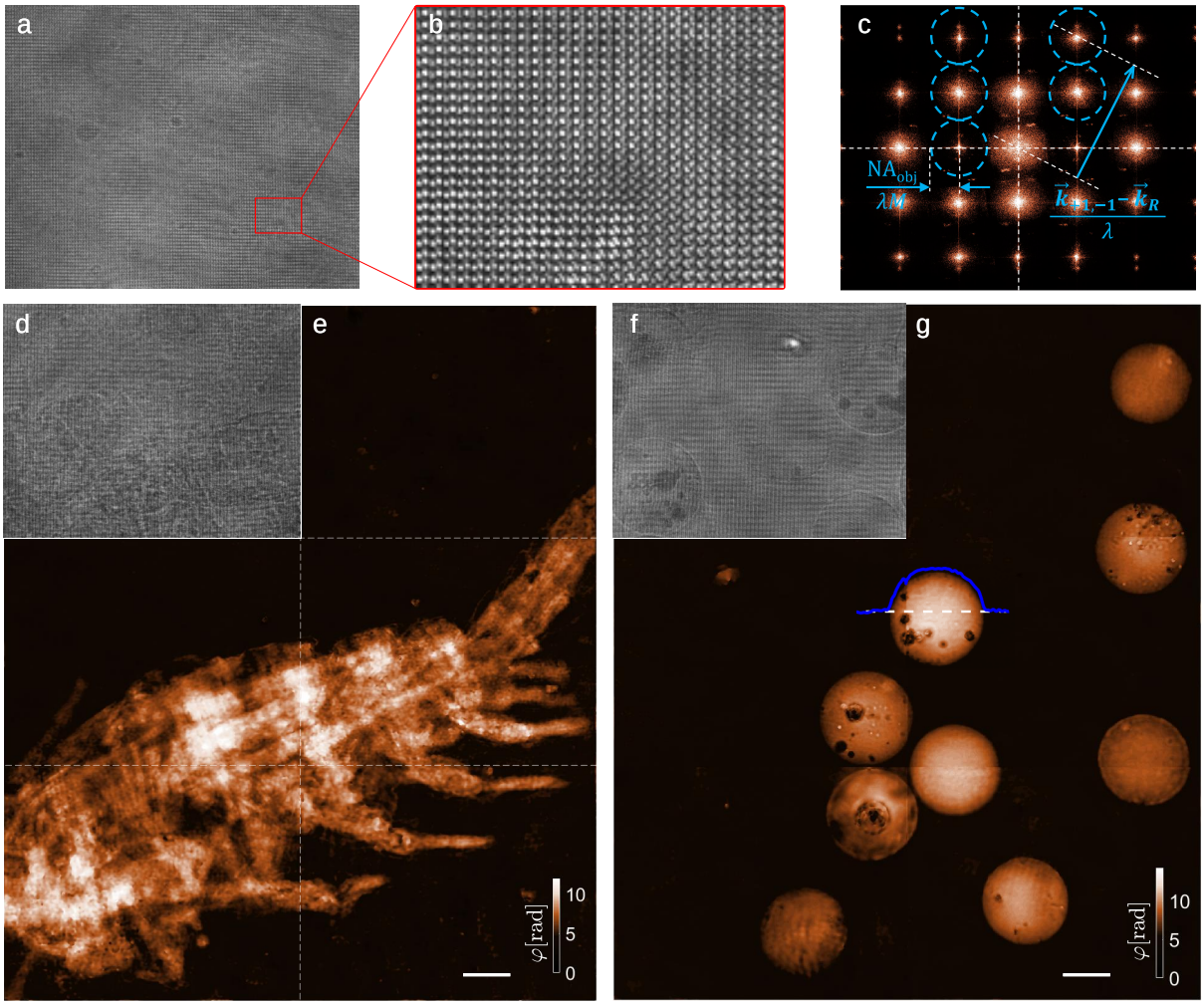

Figure 6.2: $5f$-MAIM phase imaging. (a) Sample-free interferogram for wavefront aberration compensation, and (b) the corresponding lattice structure pattern caused by 6-beam interference. (c) Typical FS components distribution of $5f$-MAIM. The blue dotted circles delimit the FS components for the five single-frequency interferograms correspondingly. (d) Original interferogram of a *Daphnia* cross-section sample, and (e) the corresponding synthetic $5f$-MAIM phase image. (f) Original interferogram of glass microspheres (75 µm mean diameter) and (g) the corresponding synthetic $5f$-MAIM phase image. The blue line illustrates the phase profile of a microsphere along the dotted line. Scale bars, 40 µm.

6.2(d)]. As the multiple wavefronts containing phase information from different parts of the sample overlap with each other, the morphological details of the *Daphnia* sample are not clearly observable in the original spatial-multiplexed interferogram. Real-time phase imaging can be feasible by adopting a graphics processing unit (GPU) due to the highly parallelizable phase reconstruction algorithm of MAIM (see Methods for the details of image reconstruction). We select five small subregions in the FS of Figure 6.2(d) by the circle sets in Figure 6.2(c) and apply inverse Fourier transform to yield the synthetic $5f$-MAIM phase image [Figure 6.2(e)]. The synthetic FOV covers almost the entire *Daphnia* sample with a CMOS sensor recording only $\sim$1/4 of the whole target. The synthetic image reveals overall profiles, organ distributions, and fine morphological details of the *Daphnia* sample. No crosstalk exists. The 5 FOV subsets connect smoothly without gaps or overlaps. The imaging performance of the synthetic wide-field phase image presents no obvious differences among these 5 FOV subsets in terms of spatial resolution and optical focusing. Additionally, we also imaged glass microspheres immersed in microscope immersion oil. The original interferogram and the corresponding synthetic $5f$-MAIM phase image are shown in Figures 6.2(f) and (g). The phase images of the individual microspheres present the spherical distributions that are consistent with the known shape of the sample. The small bubbles are caused by incomplete infiltration and defects of the microspheres.

$4f$-MAIM. Figure 6.3(a) illustrates an implementation of MAIM that enlarges the FOV by a factor of 4. Compared with $5f$-MAIM, the 2D aperture array of $4f$-MAIM blocks the asymmetric diffraction order $\mathbf{E}_{-1,+1}$ to ensure a regular imaging field, transforming the 3×3 multibeam array interference into reconstructable 5-beam interference containing C_5^2 single-frequency interferograms. Consequently, the FS components of $\mathbf{E}_{+1,-1}$ are also blocked in FS. The 5-beam interference also results in the symmetrical interference lattice pattern and single-frequency fringe patterns corresponding to the 4 reconstructable interferograms [Figure 6.3(b)]. Figure 6.3(c) illustrates the relations among the optical FOV, the camera FOV, and the synthetic $4f$-MAIM FOV when the space shift vectors are optimized. The temporal stability of the $4f$-MAIM instrument was also characterized by the same method for $5f$-MAIM [Figure 6.3(d)]. With the same CMOS sensor, both the single-point OPDs and the histograms of the entire 2D OPD standard deviation maps show the subnanometer optical path-length stability of $4f$-MAIM.

The $4f$-MAIM phase images of the *Daphnia* cross-section sample and the glass microspheres [Figures 6.3(e) and (f)] show equivalent image qualities as compared with that of $5f$-MAIM. The rectangle phase image of the *Daphnia* sample agrees with the corresponding part in Figure 6.2(e). The phase images of the individual glass microspheres are consistent with each other and show the spherical shapes that are consistent with Fig-

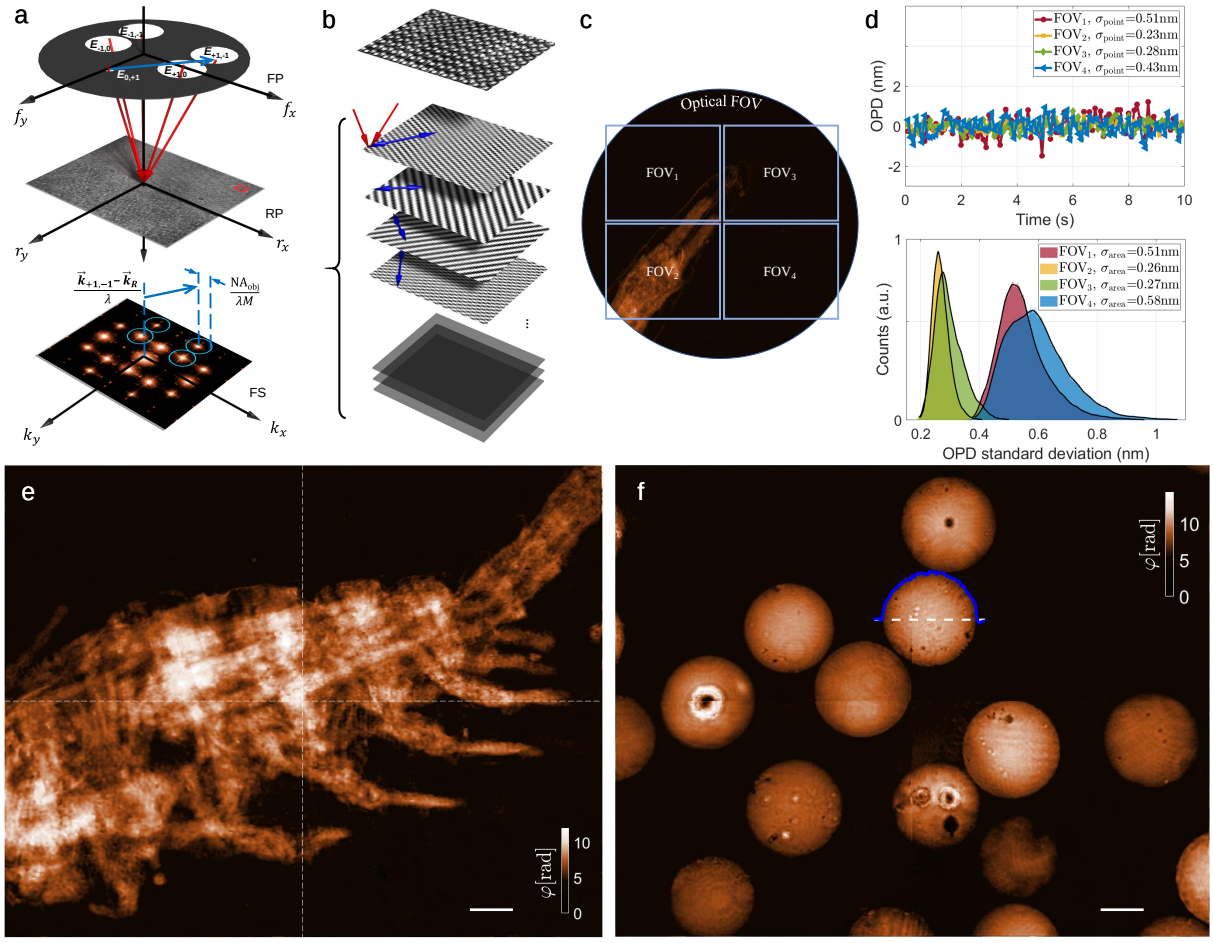

Figure 6.3: $4f$-MAIM. (a) The customized SF for 4-fold FOV enlargement. A spatially multiplexed interferogram generated by 5-beam interference and the corresponding FS components distribution are shown in the plane RP and FS, respectively. (b) Periodic 2D lattice structures zoomed from the box area of the spatially multiplexed interferogram in (a), and the corresponding single-frequency fringe patterns reconstructed by inverse Fourier transform. (c) The relations among the optical FOV, the camera FOV, and the synthetic $4f$-MAIM FOV. (d) Temporal stability characterization of the $4f$-MAIM instrument. The single-point OPD fluctuations from the 4 FOV subsets have standard deviations of 0.51 nm, 0.23 nm, 0.28 nm, and 0.43 nm, respectively. The histograms of the 2D OPD standard deviation maps corresponding to the entire individual FOV subsets show peaks at 0.51 nm, 0.26 nm, 0.27 nm, and 0.58 nm, respectively. Synthetic $4f$-MAIM phase images of (e) the *Daphnia* cross-section sample and (f) the glass microspheres. The blue line illustrates the phase profile of a microsphere along the dotted line. Scale bars, 40 μm.

ure 6.2(g). The 4 FOV subsets of both the *Daphnia* sample and the glass microspheres connect smoothly.

3f-MAIM. The 2D aperture array of 3f-MAIM transforms the 3×3 multibeam array interference into reconstructable 4-beam interference consisting of C_4^2 single-frequency interferograms [Figures 6.4(a) and (b)]. The corresponding symmetrical interference lattice pattern and the 3 reconstructable single-frequency fringe patterns are shown in Figure 6.4(b). It is not the only solution for 3-fold FOV enlargement, e.g., blocking $\mathbf{E}_{+1,-1}$ and $\mathbf{E}_{+1,0}$ in Figure 6.1(b) also achieves 3f-MAIM imaging. However, as the FS components associated with the 3 FOV subsets concentrate in the middle in FS, this 2D aperture array arrangement allows for further SBP optimizations (Figure 6.10) and further FOV expansions.

We characterized the temporal stability of the 3f-MAIM instrument [Figure 6.4(c)] by the same method applied in Figure 6.1(g). With the same CMOS sensor, both the single-point OPDs and the histograms of the entire 2D OPD standard deviation maps verify the subnanometer optical path-length stability of 3f-MAIM. In addition to the smoothly-connected synthetic FOV and the consistency of imaging performance, the phase images of 3f-MAIM [Figures 6.4(d) and (e)] cover a wider imaging field range as compared with that of 5 and 4f-MAIM. This ability to monitor multiple parallel areas can be advantageous when measurements or scans along the entire length of a channel are required, e.g., for imaging flow cytometry [140–142] and optofluidic investigations [169, 171].

6.2.3 4f-MAIM video of live erythrocytes *in vitro*

Human RBCs consist of a lipid bilayer membrane with a thickness of ∼7 nm filled with hemoglobin solution [172]. RBCs exhibit membrane fluctuations on the scale of tens to hundreds of nanometers [120, 173]. Changes in the deformability of RBCs reveal a range of pathologies. For example, cells stored for transfusion are known to exhibit progressively impaired deformability [174]. As a demonstration of dynamic imaging, we reconstructed an 8 s high-SBP video (Video S1) at the camera frame rate-limited 25 fps with our 4f-MAIM system to record the thickness (u) fluctuations of flowing live RBCs (Figure 6.5). A 20× objective lens (0.4 NA) was adopted for *in vitro* imaging.

One frame from the 4f-MAIM video (Video S1) qualifies thickness information across the entire cell population with the subcellular resolution [Figure 6.5(a), see Methods for the details of thickness reconstruction]. The single-frame thickness image with high accuracy can be further segmented automatically for cell counting, detecting, and dry mass measurements [175]. The full-FOV 4f-MAIM video shows both collective cell dynamics and individual cell motions. The full-FOV temporal standard deviations of thickness

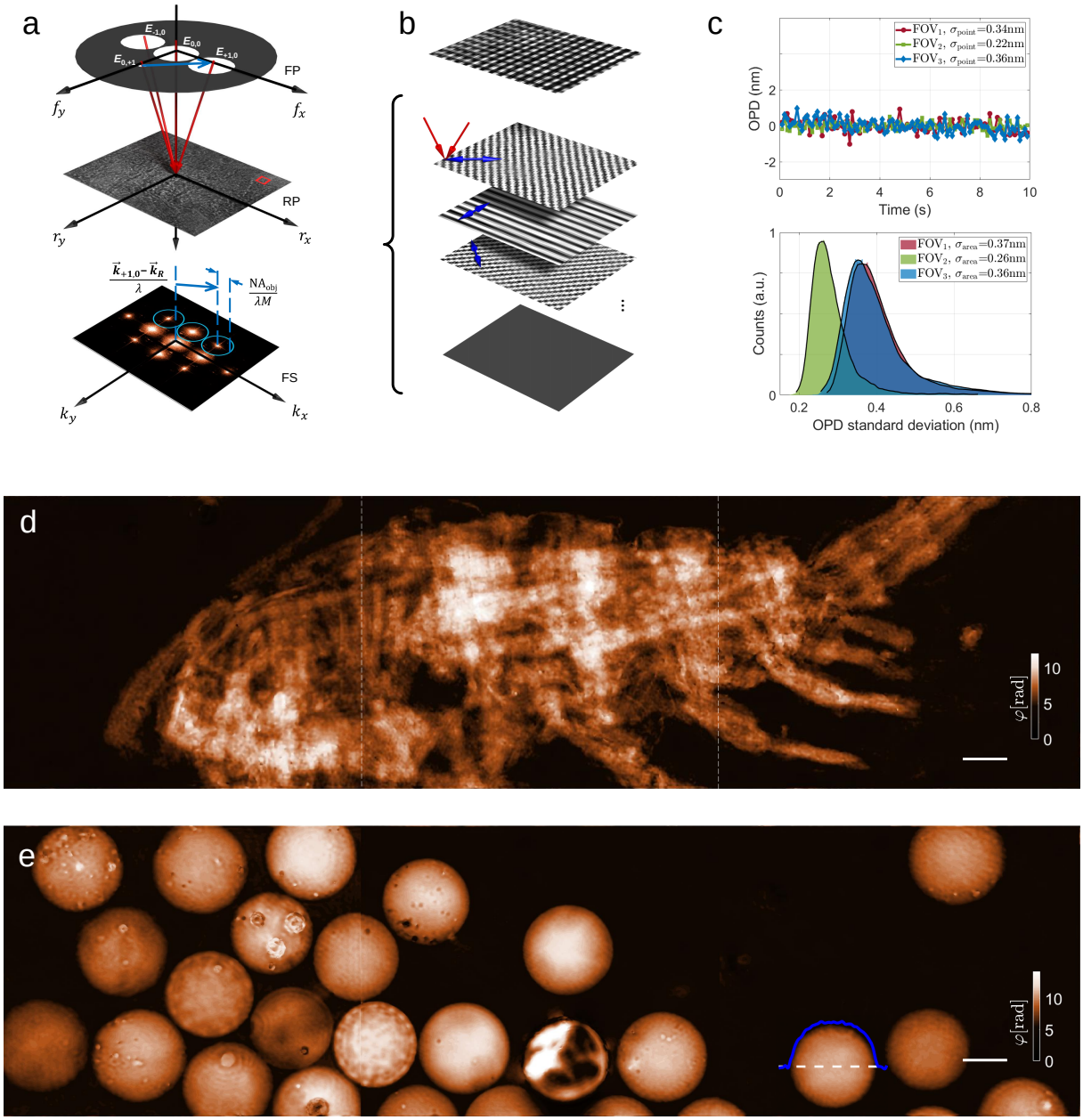

Figure 6.4: $3f$-MAIM. (a) The customized SF for 3-fold FOV enlargement. A spatially multiplexed interferogram generated by 4-beam interference and the corresponding FS components distribution are shown in the plane RP and FS, respectively. (b) Periodic 2D lattice structures zoomed from the box area of the spatially multiplexed interferogram in (a), and the corresponding single-frequency fringe patterns reconstructed by inverse Fourier transform. (c) Temporal stability characterization of the $3f$-MAIM instrument. The single-point OPD fluctuations from the 3 FOV subsets have standard deviations of 0.34 nm, 0.22 nm, and 0.36 nm, respectively. The histograms of the 2D OPD standard deviation maps corresponding to the entire individual FOV subsets show peaks at 0.37 nm, 0.26 nm, and 0.36 nm, respectively. Synthetic $3f$-MAIM phase images of (d) the *Daphnia* cross-section sample and (e) of the glass microspheres. The blue line illustrates the phase profile of a microsphere along the dotted line. Scale bars, 40 μm.

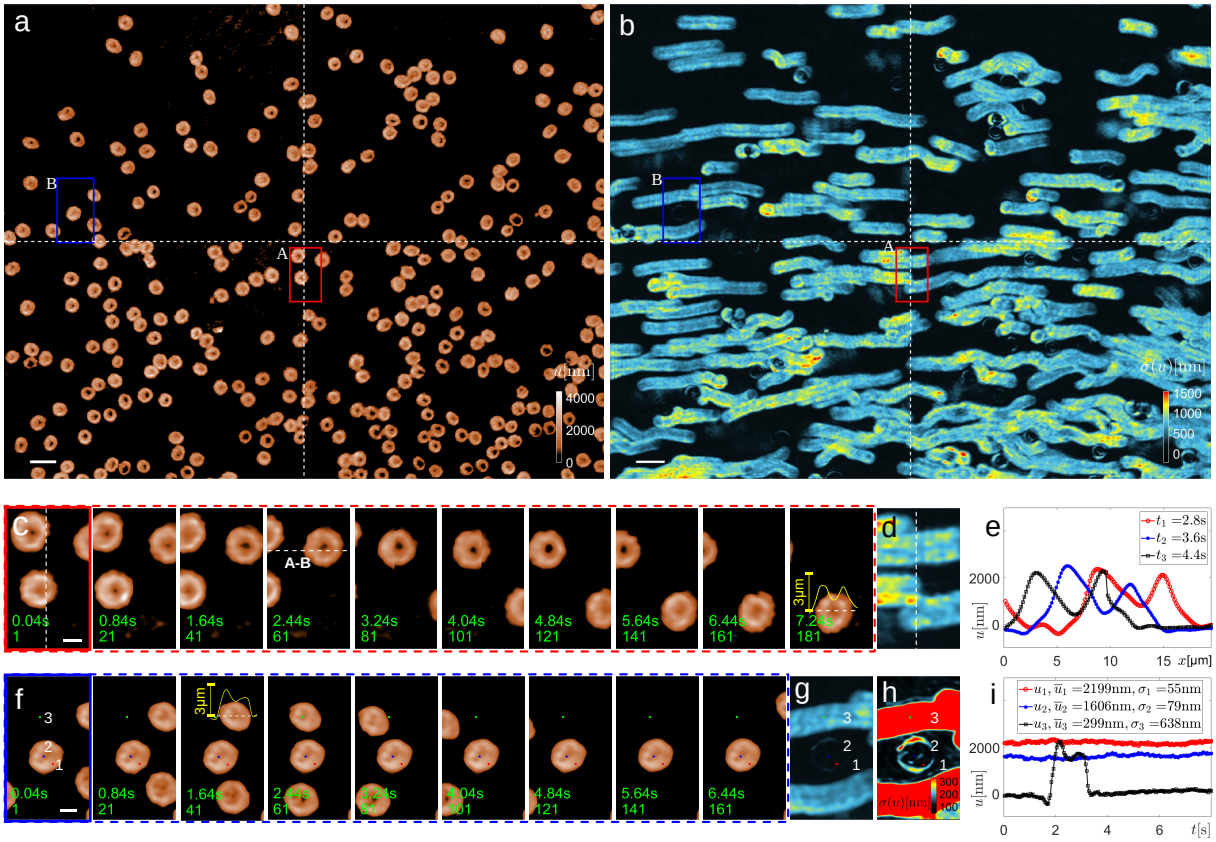

Figure 6.5: $4f$-MAIM video for quantifying subcellular dynamics of flowing erythrocytes at 25 Hz. (a) One frame from the full-FOV thickness (u) fluctuation video (Video S1). (b) Temporal standard deviations [$\sigma(u)$] of the full-FOV u fluctuations over 8 s at 0.04 s intervals. (c) Several frames of the zoomed-in video (Video S1, A) from the small box area A in (a) that spans variable FOV subsets. (d) The corresponding $\sigma(u)$ of (c). (e) u profiles along the dotted line A-B in (c) at 2.8 s, 3.6 s, and 4.4 s, respectively. (f) Several frames of the zoomed-in video (Video S1, B) from the small box area B in (a). (g) The corresponding $\sigma(u)$ of (f), and (h) the contrast-enhanced $\sigma(u)$ of (f). (i) Local u fluctuations at the three points indicated in (f)-(h). The respective average thicknesses $\bar{u}$ and standard deviations σ are indicated. Scale bars: (a), (b) 20 μm; (c), (f) 5 μm.

$\sigma(u)$ [Figure 6.5(b)] describe the time-averaged fluctuation amplitudes across the entire cell population, revealing the spatial and the temporal motion information such as flow tracks and instant local flow speeds of individual cells (a smaller average $\sigma(u)$ on the flow tracks represents a faster speed).

The magnified video from the box area A (Video S1, A), several frames of which are shown in Figure 6.5(c), and the corresponding zoomed-in $\sigma(u)$ [Figure 6.5(d)] show that both the measured static and the dynamic features of cells connect smoothly between the variable FOV subsets. The time-varying u profiles [Figure 6.5(e)] along the dotted line A-B [Figure 6.5(c)], which spans two FOV subsets, agree with the known shape of RBCs, as well as the measured u profile of another cell at 7.24 s [Figure 6.5(c)]. This video demonstrates the dynamic imaging performance of MAIM at the junctions between the FOV subsets.

The magnified video from the box area B (Video S1, B), several frames of which are in Figure 6.5(f), shows topographic and dynamic details of individual flowing cells at the subcellular level, such as cell membrane fluctuations and hemoglobin transportations within each individual cell. The corresponding zoomed-in $\sigma(u)$ [Figure 6.5(g)] shows the tracks of two flowing RBCs, indicating that the two cells flowed at a uniform speed. Furthermore, the contrast-enhanced $\sigma(u)$ [Figure 6.5(h)] of Figure 6.5(f) presents the subcellular deformations of a nonflowing cell, indicating that the nonflowing cell was more deformed at the edges near the tracks of the flowing cells than in the middle parts, due to the mechanical interactions between the cells and the solution. When there is no flow, $\sigma(u)$ of individual RBCs is inversely proportional to their stiffness maps, providing indications of the cell flexibility for cell detecting [139, 176]. Figure 6.5(i) shows the local u fluctuations at two points on the nonflowing cell and one point on a flow track. The single-point u fluctuation at point 3 (u_3) probes the thickness profile of a flowing RBC, which agrees with that measured from the single-frame image of the same cell at 1.64 s [Figure 6.5(f)], as well as the known shape of RBCs. This type of topographic imaging with the accuracy of tens to hundreds of nanometers is similar to atomic force microscopy (AFM), while it is non-invasive and provides wide-FOV images in a single shot, allowing quantification of ultrafast dynamics with high throughput.

6.2.4 $4f$-MAIM refractometry of unstained cancer tissue slices

Staining methods, such as hematoxylin and eosin (H&E) stain and fluorescence microscopy, are widely used and are the gold standard in pathology diagnostics. Although stains offer high-contrast imaging with molecular specificity, they are qualitative and can be affected by sample preparations. In contrast, QPI techniques reveal the morphological or the chemical properties of samples by measuring quantitative information of unstained

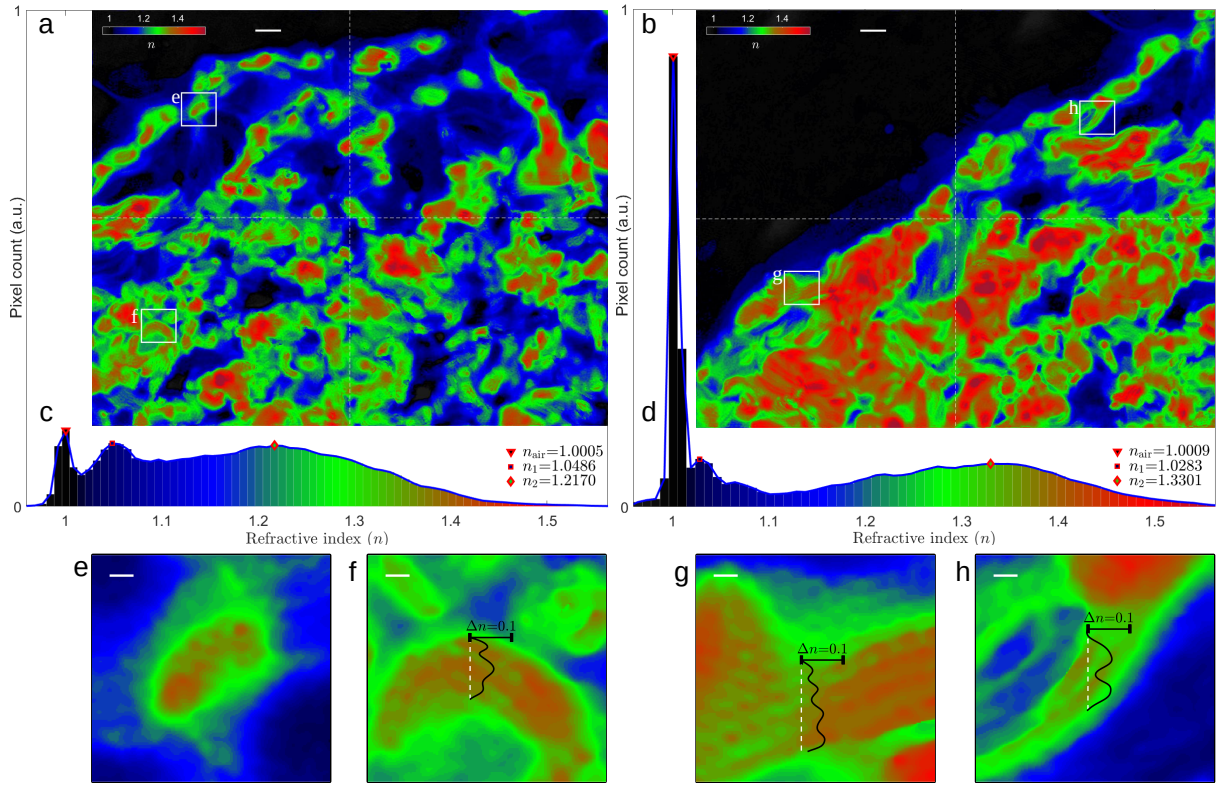

Figure 6.6: $4f$-MAIM refractometry of unstained cancer tissue (mouse pancreas). (a), (b) Full-FOV refractive index maps from two adjacent regions of the tissue slice, and (c), (d) the corresponding histograms. (e) Zoomed-in image of an individual cell from the box area (e) in (b). (f)-(h) Zoomed-in images of microfiber structures from the box areas (f)-(h) in (a) and (b), respectively. Scale bars: (a), (b) 20 μm; (e)-(h) 3 μm.

objects based on their optical properties [113, 177]. The quantitative information can also be utilized for virtual staining assisted by digital processing techniques such as deep neural networks [178]. In addition to saving time and costs associated with the labeling process, QPI also preserves tissues for subsequent diagnostic workflows such as molecular and genetic analysis. Here, we demonstrate high-SBP label-free tissue imaging capabilities of $4f$-MAIM by measuring the spatial distribution of the refractive index of an unstained cancer tissue slice from mouse pancreases. A 20× objective lens (0.4 NA) was adopted for imaging.

The full-FOV refractive index images [Figures 6.6(a) and (b), see Methods for the details of refractive index reconstruction] present the spatial distribution of various components of the tissue based on their refractive index signatures, revealing its overall biological structure with high resolution. Individual cells can be identified in the images due to their relatively higher refractive index [Figure 6.6(e)]. Fine structures such as microfibers can be observed in the zoomed-in images [Figures 6.6(f)-(h)]. To qualify the information contained in the wide-FOV refractive index images, we computed their statistical parameters via the respective histograms [Figures 6.6(c) and (d)]. Both the histograms are trimodal. The first peaks (∼1 refractive index) are from the background (air) and work as references. The second and the third peaks correspond to the refractive index information of two variable components from the tissue slice. The two histograms agree with each other in the peak locations, indicating that they contain similar biological components. The peak shifts show proportion changes among the variable tissue components within FOV by their refractive index signatures.

6.3 Discussion

We have demonstrated multibeam array interferometric microscopy (MAIM) for a single-shot high SBP. Our method overcomes the limitations of existing DHM techniques, increasing the SBP (FOV) by a maximum factor of 5, while maintaining the subnanometer optical path-length stability and the camera frame rate-limited temporal resolution. The theoretical fundamentals of MAIM were analyzed. The proof-of-concept imaging results of 5, 4, and $3f$-MAIM, the $4f$-MAIM video of live erythrocytes *in vitro*, and the $4f$-MAIM refractometry of unstained cancer tissue demonstrated the capabilities and the imaging performance of our method. This work opens up DHM to (ultra)fast or long-term (time-lapse) imaging of nanoscale dynamics in unstained live samples *in vitro* with high throughput. Our discussion has focused on the potential of the MAIM method.

The space-bandwidth efficiency can be defined by the available SBP per measurement with a given pixel amount [179]. Our prototype setup has not been optimized for extreme

space-bandwidth efficiency. The non-reconstructable FS components occupy a large part of the detector bandwidth. To achieve higher space-bandwidth efficiency, we eliminated the redundant FS components by increasing the diffraction angles and decreasing the transverse magnification factor M for more efficient use of the finite detector bandwidth (Figure 6.10). The space-bandwidth efficiency of the optimized $3f$-MAIM approached that of bright-field microscopy. Besides, the potential of MAIM for FOV enlargements are not fully exploited. The flexible 2D aperture array arrangements offer unique imaging capabilities. We believe two complementary 2D aperture arrays can be integrated by employing a beam splitter and a dual-channel architecture to collect more wavefronts simultaneously, e.g., $9f$-MAIM by combining a $4f$-MAIM and a $5f$-MAIM module with a certain space shift (Figure 6.11). Additionally, the maximum achievable SBP of MAIM can be potentially further increased by applying other alternative strategies, such as synthetic-aperture illumination [143, 144] and Kramers–Kronig imaging techniques [180].

Another consideration is the signal-to-noise ratio (SNR) reduction when multiplexing several wavefronts. The multiple single-frequency interferograms add linearly at the recording plane and thus share the limited dynamic range of gray-scale levels of the detector, resulting in a reduced SNR for each single-frequency interferogram. This issue can be addressed by using high-dynamic-range (HDR) detectors such as a 16-bit detector since the dynamic range increases significantly from 8-bit to 16-bit. From another perspective, the multiple interferograms also share the same pixel size. In this regard, MAIM can be considered as a conventional DHM with the $5\times$ pixel amount but the same pixel size, i.e., imaging without compromising the size-related imaging performance such as exposure time. Furthermore, even when using image sensors with pixel amounts that approach or exceed the SBP limit of objective lenses, MAIM can increase SNR and avoid aliasing and phase distortions via oversampling. Additionally, MAIM can increase recording speeds. For ultrahigh-speed imaging, a fundamental compromise exists between number of pixels (FOV) and frame rate, set by camera's data transfer rate. The effective number of pixels must be reduced in a process known as partial readout to achieve high frame rates. As an example, $4f$-MAIM can increase frame rates by employing 1/4 pixels (FOV) to achieve full-FOV imaging.

Although only the 3×3 beam array interference has been demonstrated, we envision that the MAIM utilizing higher-order diffraction beams is feasible, e.g., passing the diffraction orders $E_{-2,0}$ and $E_{+2,0}$ in the $3f$-MAIM setup [Figure 6.4(a)] achieves another implementation of $5f$-MAIM. Due to the twice-diffraction mechanism, the light efficiency of MAIM is usually an order of magnitude lower than that of the conventional DHM. The issue can be addressed by adopting high-power lasers or gratings with high light efficiency. Customized metasurfaces can be employed to further miniaturize the MAIM device and increase its

compactness and mechanical robustness [181]. Epi-illumination MAIM imaging should be achievable by adopting a reflection illumination [182, 183], as the MAIM module works as an add-on module and can be applied to most standard digital microscopes. The current method is a monochrome technique. When a multi-wavelength illumination is applied, the transmission beams $E_{0,0}$ propagate along the same straight path, and thus they can be low-pass spatial filtered simultaneously to generate the reference waves corresponding to different color channels. This feature allows the multi-wavelength MAIM implementations for simultaneous multi-modal or multispectral imaging [184–186].

Conventional holographic multiplexing devices usually require large space, mechanical stabilities, and precise optical alignments. The concept of multibeam array interference eliminates the hardware design challenges associated with conventional holographic multiplexing schemes, while providing high optical path-length stability. We believe this concept is potentially more broadly adaptable. Although this work specifically focuses on FOV multiplexing, we envision that this compact, robust and stable optical framework can facilitate imaging scheme designs of other types of holographic devices that require multiple wavefront recoveries, such as high-speed synthetic-aperture holographic microscopy [158] and high-speed holographic tomography [159].

6.4 Methods

Experimental Setup. In the current setup [Figure 6.1(f)], HNLS008R-EC (He-Ne laser, 632.8 nm, 0.8 mW, Thorlabs) was used for illumination, and DCC1545M (CMOS, 1280×1024, 5.2 μm pixel size, monochrome, 8-bit, $\leq$ 25 fps, Thorlabs) was used for capturing full-frame images. The lens L had a focal length of 100 mm. In Results, a pair of Ronchi gratings with a frequency of 40 c/mm was used to generate the diffraction beam array. A 10× objective lens (PLN, 0.25 NA, infinity-corrected, Olympus) was used for the proof-of-concept MAIM experiments, and a 20× objective lens (HI PLAN, EPI, 0.4 NA, infinity-corrected, Leica) was used for the $4f$-MAIM video of live erythrocytes and $4f$-MAIM label-free refractometry imaging of the cancer tissue sample. For the further space-bandwidth efficiency optimization of $3f$-MAIM (Figure 6.10), a pair of Ronchi gratings with a frequency of 50 c/mm was used to achieve higher frequency shifts.

MAIM image reconstruction. To achieve high-SBP imaging, firstly, a FOV calibration was performed to ensure proper space shifts among the multiple FOV subsets [Figure 6.7(a)]. Secondly, the complex amplitudes of the single-frequency interferograms were reconstructed from the respective FS components individually using FFT [46, 103]. The applied digital low-pass filters were circular pupils, given by the coherent transfer function of the objective lens. A reliability-guided fast 2D phase-unwrapping algorithm was applied

to unwrap the subset phase images [187]. Thirdly, FOV subsets stitching procedures and phase value alignments [Figure 6.7(b)] were performed to ensure a continuous FOV and continuous phase distributions of the synthetic images. Finally, we applied the same digital processing to sample-free interferograms [e.g., Figure 6.2(a)] and compensated for wavefront aberrations by subtraction [103, 132].

Sample preparation. For the proof-of-concept experiments, the glass microspheres (75 μm mean diameter, standard soda-lime, Sigma-Aldrich) were immersed in microscope immersion oil (1.515 refraction index) and sandwiched between coverslips with no additional preparation. To image live erythrocytes *in vitro*, droplets of blood were diluted with saline solution (0.9% NaCl) and sandwiched between coverslips. The saline solution was isotonic to RBCs and was used to keep the size and the shape of cells. The flow motions of the RBCs were driven by capillary actions. The cancer tissue slices (mouse pancreas) were prepared with the standard procedures of formalin fixation and paraffin embedding. The tissue samples were immersed in 4% Roti® Histofix for 24h and then were dehydrated in ASP300 (fully enclosed tissue processor, Leica). Paraffin was used to embed the tissue blocks at room temperature. The serial sections were cut at a thickness of ∼2.5 μm with HM355S (rotary microtome, Thermo Scientific) for phase imaging.

Thickness and refractive index reconstruction. The phase information of RBCs was transformed into thickness by using a refractive index contrast Δn of 0.045 between the hemoglobin contained in the cells and the surrounding solution:

$$u(\mathbf{r},t) = \lambda \cdot \varphi(\mathbf{r},t)/(2\pi\Delta n). \tag{6.6}$$

By the same principle, the phase information of the unstained tissue slice was transformed into refractive index (i.e., the integral of refractive index along a straight line in the direction of beam propagation) by calculating the refractive index contrast Δn between air and the tissue slice with a given thickness (2.5 μm).

6.5 Extended data

FOV calibration and phase alignment. The circle markers [Figure 6.7(a)] represent diffraction replicas of the sample image on the imaging plane, indicating the space shift of each FOV subset. The horizontal and the vertical components of $\vec{d}_{\mathrm{RP}}$ are constrained to match the detector size, ensuring no gaps or overlaps exist among the multiple FOV subsets. The phases from different FOV subsets are aligned by subtracting the mean values of a reference area (sample-free background region) corresponding to each subset [Figure

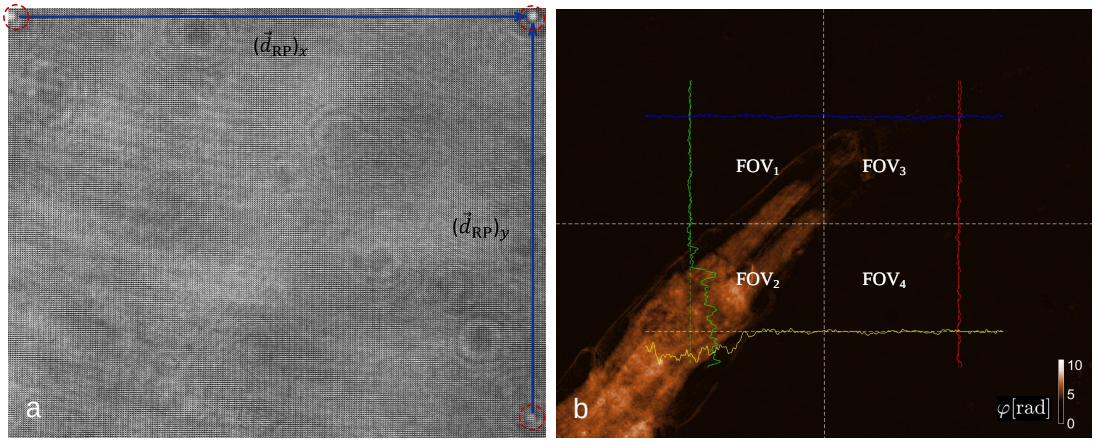

Figure 6.7: FOV calibration and phase alignment for synthesizing the multiple FOV subsets. (a) A spatially multiplexed interferogram for calibrating the space shifts of $4f$-MAIM. (b) The phase image of a *Daphnia* tail for the phase alignment of $4f$-MAIM.

6.7(b)]. The phase profiles spanning variable FOV subsets keep continuous, indicating that the phase images from different subsets are well aligned.

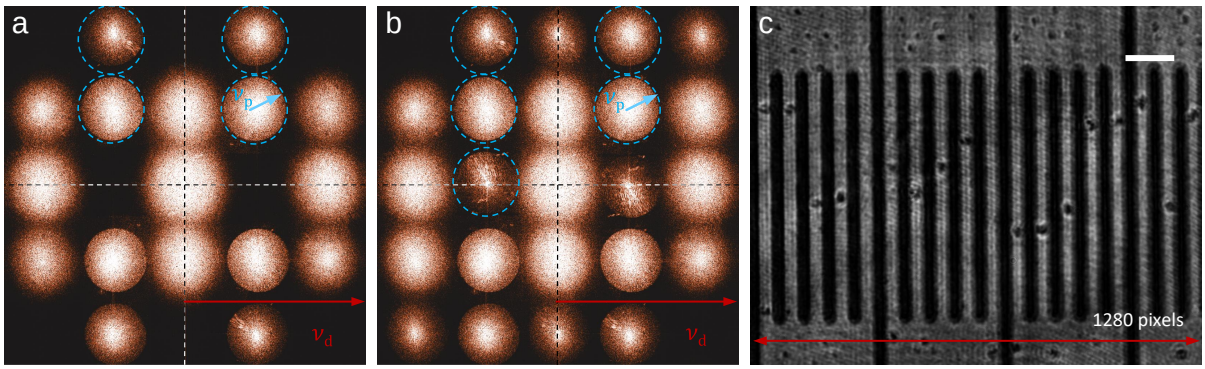

Figure 6.8: Resolution estimation of MAIM through frequency analysis. The FS component distributions of (a) $4f$- and (b) $5f$-MAIM. ν_d, the maximum sampling frequency given by the detectors. ν_d equals $1/(2S_{IP})$, where S_{IP} represents the imaging pixel size given by the magnification factor. ν_p, the maximum frequency given by the aperture function of the imaging system. (c) The calibration of S_{IP} with a calibration slide. Scale bar, 20 µm.

Resolution estimation. The resolution of the current setup was estimated using the frequency analysis method. A biological tissue slice was adopted for the estimation. As the sample has high-frequency microstructures that exceed the resolution limit of the current imaging system, the distribution of its FS components clearly illustrates the aperture function of the whole system [Figures 6.8 (a) and (b)]. To mark the aperture functions of the spatial filter for multibeam array interference, we adopted a customized 2D spatial

filter with rectangle apertures. The perfect circle shape of the FS components illustrates that the rectangular aperture functions caused by the customized spatial filter exceed the circle aperture function given by the objective lens. Additionally, we also estimated the resolution of the current imaging system by calibrating S_{IP} [Figure 6.8 (c)]. ν_{p} equals $\sim 1/6 \cdot \nu_{\mathrm{d}}$, corresponding to the resolution of $1/\nu_{\mathrm{p}} \approx 1.64$ µm. Under coherent illumination (632 nm), in which the illumination beam is parallel to the optical axis, the period of the smallest features observable with a microscope is given by $\lambda/\mathrm{NA}_{\mathrm{obj}} \approx 1.58$ µm. $1/\nu_{\mathrm{p}}$ is close to $\lambda/\mathrm{NA}_{\mathrm{obj}}$.

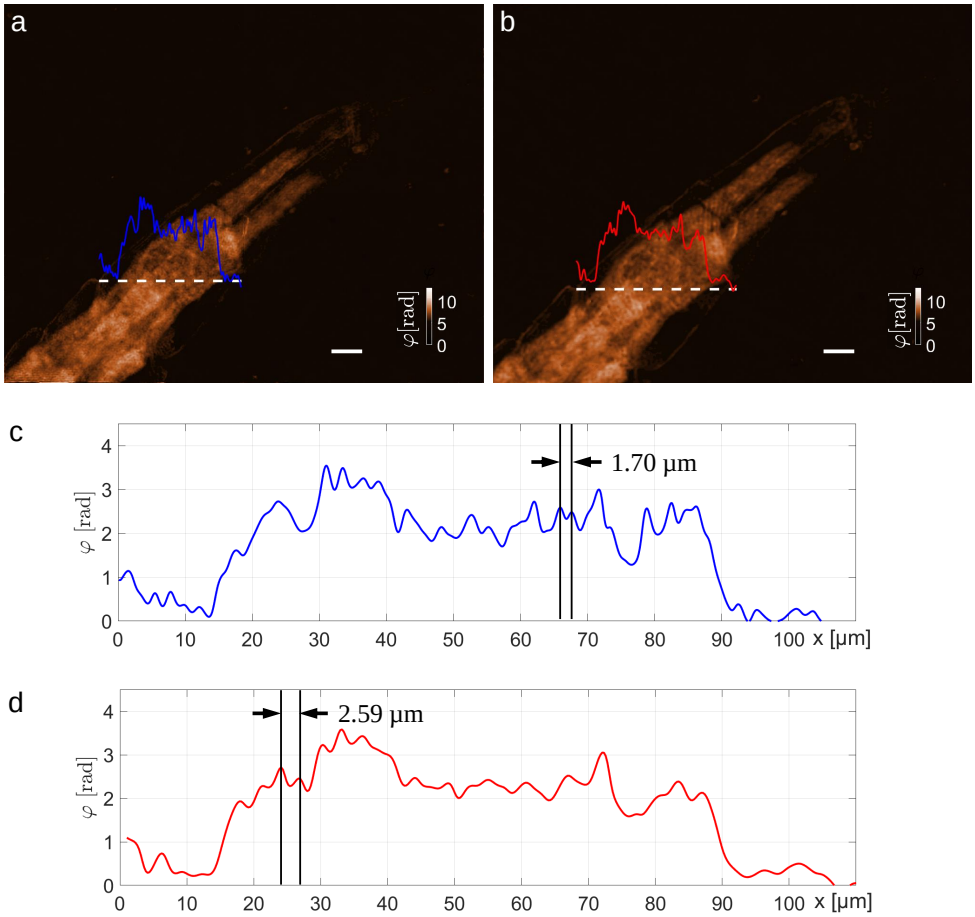

Figure 6.9: Experimental resolution analysis of $4f$-MAIM and the conventional DHM. The phase images of a *Daphnia* tail obtained with (a) the $4f$-MAIM prototype equipped with a 20× objective lens (0.4 NA) and (b) the conventional DHM equipped with a 10× objective lens (0.25 NA). (c), (d) The phase profiles along the dotted lines in (a) and (b) present the smallest observable periods of ∼1.70 µm and ∼2.59 µm, respectively. Scale bars, 20 µm.

The resolution limits of the current imaging system were also experimentally observed in the phase imaging experiment of a *Daphnia* tail. Although the two phase images

[Figures 6.9 (a) and (b)] show almost the same FOV, the image of $4f$-MAIM presents more details due to its higher NA. Both the smallest observable periods provided by $4f$-MAIM and the conventional DHM approach the corresponding theoretical coherent resolution limits ($\lambda/\mathrm{NA_{obj}}$), which equal ~1.58 µm and ~2.53 µm, respectively [Figures 6.9(c) and (d)]. Since the two methods provide images of the same FOV but MAIM presents higher resolution, it's can be concluded that MAIM increases the SBP by a factor of $\sim (\mathrm{NA_{MAIM}}/\mathrm{NA_{DHM}})^2$ as compared with the conventional DHM.

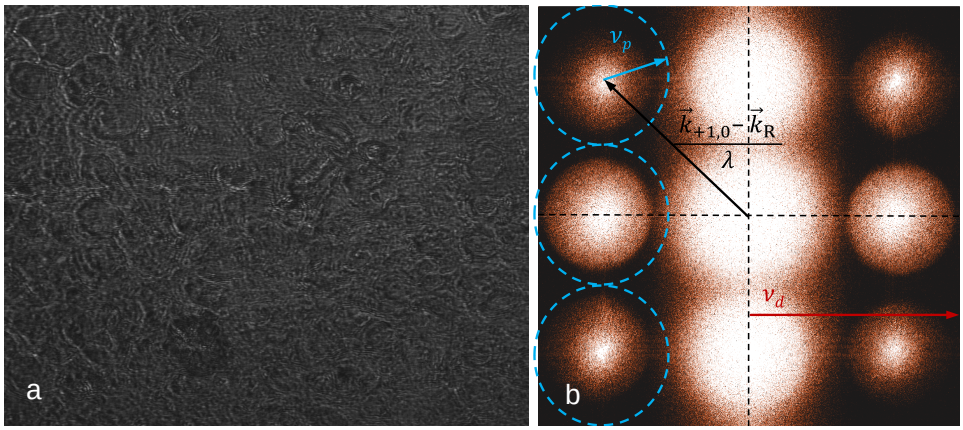

Figure 6.10: Quantifying the SPB of a spatial-bandwidth efficiency optimized $3f$-MAIM. (a) An interferogram of the unstained tissue slice obtained with the optimized $3f$-MAIM equipped with a 20× objective lens (0.4 NA), and (b) the corresponding Fourier spectrum, in which ν_p equals $\sim 1/3 \cdot \nu_\mathrm{d}$.

SPB optimization. The spatial-bandwidth efficiency of $3f$-MAIM was optimized by employing a pair of Ronchi gratings of a higher frequency (50 c/mm) and decreasing the distance d_3 (Figure 6.10). Since the optimized $3f$-MAIM provides 3 sub-FOVs, its SPB can be quantified by using Equation 2.31:

$$\mathcal{S}_{3f\text{-MAIM}} = 3 \cdot 2 \left(\frac{\nu_p}{\nu_d}\right)^2 \cdot \mathcal{S}_d = \frac{2}{3}\mathcal{S}_d. \tag{6.7}$$

The optimization strategy should also be applicable to $4/5f$-MAIM.

Design of $9f$-MAIM. Theoretically, $9f$-MAIM can be achieved by adopting a dual-channel scheme [Figure 6.11(a)], in which two complementary $4f$- and $5f$-MAIM modules capture wavefront subsets of objects without overlapping. More specifically, the $4f$-MAIM module captures the sample image with $\mathrm{FOV_{1-1}}$-$\mathrm{FOV_{1-4}}$, while the $5f$-MAIM module covers $\mathrm{FOV_{2-1}}$-$\mathrm{FOV_{2-5}}$ [Figure 6.11(b)]. By adopting the synchronous triggering procedure, quasi single-shot quantitative phase imaging with a large synthetic FOV consisting of 9 subsets should be possible via the dual-channel $9f$-MAIM.

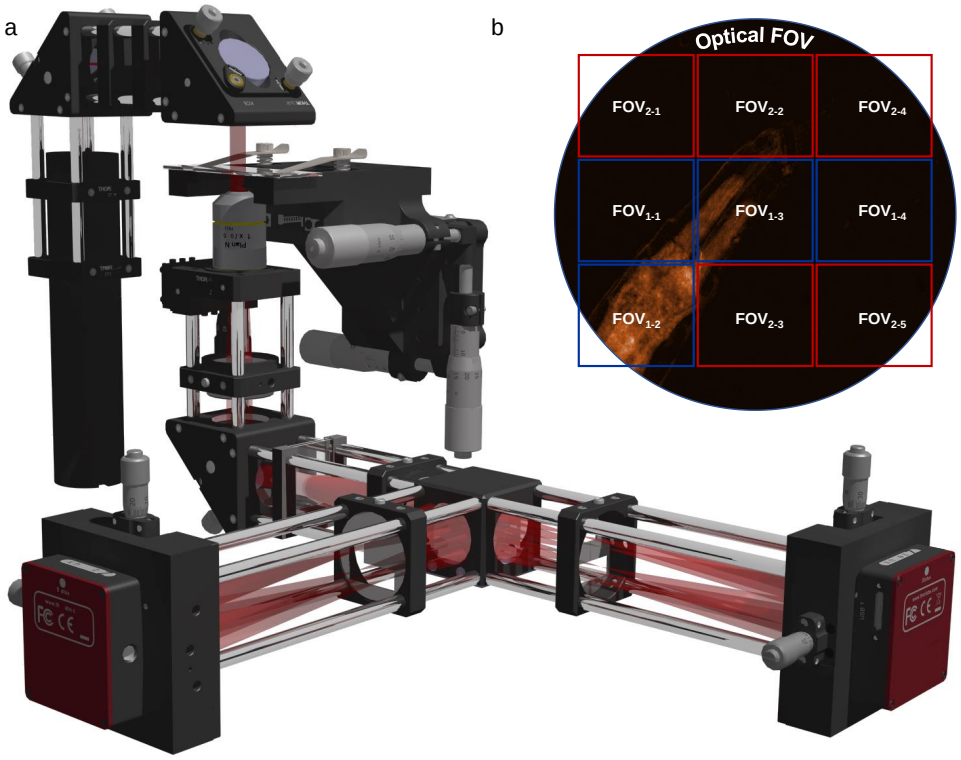

Figure 6.11: (a) Schematic of a possible implementation of dual-channel $9f$-MAIM, (b) the corresponding synthetic FOV.

Chapter 7

Conclusion

This thesis has explored several new common-path interferometric methods for single-shot quantitative phase imaging in two aspects: speckle interferometry for surface deformation measurements and holographic microscopy for label-free imaging of phase objects. Our own-developed methods provide phase imaging capabilities/performance previously unachievable while maintaining both high acquisition rates and high temporal phase stability. The key contributions are summarized as follows.

Simultaneous measurements of multiple deformation components have always been in demand, as deformations in nature and engineering are usually in 3D. Off-axis speckle interferometers of common-path geometry offer both high temporal resolution and high temporal phase stability. However, measuring multiple components is still challenging with such a configuration. To this end, for the first time to our knowledge, we developed a single-shot dual-sensitive image-shearing speckle interferometer by combining off-axis interferometry, common-path image shearing, and symmetric observation (Chapter 3). The capability of this common-path method to simultaneously measure in-plane and out-of-plane strain components was demonstrated through the measurements of crack-tip strain components in mode-I fracture experiments. This technique potentially allows industrial applications such as in-plane and out-of-plane dual-sensitive nondestructive testing.

Another drawback of the conventional common-path off-axis interferometric configuration lies in the limited minimal shear amount. In Chapter 4, we developed a single-shot image-shearing speckle interferometer with an unlimited minimal shearing amount by placing a Wollaston prism near the Fourier plane of a common-path quasi-4f imaging system. We analyzed the fundamentals of the shear amount and spatial carrier frequencies mathematically and validated the theoretical predictions via a static experiment. Its capability to

measure full-field strain distributions with various shear amounts was validated through mode-I fracture experiments of three-point bending. This method requires no tilt among the optical components, which significantly increases the robustness of the interferometric system and simplifies the optical alignment.

Common-path off-axis holographic microscopy enables true complex-field reconstruction with high phase stability from a single hologram, but it also suffers the phase aberration problem. In Chapter 5, we developed a low-pass filtering compensation (LPFC) method to compensate for wavefront aberrations in a point-diffraction common-path digital holographic microscope. This method estimates phase aberrations from a single object hologram by Fourier transform and low-pass spatial filtering. We demonstrated that for a digital holographic microscopy system with relatively high-frequency objects and low-frequency phase aberrations, the developed method allowed phase compensation for both smooth objects and objects containing abrupt edges. As this method requires no numerical fitting procedures, iterative steps, or prior knowledge of optical parameters, it substantially simplifies the process of phase compensation in digital holographic microscopy.

While off-axis holography achieves high acquisition rates, it has been troubled by the SBP problem ever since its invention by Leith and Upatnieks, which significantly limits the performance of modern off-axis digital holographic microscopy devices. In Chapter 6, we developed a high-throughput common-path phase imaging method termed multibeam array interferometric microscopy (MAIM). For the first time to our knowledge, this method overcomes the limitations of conventional off-axis DHM techniques, increasing the SBP (FOV) by a maximum factor of 5, while maintaining the subnanometer optical path-length stability. We analyzed the theoretical fundamentals and built the MAIM prototypes to increase the FOV by factors of 5, 4, and 3, respectively. The proof-of-concept imaging experiments on both natural and artificial samples proved the feasibility and the imaging capability of MAIM. Additionally, we also applied MAIM for biomedical imaging applications, including monitoring subcellular dynamical phenomena in flowing live erythrocytes *in vitro* and label-free micro-refractometry imaging of unstained cancer tissue slices. MAIM potentially enables (ultra)fast or long-term (time-lapse) high-throughput imaging of nanoscale dynamics of unstained live samples *in vitro*.

Acknowledgments

First and foremost, I would like to express my deepest gratitude to my doctoral advisor, Prof. Dr.-Ing. habil. Dr. h.c. Alexander W. Koch, for believing in me from the start and giving me such a wonderful chance to pursue my Ph.D degree, for creating a truly academic environment, and for his always insightful suggestions.

My special thanks go to Dr.-Ing. Martin Jakobi, for his always timely support and diligent scientific help. I am also grateful to Prof. Ali K. Yetisen of Imperial College London for his insightful academic advice, inspirations, warm encouragement, and for correcting my bad English. I express my appreciation to Prof. Zhanwei Liu of Beijing institute of technology, who was also my master advisor, for his precious advice and generous help for both my research and my career. I would like to thank Prof. Félix Salazar-Bloise of Technical University of Madrid for the helpful discussions on the scientific parts of my doctoral research. I also thank Prof. Dieter Saur of TranslaTUM for his generous help with my experiments.

I have learned something from all the Speckle group members of MST, Dr.-Ing Min Lu, Dr.-Ing Laura Bilgeri, Dr.-Ing Shengjia Wang, and Franziska Brändle. I greatly appreciate their contributions and cooperation in the daily laboratory section. I also had great pleasure of working with all the other friends and colleagues at MST and ESM, Xingchen Dong, Dr.-Ing. Marcel Hoffmann, Dr.-Ing. Moritz A. Graf, Dr.-Ing. Michael Köhler, Patrick Kienle, Kun Wang, Wolfgang Kurz, Qiang Bian, Xiao Bi, and Xinxu Zhao. I thank all the students who have worked under my supervision at MST. I greatly thank Chen Zhao of TranslaTUM for providing me with tissue samples and the knowledge of biology.

Specific recognition goes to Ms. Rita von Grafenstein for her perfect arrangement of my work at MST and for her professional and responsible working attitude. I thank Mr. Bernhard Obermaier for his support in the preparation of mechanical components in my experimental setup. I thank Mr. Zbigniew Poplawski for his IT support.

At the end, my warmest thoughts go to my princess Xinyi for her priceless company and unfailing patience. I am deeply grateful to my family for giving me the great opportunity to study for such a long time and making me feel supported all the time. I thank my friends Ivan, Veronica, and Isabella for making my life fun in Germany.

List of Symbols

Here we define the global symbols which are used throughout the whole thesis. The local symbols are explained in the respective contexts.

C	conjugate or cross-section term
D	direct current term
d	distance
F	Fresnel number
f_s	transmission function
I	intensity
J_0	the zero-order Bessel function
J_1	the first-order Bessel function
k_0	angular wavenumber
M	optical magnification factor
r_x, r_y	coordinates in sapce
t_x, t_y	coordinates in sapce
z	coordinate along the z-axis

α	angle
ε_0	vacuum permittivity
ε_r	relative permittivity
θ	angle
λ	wavelength
μ_0	vacuum permeability
μ_r	relative permeability
ν_C	frequency of conjugate terms
ν_D	frequency of direct current terms
ν_d	sampling frequency
ξ	variable in the frequency domain

ρ	radius
τ	variable in time or space
ϕ	angle
φ	phase
ω	angular frequency

$\mathbf{E}$	electric field
$\mathbf{e}_x, \mathbf{e}_y$	unit vector along the x- and y-axis
$\mathbf{H}$	magnetic field
$\mathbf{J}$	normalized Jones vector
$\mathbf{k}$	coordinate vector in the frequency domain
$\mathbf{r}$	coordinate vector in sapce
$\mathbf{S}$	Poynting (Umov-Poynting) vector
$\mathbf{t}$	coordinate vector in sapce
$\mathbf{U}$	vector field of electromagnetic radiation
$\mathbf{z}_0$	unit vector along the z-axis
$\boldsymbol{\nu}$	vector of carrier frequency
$\boldsymbol{\psi}_\mathrm{i}$	complex field of two-beam interference
$\vec{d}$	vector of surface displacements
$\vec{k}_i$	wavevector of illumination
$\vec{k}_j$	wavevector
$\vec{k}_o$	wavevector of observation

$\widetilde{f}$	Fourier transform of f
$\mathrm{p} \cdot \mathrm{v}$	Cauchy principal value
$\mathbb{R}$	real number
sgn	sign function
$\mathcal{C}$	intensity contrast
$\mathcal{S}$	space-bandwidth product
$\mathcal{S}_d$	space-bandwidth product of the detector
arg	complex argument operator
$\mathcal{F}$	Fourier operator
$\mathcal{H}$	Hilbert operator
∇	divergence operator
$\circledast$	convolution operator

List of Abbreviations

CDI	coherent diffractive imaging
CMOS	complementary metal-oxide semiconductor
CNN	convolutional neural network
DC	direct current
DEC	double-exposure compensation
DHM	digital holographic microscopy
DOV	depth of view
EMD	empirical mode decomposition
FFT	fast Fourier transform
FOV	field of view
FP	Fourier plane or focal plane
FS	Fourier space
GPU	graphics processing unit
HDR	high-dynamic-range
HHT	Hilbert-Huang transform
IMF	intrinsic mode function
IP	imaging plane
LIGO	laser interferometer gravitational-wave observatory
LPFC	low pass filtering compensation
MAIM	multibeam array interferometric microscopy
MO	microscope objective
MTF	modulation transfer function
NA	numerical aperture
NDT	non-destructive testing
OGM	orthogonal grating modulation
OPD	optical path difference
OTF	optical transfer function
PALM	fluorescence photoactivation localization microscopy
PCM	phase contrast microscopy

PDI point diffraction interferometer
PhTF phase transfer function
PMMA polymethyl methacrylate
PSF point spread function
QPI quantitative phase imaging
RBC red blood cell
SBP space-bandwidth product
SIM structured illumination microscopy
SNR signal-to-noise ratio
STED stimulated emission depletion
STORM stochastic optical reconstruction microscopy
TIE transport-of-intensity equation

List of Figures

Bibliography

[1] A. Snigirev, I. Snigireva, V. Kohn, S. Kuznetsov, and I. Schelokov. "On the possibilities of x-ray phase contrast microimaging by coherent high-energy synchrotron radiation". In: *Review of Scientific Instruments* 66.12 (1995), pp. 5486–5492.

[2] K. Creath. "V phase-measurement interferometry techniques". In: *Progress in optics*. Vol. 26. Elsevier, 1988, pp. 349–393.

[3] Y. Shechtman, Y. C. Eldar, O. Cohen, H. N. Chapman, J. Miao, and M. Segev. "Phase retrieval with application to optical imaging: a contemporary overview". In: *IEEE Signal Processing Magazine* 32.3 (2015), pp. 87–109.

[4] J. Miao, P. Charalambous, J. Kirz, and D. Sayre. "Extending the methodology of X-ray crystallography to allow imaging of micrometre-sized non-crystalline specimens". In: *Nature* 400.6742 (1999), pp. 342–344.

[5] D. Gabor. "A new microscopic principle". In: *Nature* 161 (1948), pp. 777–778.

[6] E. Cuche, F. Bevilacqua, and C. Depeursinge. "Digital holography for quantitative phase-contrast imaging". In: *Optics Letters* 24.5 (1999), pp. 291–293.

[7] Y. Hung. "Shearography: a new optical method for strain measurement and nondestructive testing". In: *Optical Engineering* 21.3 (1982), p. 213391.

[8] P. Hariharan. *Basics of interferometry*. Elsevier, 2010.

[9] J. Leendertz. "Interferometric displacement measurement on scattering surfaces utilizing speckle effect". In: *Journal of Physics E: Scientific Instruments* 3.3 (1970), p. 214.

[10] J. Leendertz and J. Butters. "An image-shearing speckle-pattern interferometer for measuring bending moments". In: *Journal of Physics E: Scientific Instruments* 6.11 (1973), p. 1107.

[11] A. Abramovici, W. E. Althouse, R. W. Drever, Y. Gürsel, S. Kawamura, F. J. Raab, D. Shoemaker, L. Sievers, R. E. Spero, K. S. Thorne, et al. "LIGO: The laser interferometer gravitational-wave observatory". In: *Science* 256.5055 (1992), pp. 325–333.

[12] B. C. Platt and R. Shack. "History and principles of Shack-Hartmann wavefront sensing". In: *Journal of refractive surgery* 17.5 (2001), S573–S577.

[13] P. Mercère, P. Zeitoun, M. Idir, S. Le Pape, D. Douillet, X. Levecq, G. Dovillaire, S. Bucourt, K. A. Goldberg, P. P. Naulleau, et al. "Hartmann wave-front measurement at 13.4 nm with $\lambda_{EUV}/120$ accuracy". In: *Optics Letters* 28.17 (2003), pp. 1534–1536.

[14] M. R. Teague. "Irradiance moments: their propagation and use for unique retrieval of phase". In: *JOSA* 72.9 (1982), pp. 1199–1209.

[15] A. Roberts, K. Thorn, M. L. Michna, N. Dragomir, P. Farrell, and G. Baxter. "Determination of bending-induced strain in optical fibers by use of quantitative phase imaging". In: *Optics Letters* 27.2 (2002), pp. 86–88.

[16] D. Sayre. "Some implications of a theorem due to Shannon". In: *Acta Crystallographica* 5.6 (1952), pp. 843–843.

[17] R. W. Gerchberg. "A practical algorithm for the determination of phase from image and diffraction plane pictures". In: *Optik* 35 (1972), pp. 237–246.

[18] W. L. Bragg. "The structure of some crystals as indicated by their diffraction of X-rays". In: *Proceedings of the Royal Society of London. Series A, Containing papers of a mathematical and physical character* 89.610 (1913), pp. 248–277.

[19] F. Zernike. "Diffraction theory of the knife-edge test and its improved form, the phase-contrast method". In: *Monthly Notices of the Royal Astronomical Society* 94 (1934), pp. 377–384.

[20] E. N. Leith and J. Upatnieks. "Wavefront reconstruction with continuous-tone objects". In: *JOSA* 53.12 (1963), pp. 1377–1381.

[21] D. Paganin and K. A. Nugent. "Noninterferometric phase imaging with partially coherent light". In: *Physical Review Letters* 80.12 (1998), p. 2586.

[22] K. A. Nugent, T. E. Gureyev, D. F. Cookson, D. Paganin, and Z. N. Barnea. "Quantitative phase imaging using hard x rays". In: *Physical Review Letters* 77.14 (1996), p. 2961.

[23] J. Zuo, I. Vartanyants, M. Gao, R. Zhang, and L. A. Nagahara. "Atomic resolution imaging of a carbon nanotube from diffraction intensities". In: *Science* 300.5624 (2003), pp. 1419–1421.

[24] P. Thibault, M. Dierolf, A. Menzel, O. Bunk, C. David, and F. Pfeiffer. "High-resolution scanning x-ray diffraction microscopy". In: *Science* 321.5887 (2008), pp. 379–382.

[25] F. Pfeiffer. "X-ray ptychography". In: *Nature Photonics* 12.1 (2018), pp. 9–17.

[26] Y. Jiang, Z. Chen, Y. Han, P. Deb, H. Gao, S. Xie, P. Purohit, M. W. Tate, J. Park, S. M. Gruner, et al. "Electron ptychography of 2D materials to deep sub-ångström resolution". In: *Nature* 559.7714 (2018), pp. 343–349.

[27] U. Neuhäusler, G. Schneider, W. Ludwig, M. A. Meyer, E. Zschech, and D. Hambach. "X-ray microscopy in Zernike phase contrast mode at 4 keV photon energy with 60 nm resolution". In: *Journal of Physics D: Applied Physics* 36.10A (2003), A79.

[28] C. David, B. Nöhammer, H. Solak, and E. Ziegler. "Differential x-ray phase contrast imaging using a shearing interferometer". In: *Applied Physics Letters* 81.17 (2002), pp. 3287–3289.

[29] J. Rodenburg, A. Hurst, and A. Cullis. "Transmission microscopy without lenses for objects of unlimited size". In: *Ultramicroscopy* 107.2-3 (2007), pp. 227–231.

[30] G. Zheng, R. Horstmeyer, and C. Yang. "Wide-field, high-resolution Fourier ptychographic microscopy". In: *Nature Photonics* 7.9 (2013), pp. 739–745.

[31] E. N. Leith and J. Upatnieks. "Reconstructed wavefronts and communication theory". In: *JOSA* 52.10 (1962), pp. 1123–1130.

[32] E. N. Leith and J. Upatnieks. "Wavefront reconstruction with diffused illumination and three-dimensional objects". In: *JOSA* 54.11 (1964), pp. 1295–1301.

[33] R. L. Powell and K. A. Stetson. "Interferometric vibration analysis by wavefront reconstruction". In: *JOSA* 55.12 (1965), pp. 1593–1598.

[34] J. Dyson. "An interferometer microscope". In: *Proceedings of the Royal Society of London. Series A. Mathematical and Physical Sciences* 204.1077 (1950), pp. 170–187.

[35] E. N. Leith, J. Upatnieks, and K. A. Haines. "Microscopy by wavefront reconstruction". In: *JOSA* 55.8 (1965), pp. 981–986.

[36] D. Gabor and W. Goss. "Interference microscope with total wavefront reconstruction". In: *JOSA* 56.7 (1966), pp. 849–858.

[37] G. W. Ellis. "Holomicrography: transformation of image during reconstruction a posteriori". In: *Science* 154.3753 (1966), pp. 1195–1197.

[38] R. F. Vanligten and H. Osterberg. "Holographic microscopy". In: *Nature* 211.5046 (1966), pp. 282–283.

[39] E. Cuche, P. Marquet, and C. Depeursinge. "Simultaneous amplitude-contrast and quantitative phase-contrast microscopy by numerical reconstruction of Fresnel off-axis holograms". In: *Applied Optics* 38.34 (1999), pp. 6994–7001.

[40] J. H. Bruning, D. R. Herriott, J. Gallagher, D. Rosenfeld, A. White, and D. Brangaccio. "Digital wavefront measuring interferometer for testing optical surfaces and lenses". In: *Applied Optics* 13.11 (1974), pp. 2693–2703.

[41] P. Hariharan, B. F. Oreb, and N. Brown. "A digital phase-measurement system for real-time holographic interferometry". In: *Optics Communications* 41.6 (1982), pp. 393–396.

[42] K. Creath. "Phase-shifting speckle interferometry". In: *Applied Optics* 24.18 (1985), pp. 3053–3058.

[43] I. Yamaguchi, T. Matsumura, and J. Kato. "Phase-shifting color digital holography". In: *Optics Letters* 27.13 (2002), pp. 1108–1110.

[44] S. Almazan-Cuellar and D. Malacara-Hernandez. "Two-step phase-shifting algorithm". In: *Optical Engineering* 42.12 (2003), pp. 3524–3531.

[45] X. Meng, L. Cai, X. Xu, X. Yang, X. Shen, G. Dong, and Y. Wang. "Two-step phase-shifting interferometry and its application in image encryption". In: *Optics Letters* 31.10 (2006), pp. 1414–1416.

[46] M. Takeda, H. Ina, and S. Kobayashi. "Fourier-transform method of fringe-pattern analysis for computer-based topography and interferometry". In: *JOSA* 72.1 (1982), pp. 156–160.

[47] M. Takeda and K. Mutoh. "Fourier transform profilometry for the automatic measurement of 3-D object shapes". In: *Applied Optics* 22.24 (1983), pp. 3977–3982.

[48] A. A. Michelson and E. W. Morley. "On the relative motion of the earth and of the luminiferous ether". In: *Sidereal Messenger* 6 (1887), pp. 306–310.

[49] G. Nomarski. "Nouveau dispositif pour lobservation en contraste de phase differentiel". In: *Journal de Physique et le Radium*. Vol. 16. 1955, S88.

[50] R. Allen and G. David. "The Zeiss-Nomarski differential interference equipment for transmitted-light microscopy". In: *Zeitschrift fur wissenschaftliche Mikroskopie und mikroskopische Technik* 69.4 (1969), pp. 193–221.

[51] J. Dyson. "Common-path interferometer for testing purposes". In: *JOSA* 47.5 (1957), pp. 386–390.

[52] Y. Y. Hung and C. E. Taylor. "Speckle-shearing interferometric camera–a tool for measurement of derivatives of surface-displacement". In: *Developments in Laser Technology II*. Vol. 41. International Society for Optics and Photonics. 1974, pp. 169–176.

[53] G. Popescu, L. P. Deflores, J. C. Vaughan, K. Badizadegan, H. Iwai, R. R. Dasari, and M. S. Feld. "Fourier phase microscopy for investigation of biological structures and dynamics". In: *Optics Letters* 29.21 (2004), pp. 2503–2505.

[54] M. Born and E. Wolf. *Principles of optics: electromagnetic theory of propagation, interference and diffraction of light*. Elsevier, 2013.

[55] J. W. Goodman. *Introduction to Fourier optics*. Roberts and Company, 2005.

[56] K. Shin and J. Hammond. *Fundamentals of signal processing for sound and vibration engineers*. John Wiley & Sons, 2008.

[57] G. K. Ackermann and J. Eichler. *Holography: a practical approach*. John Wiley & Sons, 2007.

[58] A. Lipson, S. G. Lipson, and H. Lipson. *Optical physics*. Cambridge University Press, 2010.

[59] N. E. Huang. *Hilbert-Huang transform and its applications*. World Scientific, 2014.

[60] G. B. Airy. "On the diffraction of an object-glass with circular aperture". In: *Transactions of the Cambridge Philosophical Society* 5 (1835), p. 283.

[61] E. Abbe. "Beiträge zur Theorie des Mikroskops und der mikroskopischen Wahrnehmung". In: *Archiv für mikroskopische Anatomie* 9.1 (1873), pp. 413–468.

[62] D. B. Murphy. *Fundamentals of light microscopy and electronic imaging*. John Wiley & Sons, 2002.

[63] L. Rayleigh. "XXXI. Investigations in optics, with special reference to the spectroscope". In: *The London, Edinburgh, and Dublin Philosophical Magazine and Journal of Science* 8.49 (1879), pp. 261–274.

[64] M. G. Gustafsson. "Surpassing the lateral resolution limit by a factor of two using structured illumination microscopy". In: *Journal of Microscopy* 198.2 (2000), pp. 82–87.

[65] S. W. Hell and J. Wichmann. "Breaking the diffraction resolution limit by stimulated emission: stimulated-emission-depletion fluorescence microscopy". In: *Optics Letters* 19.11 (1994), pp. 780–782.

[66] S. T. Hess, T. P. Girirajan, and M. D. Mason. "Ultra-high resolution imaging by fluorescence photoactivation localization microscopy". In: *Biophysical journal* 91.11 (2006), pp. 4258–4272.

[67] M. J. Rust, M. Bates, and X. Zhuang. "Sub-diffraction-limit imaging by stochastic optical reconstruction microscopy (STORM)". In: *Nature Methods* 3.10 (2006), pp. 793–796.

[68] J. W. Lichtman and J. Conchello. “Fluorescence microscopy”. In: *Nature Methods* 2.12 (2005), pp. 910–919.

[69] E. Abbe. “Ueber einen neuen Beleuchtungsapparat am Mikroskop”. In: *Archiv für mikroskopische Anatomie* 9.1 (1873), p. 1873.

[70] C. M. Sparrow. “On spectroscopic resolving power”. In: *The Astrophysical Journal* 44 (1916), p. 76.

[71] P. M. Duffieux. “L’intégrale de Fourier et ses applications à l’optique”. In: *Rennes* (1946).

[72] J. G. McNally, T. Karpova, J. Cooper, and J. A. Conchello. “Three-dimensional imaging by deconvolution microscopy”. In: *Methods* 19.3 (1999), pp. 373–385.

[73] P. Sarder and A. Nehorai. “Deconvolution methods for 3-D fluorescence microscopy images”. In: *IEEE Signal Processing Magazine* 23.3 (2006), pp. 32–45.

[74] J. Dong, S. Wang, M. Lu, M. Jakobi, Z. Liu, X. Dong, F. Pöller, L. M. Bilgeri, F. Salazar-Bloise, A. K. Yetisen, and A. W. Koch. “Real-time dual-sensitive shearography for simultaneous in-plane and out-of-plane strain measurements”. In: *Optics Express* 27.3 (2019), pp. 3276–3283.

[75] H. M. Shang, Y. Hung, W. Luo, and F. Chen. “Surface profiling using shearography”. In: *Optical Engineering* 39.1 (2000), pp. 23–32.

[76] I. Yamaguchi, J. Kato, and S. Ohta. “Surface shape measurement by phase-shifting digital holography”. In: *Optical Review* 8.2 (2001), pp. 85–89.

[77] U. P. Kumar, B. Bhaduri, M. P. Kothiyal, and N. K. Mohan. “Two-wavelength micro-interferometry for 3-D surface profiling”. In: *Optics and Lasers in Engineering* 47.2 (2009), pp. 223–229.

[78] L. M. Bilgeri, F. Salazar-Bloise, M. Lu, S. Wang, M. Jakobi, and A. W. Koch. “Intensity distortions due to phase-only spatial light modulation: Characterization for applications in electronic speckle-pattern interferometry”. In: *Review of Scientific Instruments* 89.8 (2018), p. 083701.

[79] N. Werth, F. Salazar-Bloise, and A. W. Koch. “Influence of roughness in the phase-shifting speckle method: an experimental study with applications”. In: *Review of Scientific Instruments* 85.1 (2014), p. 015114.

[80] J. Butters and J. Leendertz. “Speckle pattern and holographic techniques in engineering metrology”. In: *Optics and Lasers in Engineering* 3.1 (1971), pp. 26–30.

[81] A. W. Koch, M. W. Ruprecht, O. Toedter, and G. Häusler. *Optische messtechnik an technischen oberflächen*. Expert-Verlag: Renningen-Malmsheim, Germany, 1998.

[82] Y. Hung and C. Liang. “Image-shearing camera for direct measurement of surface strains”. In: *Applied Optics* 18.7 (1979), pp. 1046–1051.

[83] B. Bhaduri, M. Kothiyal, and N. K. Mohan. “Curvature measurement using three-aperture digital shearography and fast Fourier transform”. In: *Optics and Lasers in Engineering* 45.10 (2007), pp. 1001–1004.

[84] M. Lu, S. Wang, L. Aulbach, and A. W. Koch. “Simultaneous displacement and slope measurement in electronic speckle pattern interferometry using adjustable aperture multiplexing”. In: *Applied Optics* 55.22 (2016), pp. 5868–5875.

[85] M. Lu, S. Wang, L. Bilgeri, X. Song, M. Jakobi, and A. W. Koch. “Online 3D displacement measurement using speckle interferometer with a single illumination-detection path”. In: *Sensors (Basel, Switzerland)* 18.6 (2018), p. 1923.

[86] L. Yang, W. Steinchen, M. Schuth, and G. Kupfer. “Precision measurement and nondestructive testing by means of digital phase shifting speckle pattern and speckle pattern shearing interferometry”. In: *Measurement* 16.3 (1995), pp. 149–160.

[87] B. Bhaduri, N. K. Mohan, and M. Kothiyal. “A dual-function ESPI system for the measurement of out-of-plane displacement and slope”. In: *Optics and Lasers in Engineering* 44.6 (2006), pp. 637–644.

[88] H. V. Tippur. “Simultaneous and real-time measurement of slope and curvature fringes in thin structures using shearing interferometery”. In: *Optical Engineering* 43.12 (2004), pp. 3014–3021.

[89] D. Sharma, R. Sirohi, and M. P. Kothiyal. “Simultaneous measurement of slope and curvature with a three-aperture speckle shearing interferometer”. In: *Applied Optics* 23.10 (1984), pp. 1542–1546.

[90] K. Patorski and A. G. Olszak. “Digital in-plane electronic speckle pattern shearing interferometry”. In: *Optical Engineering* 36.7 (1997), pp. 2010–2016.

[91] G. Pedrini, Y. Zou, and H. J. Tiziani. “Simultaneous quantitative evaluation of in-plane and out-of-plane deformations by use of a multidirectional spatial carrier”. In: *Applied Optics* 36.4 (1997), pp. 786–792.

[92] P. Picart, E. Moisson, and D. Mounier. “Twin-sensitivity measurement by spatial multiplexing of digitally recorded holograms”. In: *Applied Optics* 42.11 (2003), pp. 1947–1957.

[93] M. Mello, S. Hong, and A. J. Rosakis. “Extension of the coherent gradient sensor (CGS) to the combined measurement of in-plane and out-of-plane displacement field gradients”. In: *Experimental Mechanics* 49.2 (2009), pp. 277–289.

[94] M. Mello and A. J. Rosakis. *Surface characterization based on lateral shearing of diffracted wave fronts to measure in-plane and out-of-plane displacement gradient fields*. US Patent 7,538,891. 2009.

[95] D. Francis, S. W. James, and R. P. Tatam. "Surface strain measurement using multi-component shearography with coherent fibre-optic imaging bundles". In: *Measurement Science and Technology* 18.11 (2007), pp. 3583–3591.

[96] S. Wang, M. Lu, L. M. Bilgeri, M. Jakobi, F. Salazar-Bloise, and A. W. Koch. "Temporal electronic speckle pattern interferometry for real-time in-plane rotation analysis". In: *Optics Express* 26.7 (2018), pp. 8744–8755.

[97] M. Lu, S. Wang, L. Aulbach, M. Jakobi, and A. W. Koch. "Non-phase unwrapping interferometric approach for a real-time in-plane rotation measurement". In: *Optics Letters* 42.10 (2017), pp. 1986–1989.

[98] Y. Hung and J. Wang. "Dual-beam phase shift shearography for measurement of in-plane strains". In: *Optics and Lasers in Engineering* 24.5-6 (1996), pp. 403–413.

[99] X. Xie, X. Chen, J. Li, Y. Wang, and L. Yang. "Measurement of in-plane strain with dual beam spatial phase-shift digital shearography". In: *Measurement Science and Technology* 26.11 (2015), p. 115202.

[100] X. Gao, L. Yang, Y. Wang, B. Zhang, X. Dan, J. Li, and S. Wu. "Spatial phase-shift dual-beam speckle interferometry". In: *Applied Optics* 57.3 (2018), pp. 414–419.

[101] W. Steinchen, L. Yang, and M. Schuth. "TV-shearography for measuring 3D-strains". In: *Strain* 32.2 (1996), pp. 49–58.

[102] H. Tada, P. C. Paris, and G. R. Irwin. "The stress analysis of cracks". In: *Handbook, Del Research Corporation* (1973).

[103] J. Dong, S. Wang, A. K. Yetisen, X. Dong, F. Pöller, N. Ong, M. Jakobi, Z. Liu, F. Salazar-Bloise, and A. W. Koch. "Shear-unlimited common-path speckle interferometer". In: *Optics Letters* 45.6 (2020), pp. 1305–1308.

[104] S. Wang, J. Dong, F. Pöller, X. Dong, M. Lu, L. M. Bilgeri, M. Jakobi, F. Salazar-Bloise, and A. W. Koch. "Dual-directional shearography based on a modified common-path configuration using spatial phase shift". In: *Applied Optics* 58.3 (2019), pp. 593–603.

[105] V. Arrizón and D. Sánchez-de La-Llave. "Common-path interferometry with one-dimensional periodic filters". In: *Optics Letters* 29.2 (2004), pp. 141–143.

[106] J. Glückstad and P. C. Mogensen. "Optimal phase contrast in common-path interferometry". In: *Applied Optics* 40.2 (2001), pp. 268–282.

[107] D. Francis, R. P. Tatam, and R. M. Groves. "Shearography technology and applications: a review". In: *Measurement Science and Technology* 21.10 (2010), p. 102001.

[108] J. R. Lee, D. J. Yoon, J. S. Kim, and A. Vautrin. "Investigation of shear distance in Michelson interferometer-based shearography for mechanical characterization". In: *Measurement Science and Technology* 19.11 (2008), p. 115303.

[109] J. Dong, A. K. Yetisen, X. Dong, F. Pöller, M. Jakobi, Z. Liu, F. Salazar-Bloise, and A. W. Koch. "Low-pass filtering compensation in common-path digital holographic microscopy". In: *Applied Physics Letters* 117.12 (2020), p. 121105.

[110] P. Marquet, B. Rappaz, P. J. Magistretti, E. Cuche, Y. Emery, T. Colomb, and C. Depeursinge. "Digital holographic microscopy: a noninvasive contrast imaging technique allowing quantitative visualization of living cells with subwavelength axial accuracy". In: *Optics Letters* 30.5 (2005), pp. 468–470.

[111] F. Merola, P. Memmolo, L. Miccio, R. Savoia, M. Mugnano, A. Fontana, G. D'ippolito, A. Sardo, A. Iolascon, A. Gambale, and P. Ferraro. "Tomographic flow cytometry by digital holography". In: *Light: Science & Applications* 6.4 (2017), e16241.

[112] R. Zhou, C. Edwards, A. Arbabi, G. Popescu, and L. L. Goddard. "Detecting 20 nm wide defects in large area nanopatterns using optical interferometric microscopy". In: *Nano Letters* 13.8 (2013), pp. 3716–3721.

[113] S. Khadir, P. Bon, D. Vignaud, E. Galopin, N. McEvoy, D. McCloskey, S. Monneret, and G. Baffou. "Optical imaging and characterization of graphene and other 2D materials using quantitative phase microscopy". In: *ACS Photonics* 4.12 (2017), pp. 3130–3139.

[114] S. Ebrahimi, M. Dashtdar, E. Sánchez-Ortiga, M. Martínez-Corral, and B. Javidi. "Stable and simple quantitative phase-contrast imaging by Fresnel biprism". In: *Applied Physics Letters* 112.11 (2018), p. 113701.

[115] S. Ebrahimi and M. Dashtdar. "Quantitative phase imaging based on Fresnel diffraction from a phase plate". In: *Applied Physics Letters* 115.20 (2019), p. 203702.

[116] S. H. S. Yaghoubi, S. Ebrahimi, M. Dashtdar, A. Doblas, and B. Javidi. "Common-path, single-shot phase-shifting digital holographic microscopy using a Ronchi ruling". In: *Applied Physics Letters* 114.18 (2019), p. 183701.

[117] P. Girshovitz and N. T. Shaked. "Doubling the field of view in off-axis low-coherence interferometric imaging". In: *Light: Science & Applications* 3.3 (2014), e151.

[118] H. Medecki, E. Tejnil, K. A. Goldberg, and J. Bokor. "Phase-shifting point diffraction interferometer". In: *Optics Letters* 21.19 (1996), pp. 1526–1528.

[119] H. Medecki. *Phase-shifting point diffraction interferometer*. US Patent 5,835,217. 1998.

[120] G. Popescu, T. Ikeda, R. R. Dasari, and M. S. Feld. "Diffraction phase microscopy for quantifying cell structure and dynamics". In: *Optics Letters* 31.6 (2006), pp. 775–777.

[121] P. Gao, B. Yao, J. Min, R. Guo, J. Zheng, T. Ye, I. Harder, V. Nercissian, and K. Mantel. "Parallel two-step phase-shifting point-diffraction interferometry for microscopy based on a pair of cube beamsplitters". In: *Optics Express* 19.3 (2011), pp. 1930–1935.

[122] N. T. Shaked. "Quantitative phase microscopy of biological samples using a portable interferometer". In: *Optics Letters* 37.11 (2012), pp. 2016–2018.

[123] P. Ferraro, S. De Nicola, A. Finizio, G. Coppola, S. Grilli, C. Magro, and G. Pierattini. "Compensation of the inherent wave front curvature in digital holographic coherent microscopy for quantitative phase-contrast imaging". In: *Applied Optics* 42.11 (2003), pp. 1938–1946.

[124] T. Nguyen, G. Nehmetallah, C. Raub, S. Mathews, and R. Aylo. "Accurate quantitative phase digital holographic microscopy with single-and multiple-wavelength telecentric and nontelecentric configurations". In: *Applied Optics* 55.21 (2016), pp. 5666–5683.

[125] T. Colomb, E. Cuche, F. Charrière, J. Kühn, N. Aspert, F. Montfort, P. Marquet, and C. Depeursinge. "Automatic procedure for aberration compensation in digital holographic microscopy and applications to specimen shape compensation". In: *Applied Optics* 45.5 (2006), pp. 851–863.

[126] L. Miccio, D. Alfieri, S. Grilli, P. Ferraro, A. Finizio, L. De Petrocellis, and S. D. Nicola. "Direct full compensation of the aberrations in quantitative phase microscopy of thin objects by a single digital hologram". In: *Applied Physics Letters* 90.4 (2007), p. 041104.

[127] W. Xiao, Q. Wang, F. Pan, R. Cao, X. Wu, and L. Sun. "Adaptive frequency filtering based on convolutional neural networks in off-axis digital holographic microscopy". In: *Biomedical Optics Express* 10.4 (2019), pp. 1613–1626.

[128] S. Liu, Q. Lian, Y. Qing, and Z. Xu. "Automatic phase aberration compensation for digital holographic microscopy based on phase variation minimization". In: *Optics Letters* 43.8 (2018), pp. 1870–1873.

[129] Z. Ren, J. Zhao, and E. Y. Lam. "Automatic compensation of phase aberrations in digital holographic microscopy based on sparse optimization". In: *APL Photonics* 4.11 (2019), p. 110808.

[130] C. Leiping, W. Xiao, L. Xiaoping, J. Liu, F. Pan, and P. Ferraro. "Automatic removal of phase aberration in holographic microscopy for drug sensitivity detection of ovarian cancer cells". In: *OSA Continuum* 3.7 (2020), pp. 1856–1868.

[131] G. Coppola, G. Di Caprio, M. Gioffré, R. Puglisi, D. Balduzzi, A. Galli, L. Miccio, M. Paturzo, S. Grilli, A. Finizio, and P. Ferraro. "Digital self-referencing quantitative phase microscopy by wavefront folding in holographic image reconstruction". In: *Optics Letters* 35.20 (2010), pp. 3390–3392.

[132] T. Colomb, J. Kühn, F. Charrière, C. Depeursinge, P. Marquet, and N. Aspert. "Total aberrations compensation in digital holographic microscopy with a reference conjugated hologram". In: *Optics Express* 14.10 (2006), pp. 4300–4306.

[133] C. J. Mann, L. Yu, C. M. Lo, and M. K. Kim. "High-resolution quantitative phase-contrast microscopy by digital holography". In: *Optics Express* 13.22 (2005), pp. 8693–8698.

[134] J. Dong, A. K. Yetisen, C. Zhao, X. Dong, F. Brändle, Q. Wang, M. Jakobi, D. Saur, and A. W. Koch. "Single-shot high-throughput phase imaging with multi-beam array interferometric microscopy". In: *ACS Photonics* 8.12 (2021), pp. 3536–3547.

[135] A. W. Lohmann, R. G. Dorsch, D. Mendlovic, Z. Zalevsky, and C. Ferreira. "Space–bandwidth product of optical signals and systems". In: *JOSA* 13.3 (1996), pp. 470–473.

[136] F. Ghaznavi, A. Evans, A. Madabhushi, and M. Feldman. "Digital imaging in pathology: whole-slide imaging and beyond". In: *Annual Review of Pathology: Mechanisms of Disease* 8 (2013), pp. 331–359.

[137] A. Greenbaum, Y. Zhang, A. Feizi, P. L. Chung, W. Luo, S. R. Kandukuri, and A. Ozcan. "Wide-field computational imaging of pathology slides using lens-free on-chip microscopy". In: *Applied Optics* 6.267 (2014), 267ra175.

[138] M. Mugnano, P. Memmolo, L. Miccio, F. Merola, V. Bianco, A. Bramanti, A. Gambale, R. Russo, I. Andolfo, and A. Iolascon. "Label-free optical marker for red-blood-cell phenotyping of inherited anemias". In: *Analytical Chemistry* 90.12 (2018), pp. 7495–7501.

[139] N. T. Shaked, L. L. Satterwhite, G. A. Truskey, A. P. Wax, and M. J. Telen. "Quantitative microscopy and nanoscopy of sickle red blood cells performed by wide field digital interferometry". In: *Journal of Biomedical Optics* 16.3 (2011), p. 030506.

[140] M. Ugele, M. Weniger, M. Leidenberger, Y. Huang, M. Bassler, O. Friedrich, B. Kappes, O. Hayden, and L. Richter. "Label-free, high-throughput detection of P. falciparuminfection in sphered erythrocytes with digital holographic microscopy". In: *Lab on a Chip* 18.12 (2018), pp. 1704–1712.

[141] T. Blasi, H. Hennig, H. D. Summers, F. J. Theis, J. Cerveira, J. O. Patterson, D. Davies, A. Filby, A. E. Carpenter, and P. Rees. "Label-free cell cycle analysis for high-throughput imaging flow cytometry". In: *Nature Communications* 7.1 (2016), pp. 1–9.

[142] K. Goda, A. Ayazi, D. R. Gossett, J. Sadasivam, C. K. Lonappan, E. Sollier, A. M. Fard, S. C. Hur, J. Adam, C. Murray, et al. "High-throughput single-microparticle imaging flow analyzer". In: *PNAS* 109.29 (2012), pp. 11630–11635.

[143] F. Le Clerc, M. Gross, and L. Collot. "Synthetic-aperture experiment in the visible with on-axis digital heterodyne holography". In: *Optics Letters* 26.20 (2001), pp. 1550–1552.

[144] S. A. Alexandrov, T. R. Hillman, T. Gutzler, and D. D. Sampson. "Synthetic aperture Fourier holographic optical microscopy". In: *Physical Review Letters* 97.16 (2006), p. 168102.

[145] W. Luo, A. Greenbaum, Y. Zhang, and A. Ozcan. "Synthetic aperture-based on-chip microscopy". In: *Light: Science & Applications* 4.3 (2015), e261–e261.

[146] L. Tian, Z. Liu, L. Yeh, M. Chen, J. Zhong, and L. Waller. "Computational illumination for high-speed in vitro Fourier ptychographic microscopy". In: *Optica* 2.10 (2015), pp. 904–911.

[147] H. Wang, Z. Göröcs, W. Luo, Y. Zhang, Y. Rivenson, L. A. Bentolila, and A. Ozcan. "Computational out-of-focus imaging increases the space–bandwidth product in lens-based coherent microscopy". In: *Optica* 3.12 (2016), pp. 1422–1429.

[148] V. Micó, J. Zheng, J. Garcia, Z. Zalevsky, and P. Gao. "Resolution enhancement in quantitative phase microscopy". In: *Advances in Optics and Photonics* 11.1 (2019), pp. 135–214.

[149] Y. Xue, S. Cheng, Y. Li, and L. Tian. "Reliable deep-learning-based phase imaging with uncertainty quantification". In: *Optica* 6.5 (2019), pp. 618–629.

[150] M. Kellman, E. Bostan, M. Chen, and L. Waller. "Data-driven design for fourier ptychographic microscopy". In: *2019 IEEE International Conference on Computational Photography (ICCP)*. IEEE. 2019, pp. 1–8.

[151] O. Matoba and B. Javidi. "Encrypted optical storage with angular multiplexing". In: *Applied Optics* 38.35 (1999), pp. 7288–7293.

[152] N. T. Shaked, V. Micó, M. Trusiak, A. Kuś, and S. K. Mirsky. "Off-axis digital holographic multiplexing for rapid wavefront acquisition and processing". In: *Advances in Optics and Photonics* 12.3 (2020), pp. 556–611.

[153] W. Zhang, L. Cao, G. Jin, and D. Brady. "Full field-of-view digital lens-free holography for weak-scattering objects based on grating modulation". In: *Applied Optics* 57.1 (2018), A164–A171.

[154] Z. Liu, M. Centurion, G. Panotopoulos, J. Hong, and D. Psaltis. "Holographic recording of fast events on a CCD camera". In: *Optics Letters* 27.1 (2002), pp. 22–24.

[155] X. Wang, H. Zhai, and G. Mu. "Pulsed digital holography system recording ultrafast process of the femtosecond order". In: *Optics Letters* 31.11 (2006), pp. 1636–1638.

[156] V. Mico, Z. Zalevsky, P. Garcia-Martinez, and J. Garcia. "Single-step superresolution by interferometric imaging". In: *Optics Express* 12.12 (2004), pp. 2589–2596.

[157] A. Calabuig, V. Micó, J. Garcia, Z. Zalevsky, and C. Ferreira. "Single-exposure super-resolved interferometric microscopy by red-green-blue multiplexing". In: *Optics Letters* 36.6 (2011), pp. 885–887.

[158] C. Yuan, H. Zhai, and H. Liu. "Angular multiplexing in pulsed digital holography for aperture synthesis". In: *Optics Letters* 33.20 (2008), pp. 2356–2358.

[159] P. Hosseini, Y. Sung, Y. Choi, N. Lue, Z. Yaqoob, and P. So. "Scanning color optical tomography (SCOT)". In: *Optics Express* 23.15 (2015), pp. 19752–19762.

[160] K. Dorozynska and E. Kristensson. "Implementation of a multiplexed structured illumination method to achieve snapshot multispectral imaging". In: *Optics Express* 25.15 (2017), pp. 17211–17226.

[161] I. Frenklach, P. Girshovitz, and N. T. Shaked. "Off-axis interferometric phase microscopy with tripled imaging area". In: *Optics Letters* 39.6 (2014), pp. 1525–1528.

[162] B. Tayebi, F. Sharif, M. R. Jafarfard, and D. Y. Kim. "Double-field-of-view, quasi-common-path interferometer using Fourier domain multiplexing". In: *Optics Express* 23.20 (2015), pp. 26825–26833.

[163] B. Lee, C. Jang, D. Kim, and B. Lee. "Single grating reflective digital holography with double field of view". In: *IEEE Transactions on Industrial Informatics* 15.11 (2019), pp. 6155–6161.

[164] P. Gao, I. Harder, V. Nercissian, K. Mantel, and B. Yao. "Phase-shifting point-diffraction interferometry with common-path and in-line configuration for microscopy". In: *Optics Letters* 35.5 (2010), pp. 712–714.

[165] J. Burch, A. Ennos, and R. Wilton. "Dual-and multiple-beam interferometry by wavefront reconstruction". In: *Nature* 209.5027 (1966), pp. 1015–1016.

[166] T. Kondo, S. Matsuo, S. Juodkazis, and H. Misawa. "Femtosecond laser interference technique with diffractive beam splitter for fabrication of three-dimensional photonic crystals". In: *Applied Physics Letters* 79.6 (2001), pp. 725–727.

[167] C. Lu and R. H. Lipson. "Interference lithography: a powerful tool for fabricating periodic structures". In: *Laser & Photonics Reviews* 4.4 (2010), pp. 568–580.

[168] G. M. Burrow and T. K. Gaylord. "Multi-beam interference advances and applications: nano-electronics, photonic crystals, metamaterials, subwavelength structures, optical trapping, and biomedical structures". In: *Micromachines* 2.2 (2011), pp. 221–257.

[169] V. Bianco, M. Paturzo, V. Marchesano, I. Gallotta, E. Di Schiavi, and P. Ferraro. "Optofluidic holographic microscopy with custom field of view (FoV) using a linear array detector". In: *Lab on a Chip* 15.9 (2015), pp. 2117–2124.

[170] M. K. Kim. "Wide area quantitative phase microscopy by spatial phase scanning digital holography". In: *Optics Letters* 45.3 (2020), pp. 784–786.

[171] D. Psaltis, S. R. Quake, and C. Yang. "Developing optofluidic technology through the fusion of microfluidics and optics". In: *Nature* 442.7101 (2006), pp. 381–386.

[172] M. M. Wintrobe. "Clinical hematology". In: *Academic Medicine* 37.1 (1962), p. 78.

[173] G. Popescu, T. Ikeda, K. Goda, C. A. Best-Popescu, M. Laposata, S. Manley, R. R. Dasari, K. Badizadegan, and M. S. Feld. "Optical measurement of cell membrane tension". In: *Physical Review Letters* 97.21 (2006), p. 218101.

[174] H. S. Park, W. J. Eldridge, W. Yang, M. Crose, S. Ceballos, J. D. Roback, J. A. Chi, and A. Wax. "Quantitative phase imaging of erythrocytes under microfluidic constriction in a high refractive index medium reveals water content changes". In: *Microsystems & Nanoengineering* 5.1 (2019), pp. 1–9.

[175] M. E. Kandel, Y. R. He, Y. J. Lee, T. H. Chen, K. M. Sullivan, O. Aydin, M. T. A. Saif, H. Kong, N. Sobh, and G. Popescu. "Phase Imaging with Computational Specificity (PICS) for measuring dry mass changes in sub-cellular compartments". In: *Nature Communications* 11.1 (2020), pp. 1–10.

[176] Y. Park, C. A. Best, T. Auth, N. S. Gov, S. A. Safran, G. Popescu, S. Suresh, and M. S. Feld. "Metabolic remodeling of the human red blood cell membrane". In: *PNAS* 107.4 (2010), pp. 1289–1294.

[177] G. Popescu. *Quantitative phase imaging of cells and tissues*. McGraw-Hill Education, 2011.

[178] Y. Rivenson, T. Liu, Z. Wei, Y. Zhang, K. de Haan, and A. Ozcan. "PhaseStain: the digital staining of label-free quantitative phase microscopy images using deep learning". In: *Light: Science & Applications* 8.1 (2019), pp. 1–11.

[179] G. Dardikman and N. T. Shaked. "Is multiplexed off-axis holography for quantitative phase imaging more spatial bandwidth-efficient than on-axis holography?" In: *JOSA* 36.2 (2019), A1–A11.

[180] Y. Baek, K. Lee, S. Shin, and Y. Park. "Kramers-Kronig holographic imaging for high-space-bandwidth product". In: *Optica* 6.1 (2019), pp. 45–51.

[181] H. Kwon, E. Arbabi, S. M. Kamali, M. Faraji-Dana, and A. Faraon. "Single-shot quantitative phase gradient microscopy using a system of multifunctional metasurfaces". In: *Nature Photonics* 14.2 (2019), pp. 109–114.

[182] M. E. Kandel, C. Hu, G. N. Kouzehgarani, E. Min, K. M. Sullivan, H. Kong, J. M. Li, D. N. Robson, M. U. Gillette, C. Best-Popescu, et al. "Epi-illumination gradient light interference microscopy for imaging opaque structures". In: *Nature Communications* 10.1 (2019), pp. 1–9.

[183] C. Edwards, A. Arbabi, G. Popescu, and L. L. Goddard. "Optically monitoring and controlling nanoscale topography during semiconductor etching". In: *Light: Science & Applications* 1.9 (2012), e30–e30.

[184] D. Fu, W. Choi, Y. Sung, Z. Yaqoob, R. R. Dasari, and M. Feld. "Quantitative dispersion microscopy". In: *Biomedical Optics Express* 1.2 (2010), pp. 347–353.

[185] N. Lue, J. W. Kang, T. R. Hillman, R. R. Dasari, and Z. Yaqoob. "Single-shot quantitative dispersion phase microscopy". In: *Applied Physics Letters* 101.8 (2012), p. 084101.

[186] S. Chowdhury, W. J. Eldridge, A. Wax, and J. A. Izatt. "Spatial frequency-domain multiplexed microscopy for simultaneous, single-camera, one-shot, fluorescent, and quantitative-phase imaging". In: *Optics Letters* 40.21 (2015), pp. 4839–4842.

[187] M. A. Herráez, D. R. Burton, M. J. Lalor, and M. A. Gdeisat. "Fast two-dimensional phase-unwrapping algorithm based on sorting by reliability following a noncontinuous path". In: *Applied Optics* 41.35 (2002), pp. 7437–7444.

Publication List

Articles

[1] J. Dong, A. K. Yetisen, C. Zhao, X. Dong, F. Brändle, Q. Wang, M. Jakobi, D. Saur, and A. W. Koch. "Single-shot high-throughput phase imaging with multi-beam array interferometric microscopy". In: *ACS Photonics* 8.12 (2021), pp. 3536–3547. DOI: 10.1021/acsphotonics.1c01124.

[2] J. Dong, A. K. Yetisen, X. Dong, F. Pöller, M. Jakobi, Z. Liu, F. Salazar-Bloise, and A. W. Koch. "Low-pass filtering compensation in common-path digital holographic microscopy". In: *Applied Physics Letters* 117.12 (2020), p. 121105. DOI: 10.1063/5.0019209.

[3] J. Dong, S. Wang, A. K. Yetisen, X. Dong, F. Pöller, N. Ong, M. Jakobi, Z. Liu, F. Salazar-Bloise, and A. W. Koch. "Shear-unlimited common-path speckle interferometer". In: *Optics Letters* 45.6 (2020), pp. 1305–1308. DOI: 10.1364/OL.382893.

[4] J. Dong, S. Wang, M. Lu, M. Jakobi, Z. Liu, X. Dong, F. Pöller, L. M. Bilgeri, F. Salazar-Bloise, A. K. Yetisen, and A. W. Koch. "Real-time dual-sensitive shearography for simultaneous in-plane and out-of-plane strain measurements". In: *Optics Express* 27.3 (2019), pp. 3276–3283. DOI: 10.1364/OE.27.003276.

[5] J. Rao, J. Dong, J. Wang, and E. Rank. "Application of common-path speckle interferometer with unlimited minimal shearing amount to characterization of irregularly shaped notch". In: *NDT & E International* 116 (2020), p. 102326. DOI: 10.1016/j.ndteint.2020.102326.

[6] X. Dong, J. Dong, A. K. Yetisen, M. H. Koehler, S. Wang, M. Jakobi, and A. W. Koch. "Characterization and layer thickness mapping of two-dimensional MoS2 flakes via hyperspectral line-scanning microscopy". In: *Applied Physics Express* 12.10 (2019), p. 102004. DOI: 10.7567/1882-0786/ab3e51.

[7] J. Zhao, J. Dong, Z. Liu, and H. Xie. "Characterization method of mechanical properties of rubber materials based on in-situ stereo finite-element-model updating". In: *Polymer Testing* 79 (2019), p. 106015. DOI: 10.1016/j.polymertesting.2019.106015.

[8] S. Wang, J. Dong, F. Pöller, X. Dong, M. Lu, L. M. Bilgeri, M. Jakobi, F. Salazar-Bloise, and A. W. Koch. "Dual-directional shearography based on a modified common-path configuration using spatial phase shift". In: *Applied Optics* 58.3 (2019), pp. 593–603. DOI: 10.1364/AO.58.000593.

[9] S. Balbach, N. Jiang, R. Moreddu, X. Dong, W. Kurz, C. Wang, J. Dong, Y. Yin, H. Butt, M. Brischwein, O. Hayden, M. Jakobi, S. Tasoglu, A. W. Koch, and A. K. Yetisen. "Smartphone-based colorimetric detection system for portable health tracking". In: *Analytical Methods* 13.38 (2021), pp. 4361–4369. DOI: 10.1039/d1ay01209f.

[10] X. Dong, A. K. Yetisen, J. Dong, K. Wang, P. Kienle, M. Jakobi, and A. W. Koch. "Hyperspectral fingerprints for atomic layer mapping of two-dimensional materials with single-layer accuracy". In: *The Journal of Physical Chemistry C* 125.30 (2021), pp. 16583–16590. DOI: 10.1039/D1AY01209F.

[11] X. Dong, H. Li, Z. Jiang, T. Grunleitner, I. Guler, J. Dong, K. Wang, M. H. Kohler, M. Jakobi, B. H. Menze, A. K. Yetisen, I. D. Sharp, A. V. Stier, J. J. Finley, and A. W. Koch. "3D deep learning enables accurate layer mapping of 2D materials". In: *ACS Nano* 15.2 (2021), pp. 3139–3151. DOI: 10.1021/acsnano.0c09685.

[12] N. Jiang, A. K. Yetisen, N. Linhart, K. Flisikowski, J. Dong, X. Dong, H. Butt, M. Jakobi, A. Schnieke, and A. W. Koch. "Fluorescent dermal tattoo biosensors for electrolyte analysis". In: *Sensors and Actuators B: Chemical* 320 (2020), p. 128378. DOI: 10.1016/j.snb.2020.128378.

[13] X. Dong, A. K. Yetisen, H. Tian, J. Dong, M. H. Köhler, M. Jakobi, and A. W. Koch. "Analyses of hyperspectral imaging microscopy data sets of semiconducting 2D materials". In: *Applied Physics Express* 13.5 (2020), p. 052008. DOI: 10.35848/1882-0786/ab88c7.

[14] X. Dong, A. K. Yetisen, H. Tian, I. Guler, A. V. Stier, Z. Li, M. H. Kohler, J. Dong, M. Jakobi, J. J. Finley, and A. W. Koch. "Line-scan hyperspectral imaging microscopy with linear unmixing for automated two-dimensional crystals identification". In: *ACS Photonics* 7.5 (2020), pp. 1216–1225. DOI: 10.1021/acsphotonics.0c00050.

[15] A. K. Yetisen, N. Jiang, C. M. Castaneda Gonzalez, Z. I. Erenoglu, J. Dong, X. Dong, S. Stößer, M. Brischwein, H. Butt, M. F. Cordeiro, M. Jakobi, O. Hayden, and A. W. Koch. "Scleral lens sensor for ocular electrolyte analysis". In: *Advanced Materials* 32.6 (2020), p. 1906762. DOI: 10.1002/adma.201906762.

[16] X. Dong, A. K. Yetisen, M. H. Köhler, J. Dong, S. Wang, M. Jakobi, X. Zhang, and A. W. Koch. "Microscale spectroscopic mapping of 2D optical materials". In: *Advanced Optical Materials* 7.18 (2019), p. 1900324. DOI: 10.1002/adom.201900324.

[17] A. K. Yetisen, R. Moreddu, S. Seifi, N. Jiang, K. Vega, X. Dong, J. Dong, H. Butt, M. Jakobi, M. Elsner, and A. W. Koch. "Dermal tattoo biosensors for colorimetric metabolite detection". In: *Angewandte Chemie* 131.31 (2019), pp. 10616–10623. DOI: 10.1002/ange.201904416.

[18] A. K. Yetisen, B. Soylemezoglu, J. Dong, Y. Montelongo, H. Butt, M. Jakobi, and A. W. Koch. "Capillary flow in microchannel circuitry of scleral lenses". In: *RSC Advances* 9.20 (2019), pp. 11186–11193. DOI: 10.1039/C9RA01094G.

[19] F. Pöller, F. Salazar-Bloise, M. Jakobi, S. Wang, J. Dong, and A. W. Koch. "Non-contact roughness measurement in sub-micron range by considering depolarization effects". In: *Sensors* 19.10 (2019), p. 2215. DOI: 10.3390/s19102215.

Patents Filed

[1] J. Dong. *Vorrichtung zur interferometrischen Mehrstrahl-Array-Mikroskopie*. German patent, DE 10 2021 004 043 A1. 2021.

[2] J. Dong, S. Wang, and M. Jakobi. *Vorrichtung und Verfahren für ein gleichzeitig in-plane- und out-of-plane-sensitives Shearographiesystem*. German patent, DE 10 2019 000 564 A1. 2019.

Supervised Theses

[1] *Multibeam array interferometric microscopy for high-throughput phase imaging.* Master thesis, Technical University of Munich. 2021.

[2] *Sampling phase reconstruction in off-axis digital holographic microscopy.* Bachelor thesis, Technical University of Munich. 2020.

[3] *Shearing-adjustable common-path shearography.* Bachelor thesis, Technical University of Munich. 2019.

[4] *Test Equipment Measurement with iPMA.* Engineering Practice, Technical University of Munich. 2020.